Actuation of Shape Memory Polymer using Magnetic Fields for Applications in Medical Devices

By

Patrick Regan Buckley

B.S. Mechanical Engineering
Massachusetts Institute of Technology, 2003

SUBMITTED TO THE DEPARTMENT OF MECHANICAL ENGINEERING IN PARTIAL FULFILLMENT OF THE REQUIRMENTS FOR THE DEGREE OF

MASTER OF SCIENCE IN MECHANICAL ENGINEERING
AT THE
MASSACHUSETTS INSTITUTE OF TECHNOLOGY

JUNE 2004

Signature of Author:_____

Patrick Regan Buckley
Department of Mechanical Engineering
2004

Certified by:_____

Gareth Mckinley
Professor of Mechanical Engineering
Thesis Supervisor

Accepted by:_____

Ain Sonin
Professor of Mechanical Engineering
Graduate Officer

Actuation of Shape Memory Polymer using Magnetic Fields for Applications in Medical Devices

By

Patrick Regan Buckley

Submitted to the Department of Mechanical Engineering
on 21 May, 2004, in Partial Fulfillment of the
Requirements for the Degree of Masters of Science in
Mechanical Engineering

ABSTRACT

A novel approach to the heating and actuation of shape memory polymer using dispersed Curie temperature thermo-regulated particles is proposed. Such a material has potential applications in medical devices which are delivered via catheters. A variety of tests were performed to determine the feasibility of this new approach to shape memory polymer actuation. Calorimetry tests were performed to quantify heat generation of various Nickel Zinc Ferrite particles. Dynamic Mechanical Thermal Analysis (DMTA), tensile strain recovery tests, and Differential Scanning Calorimetry (DSC) were used to measure the mechanical effects of various particle volume contents and sizes on shape memory polymer. These tests suggest that the proposed method of actuation is very feasible, rapid heating can be achieved and the addition of particles up to 10% volume content has a minimal effect on the mechanical properties of the shape memory polymer.

Thesis Supervisor: Gareth Mckinley
Title: Professor of Mechanical Engineering

Acknowledgments

This thesis was made possible by the help of a great number of people. I am grateful for all the help and encouragement I received from the team of researchers at the Lawrence Livermore National Laboratory, this includes but is not limited to Duncan Maitland, Tom Wilson, Melodie Metzger, Jane Bearinger, Brian Kelly and Ward Small. Other people who contributed to the successful completion of this thesis in a less direct but just as important manner, by providing moral support and or shelter during my time in the "van down by the river" are Darcy Kelly, Shawn Graham, Kurt Herzog, and Patrick Riley. Mr. Riley was especially inspiring to me and I am lucky to have him as a friend.

My thesis advisor Prof. Gareth Mckinley deserves a huge thanks, he is one of the most excellent teachers I have had and I was always amazed by his wisdom and cheered by his humor.

My family and friends, especially my mother, Judith Regan, and the very special Alexis Dieter deserve a thank you. They are two of the best woman I know. Tom Truelove thanks for correcting my atrocious grammer, and always being ready to go to Anna's. Henry Gabathuler thanks for your legal advice, you are going to make a great patent lawyer. I know I am missing people in this acknowledgment so I will end by just thanking everyone I know, that should cover it. That's it, I am done!

Table of Contents

Table of Figures

List of Tables

1 INTRODUCTION

1.1 Purpose

Shape memory polymers (SMP) are a class of polymeric materials that can be formed into a specific primary shape, reformed into a secondary stable shape, and then controllably actuated by heating to recover its primary shape. This useful "shape memory" property makes SMP an attractive material for certain medical applications, ranging from stents to devices and tools which need to be delivered via catheter. Presently, minimally invasive catheter surgical techniques are limited by the functionality of the tools and devices which can be delivered inside the catheter. Devices must be small and or collapsible to fit inside the catheter, yet be useful once delivered to the site of interest. Utilizing SMP for medical devices such as stents or neurovascular surgical tools has great potential for creating new breakthrough treatment options that are presently not available.

While other classes of thermally activated shape memory materials have been developed, shape memory alloys (SMA) (Schetky 1979) and shape memory ceramics (Swain 1986) being the two other major classes, SMP has a number of properties that make it better suited for certain medical applications. Firstly, shape memory ceramics have quite small recoverable strain and for this reason have not been used in any medical applications known to the author. SMA have been adopted in a number of medical devices and would be the material SMP would be competing with when the use of a shape memory material was necessary or seen as beneficial for a medical device, and for this reason these two materials will be compared.

The shape memory characteristics of SMA and SMP are vastly different, affecting the potential applications the materials are used in. Some of these key differences are illustrated in Table 1 (Otsuka and Wayman 1998).

Physical Properties	Shape Memory Polymer	Shape Memory Alloy
Density (g/cm^3)	0.9-1.1	6-8
Deformation (%)	250-800	6-7
Recovery temperature (C)	25-90	-10-100
Force required for deformation (kgf/ cm^2)	10-30	500-2000
Recovery stress (kgf/ cm^3)	10-30	500-2000

Table 1: Comparison of SMP and SMA properties (Otsuka and Wayman 1998)

As can be seen above, SMP is able to undergo deformations two orders of magnitude greater then SMA. SMA has the advantage of being able to generate a much larger force then SMP while actuating, demonstrated in the greater recovery stress. This indicates that SMA is a good material to use in applications where large forces are needed but small changes of shape are acceptable. SMP is better for applications where large changes in shape are desired but force generation is not as important. SMP also has some other advantages, such as it is cheaper and easier to program the primary and secondary shapes of SMP compared to SMA. SMP shapes can be programmed at temperatures ~100°C, while for SMA shapes must be programmed at higher temperatures, ~400°C. SMP can also be made in a biodegradable form (Lendlein and Langer) so that temporarily implanted devices can be degraded and absorbed by the body, eliminating the need for surgical retrieval. SMA does not give this option.

Currently there is much research into developing devices which take advantage of the unique properties of SMP. Some of the devices and research already done in this field includes vascular graft materials (Szycher, 1998), implant devices (Kusy and Whitley, 1994), catheters (LaFontaine, 1996), and microactuators (Benett et al., 1998).

The actuation temperature of SMP is determined by the soft phase material glass transition temperature of the material. This glass transition temperature (T_g) can be adjusted by changing the chemistry of the material which in turn affects the cross linking of the polymer chains. At the present time the major focus is on using SMP with a T_g of 55°C. This material has desirable stiffness at body temperatures and a T_g that is believed to be attainable without causing damage to the patient.

One of the major engineering challenges that stands in the way of using SMP in medical devices is the difficulty of heating devices to T_g inside the body. Presently SMP devices are heated using lasers or resistive heating elements(Maitland et al. 2002). These methods have the following disadvantages and limitations.

1. They require a power transmission line, be it a fiber optic or electrical wire. These power transmission lines lose energy over their length, impede the flexibility of a catheter, require larger catheters to house them, and must be jointed to a device. It has been the author's experience that a devices joint can be the most complicated and failure prone part of a device.
2. The device geometry is limited by the heating mechanism. For example, if a laser is used, the ability of light to travel through the geometry of the device and be absorbed by the SMP severely limits the shape of a device.
3. Laser and resistive heating elements require feed back systems to ensure that devices do not over heat.

An alternative to using lasers or resistive heating elements is the use of inductive heating. This thesis proposes a novel method of SMP actuation which uses ferromagnetic particles dispersed in an SMP matrix as a means of induction heating. These dispersed

particles can be heated using alternating magnetic fields to cause heating and actuation of SMP. To the knowledge of the author this is the first proposed mechanism that will allow the use of inductive heating to cause SMP actuation. The method is illustrated in a general manner in the figure below. This figure is not to scale and it only serves to illustrate the principle of the idea.

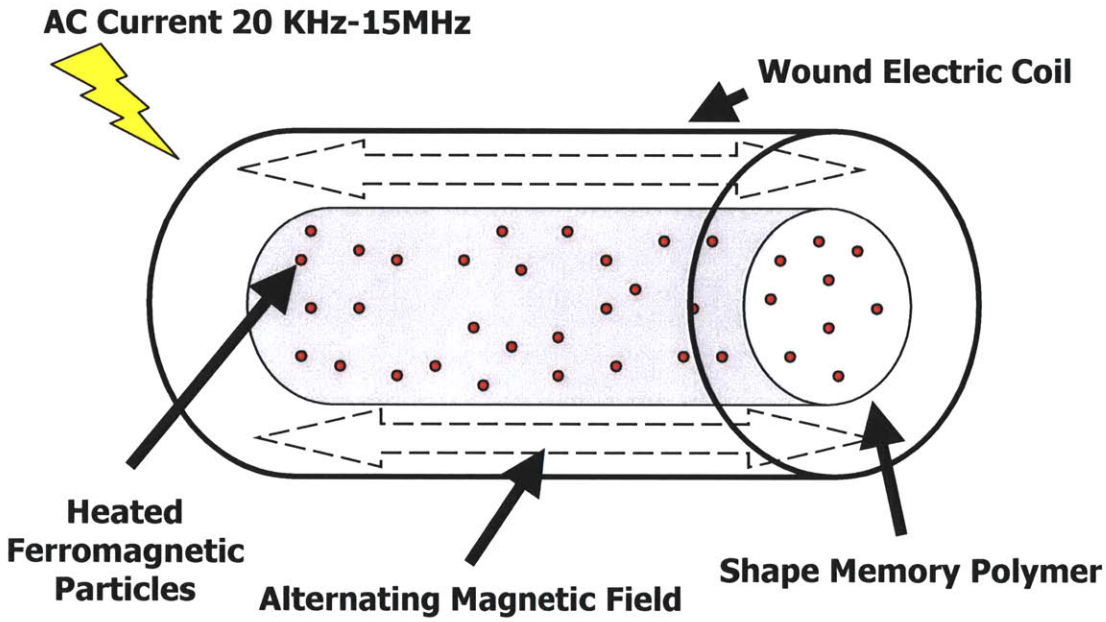

Figure 1: Proposed method of inductive heating of shape memory polymer using dispersed ferromagnetic particles.

Further advantages of this approach are realized when the useful property of a ferromagnetic material's Curie temperature (T_c) is understood and properly selected. T_c is the temperature at which a ferromagnetic material becomes paramagnetic, losing its ability to generate heat via a hysteresis loss mechanism (Goldman 1990). By selecting a ferromagnetic particle material with a T_c near the T_g of SMP, and by using particle sizes and materials which will heat mainly via a magnetic hysteresis loss mechanism instead of eddy current mechanism, it becomes possible to have a thermoregulation mechanism

which is an innate property of the material. The advantages of the inductive heating approach over the laser or resistive heating approaches are listed below.

1. There are no power transmission lines, heating and actuation is remote. This allows smaller catheters to be used, increasing the access of a device to narrower vessels.
2. More complex device geometries are possible since even and consistent heating is provided throughout the SMP, and conduction lengths are very short due to the evenly dispersed particles.
3. The joint between the device and the power transmission line is eliminated, simplifying and making a device more robust.
4. Thermoregulation can be provided by selecting the Curie temperature of the ferromagnetic particles, eliminating the need for thermoregulatory feedback systems.

1.2 Specific Medical Application: Strokes

The area of neurovascular surgery has a great need for devices that can function in the narrow and delicate vessels of the brain. In particular, there is a desperate need for a device to treat acute ischemic stroke, which is a stroke caused by a blockage of blood flow to the brain due to a lodged blood clot. 88% of all strokes in the US are of the ischemic variety (Maitland et al. 2002; A.H.A. 2003) and stroke is the third leading cause of death, with 163,538 deaths in 2001, and the leading cause of disability in the United States(A.H.A. 2003). Conservative estimates indicate that some 700,000 strokes occur annually and are expected to have an associated direct and indirect cost of 53.6 billion dollars in the year 2004 (A.H.A. 2003). Presently the only FDA approved treatment for

acute ischemic stroke is a blood thinning medication, tissue plasminogen activator (tPA). This drug is minimally affective, must be administered within 3 hours of the onset of stroke, is associated with increased risk of intracranial hemorrhaging, and, as a result, is administered in only 2-3% of acute stroke cases (Jonathan Hartmann 2003).

There can, however, be a window of 24 hours in which to restore blood flow before permanent brain damage is sustained (Maitland et al. 2002). This lengthy window allows time for surgical procedures and makes mechanical intervention to remove a clot an attractive option. At present there are few effective devices that exist to extract these clots. The tools and devices which do exist to perform clot extraction are relatively invasive and are limited to larger vessels such as the carotid arteries (4-5mm diameter). However, most blockages occur in the narrower (<3 mm diameter), and more deeply-seated vessels, such as the middle cerebral artery (Maitland et al. 2002).

It is the author's belief that the above mentioned advantages of an inductively heated shape memory polymer, mainly the possibility of the remote actuation of a complex shaped device, and the possibility of using smaller catheters for device delivery, may offer the breakthrough that enables the design of a device which is small enough and savvy enough to perform clot extraction in the narrow and winding neurovasculature. If such a device is realized, it will provide a much more effective treatment option for people suffering an acute ischemic stroke than what is currently available. There is presently a group of researchers led by Duncan Maitland at the Lawrence Livermore National Laboratory who are working on the development of a clot extraction device made from SMP. One of the device embodiments is illustrated in the figure below.

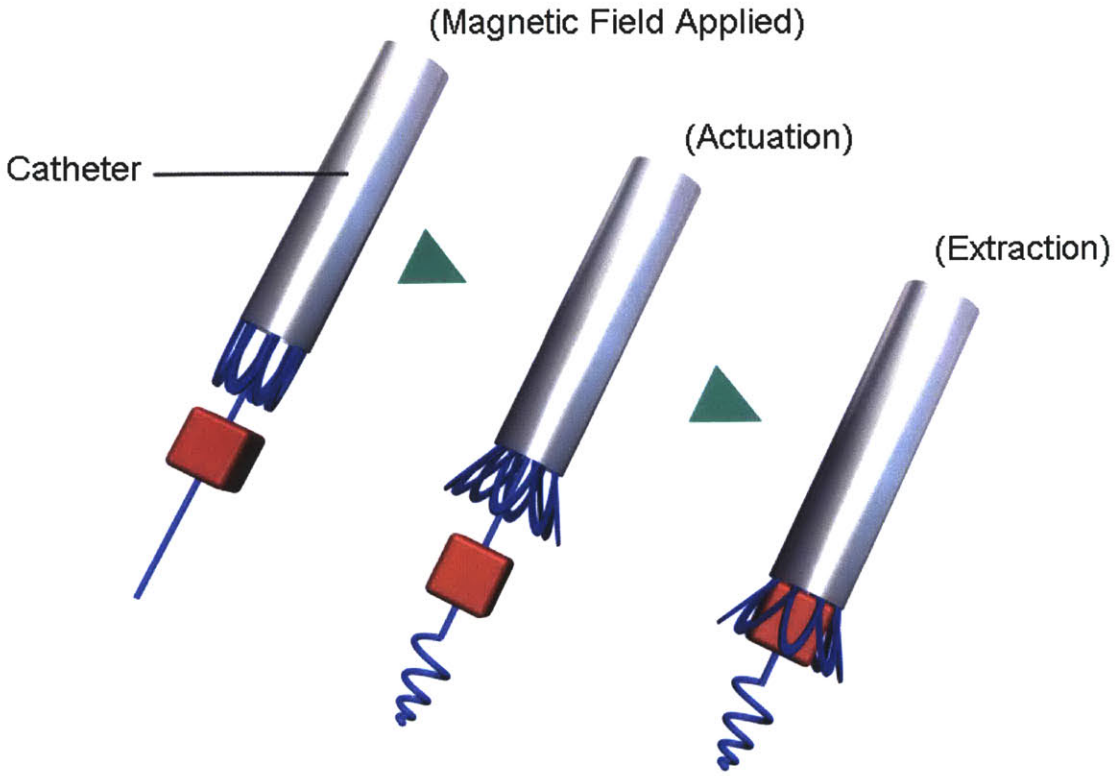

Figure 2: The embodiment of a clot extracting device which employs inductively heated shape memory polymer as a device material, red block represents a blood clot.

If the implementation of inductively heated SMP proves to be successful in a clot extraction device, there are a host of other potential devices that may benefit from the material.

1.3 Scope of Thesis

1.3.1 Review of Induction Heating in Previous Medical Applications

A large body of research exists on the use of induction heating for hyperthermia treatment. This is a treatment that attempts to heat cancerous tissue to above 42°C in an attempt to kill or weaken the diseased area. A review of the literature provides safety limits for magnetic field strengths and frequencies as well as providing some recommendations for Curie temperature thermo-regulated materials and possible designs for induction coils and field generating machines.

1.3.2 Magnetic Material Characterization and Review

The different mechanisms of induction heating, hysteresis loss, and eddy current loss will be reviewed. This will aid in the future selection of a material that has a Curie temperature thermoregulation as described above. A number of possible materials will be suggested and three commercially available Nickel Zinc Ferrites will be experimented with. These three materials will be dispersed into SMP with varying particle sizes, ranging from 6.71-43.6 microns, and varying volume contents, ranging from 1-20% by volume magnetic material. The figure below shows an example of a particle loaded SMP matrix.

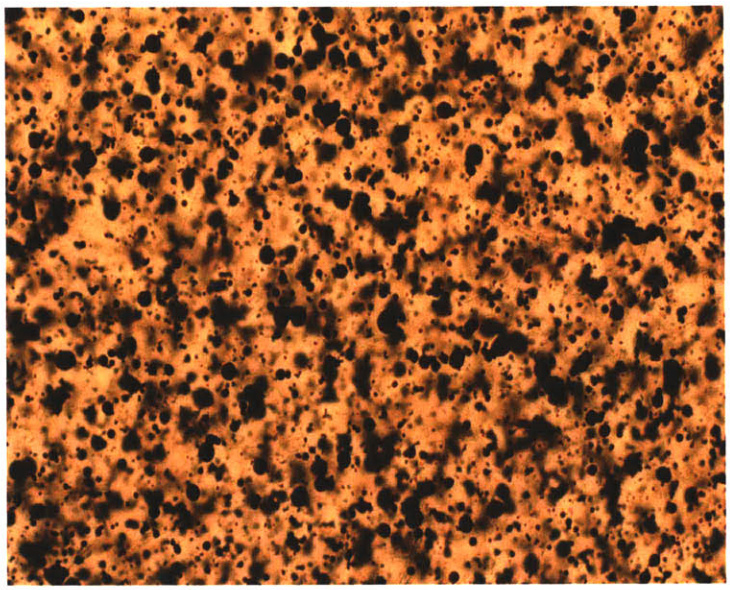

Figure 3: A 5x magnification of 1% by volume Nickel Zinc Ferrite particle loaded SMP matrix

1.3.3 Demonstration of Inductive Heating

Inductive heating of the SMP will be demonstrated and the affect of particle size and volume content on heating rates will be explored. The actuation of complex shaped devices using the inductive heating approach will also be shown.

1.3.4 Mechanical Properties of Particle loaded SMP

The effect of dispersed particles on the mechanical properties of SMP will be explored. The thermo-mechanical effects on the material will be determined by Dynamic Mechanical Thermal Analysis (DMTA) and Differential Scanning Calorimetry (DSC). Large strain recovery will be tested with a tensile testing machine.

2 Literature Review and Background

2.1 Hyperthermia

A great deal of research has gone into the development of inductive heating for applications in the field of Hyperthermia. Hyperthermia is a form of treatment that attempts to kill or weaken cancerous tissue by heating. A number of researchers have demonstrated the functionality of "thermal seeds", magnetic material in the form of cylindrical rods or particles which are implanted in the cancerous area and are then heated using an alternating magnetic field. While this application of inductive heating is very different than that proposed in this thesis, the research in this field has demonstrated materials, field strengths, frequencies, and achievable heating rates using inductive heating in the body. Because the temperature range desired for hyperthermia treatment and SMP actuation overlap, hyperthermia attempts to generate temperatures $\geq 42°C$ (Stauffer et al. 1984) and most SMP devices can be actuated in the temperature range of $35°C \leq T \leq 80°C$, the research done in this field can be directly applied to inductively actuated SMP.

2.1.1 Thermoregulation and Curie Temperature

A key aspect of both hyperthermia and inductively actuated SMP is thermoregulation. It is important to be able to set the maximum temperature of a heating device placed inside the body. This is important because excessive heating can damage body tissue and if it occurs in an SMP device it could cause melting of the plastic, an event that would most likely have adverse effects on health. Limiting the maximum temperature can be achieved with complicated and invasive feed back circuits but the simplest and most effective way of setting a maximum temperature with inductive

heating is by controlling the heating material's Curie temperature (T_c) and ensuring that the material heats mainly via a hysteresis loss mechanism. T_c is the temperature at which a ferromagnetic material transitions to a paramagnetic material (McCurrie 1994). At T_c the materials magnetic permeability drops to that of free space and the material no longer experiences hysteresis losses. This transition is an automatic temperature control built into the material. Field frequencies and strengths will not influence the Curie temperature. The key to the success of inductively heated SMP is to find the optimum material for the heating particles. A number of materials with low Curie temperatures (40-100 degrees Celsius) are reviewed and proposed by Cetas in "A Ferrite Core /Metallic Sheath Thermoseed for Interstitial Thermal Ablation" (Cetas et al. 1998) . Among these materials are Ni-Si, Fe-Pt, and Ni-Pd alloys. A number of magnetic powders were also tested in "Inductive heating of ferromagnetic particles and magnetic fluids: physical evaluation of their potential for hyperthermia" (Jordan et al. 1993) of which Ni-Zn-Fe-O, Ba-Co-Fe-O, and Fe-O looked promising. Gray et al. also proposes a promising material in US patent US6,599,234B1, "Heating of Magnetic Material by Hysteresis Effects" (Gray et al. 2003). This material is a substituted magnetite or ferric oxide crystalline lattice with a portion of the iron atoms substituted by one of the following; cobalt, nickel, manganese, zinc, magnesium, copper, chromium, cadmium, or gallium. Paulus et al. proposes a Palladium Cobalt alloy that also has a controllable Curie temperature in the range of 40-100 degrees Celsius in US patent US5429583 (Paulus and Tucker 1995).

2.1.2 Medically Safe Magnetic Field Limits

At increasing field frequencies and strengths, eddy current heating can be generated in body tissues. This safety concern places limits on field strengths and frequencies that can be used in medical applications. A number of researchers have made observations about this effect and developed safety limits. Atkinson, Brezovich, and Chakraborty in "Usable Frequencies in Hyperthermia with Thermal Seeds"(Atkinson et al. 1984) developed a simple model of heat production per unit volume tissue. Simplifying a body torso to a cylinder, they derived that $P = \sigma_t (\pi \mu_o)^2 (H_o f)^2 r^2$, where P= heat production per unit volume tissue, (W/m^3), σ_t= electrical conductivity of the cylinder, $(1/\Omega \cdot m)$, μ_o= magnetic permeability of free space $(1.257 \times 10^{-6} \text{ H} * \text{m}^{-1})$, H_o= magnetic field amplitude (A/m), f = field frequency *(Hz)*, and r = radius from center of cylinder *(m)*. It becomes apparent from this equation that the heating produced in the tissue is proportional to the square of the product, $H_o f$ and *r*. This means that tissue farthest from the center axis of the body would be subjected to the greatest heating rates. This being known Atkinson, Brezovich, and Chakraborty conducted experiments with numerous people and found that field intensities of 35.8 *A/m* at a frequency of 13.56 MHz could be tolerated for an extended period of time. They developed a safety limit of $H_o f \leq 4.85 \times 10^8 \, A \cdot turns/m \cdot s$ for whole body exposure. It was also pointed out that field strengths could be increased for extremities, such as the head or the arms since these portions of the body have smaller radii.

2.1.3 Field Generation

Inductively actuated SMP is only functional if it is exposed to the correct frequency and magnitude magnetic field. While the generation of this field is not a part of this thesis it is important for the realization of its application. Research in the field of Hyperthermia has not been limited to just the design of heating elements, much research has also gone into the development of induction coils and field generating machines specially suited for use in medical applications and well suited for producing the magnetic fields needed to actuate the proposed SMP with dispersed ferromagnetic particles. A quick overview of the literature will give a sense of the applicability of this research towards the implementation of inductively actuated SMP.

Different induction coil designs are presented by Stauffer et al. in "Practical Induction Heating Coil Designs for Clinical Hyperthermia with Ferromagnetic Implants" (Stauffer et al. 1994). This paper presents the field geometries and achievable field strengths generated by the different designs.

An inexpensive induction heating system for medical treatments is presented by Kimura and Katsuki in "VLF Induction Heating for Clinical Hyperthermia" (Kimura and Katsuki 1986) and Oleson gives a good overview of some basic coil designs in "A Review of Magnetic Induction Methods for Hyperthermia Treatment of Cancer" (Oleson 1984).

The possibility of using MRI machines for generating heating fields is also an attractive option, as many hospitals already have such equipment. This equipment uses an excitation RF magnetic field in the 30-60 MHz frequency (Jovicich 2004) that may possibly be used for heating magnetic particles. To the author's knowledge, no one has

investigated this possibility. More research needs to be done on the feasibility of this approach.

2.2 Modes of Magnetically Induced Heating

When a ferromagnetic material is exposed to an alternating magnetic field heat is produced; this is known as *power loss* (Zhen 1977). This heating is the result of a number of different microscopic mechanisms whose interactions are quite complicated and which have been studied and researched for most of the 20th century and continue to be researched today. Even with this rich history of research there has yet to be a reliable means of quantitatively predicting the macroscopic properties, including the *power loss* properties, of magnetic material from first principles (Wetzel and Fink 2001). It is still very useful to have at least a basic understanding of these microscopic mechanisms in order to understand what achievable heating rates are and to aid in the selection or possible creation of new materials that maximize heating and have the desired properties of Curie temperature and a loss mechanism which is mainly due to hysteresis instead of eddy currents. Although magnetic material development is largely a trial and error process, these basic principles can help in guiding this research in a more productive manner.

As described previously, the specific mechanisms that cause power loss can be grouped into two major categories: hysteresis loss, and eddy current loss. These two groups will be looked at separately.

2.2.1 Hysteresis Loss

A material's hysteresis loop is a measure of the hysteresis loss experienced by the material, with the area inside of the loop being equal to the magnitude of losses

experienced in one magnetic reorientation, i.e. one cycle. Each time the magnetic orientation of a material is switched, more heat is produced. It is important to understand that when referring to hysteresis and hysteresis loops in this thesis, it is the rate-independent definition that is used. Some researchers define hysteresis as including rate-dependant phenomenon such as eddy current loss (Bertotti 1998), and then make a distinction between rate-dependant and rate-independent hysteresis. The semantics and language of the magnetics research world are quite complicated and nuanced, but it has been the author's experience that it is more common in the literature to make a distinction between hysteresis and eddy current modes of heating rather then rate-independent and rate-dependent hysteresis. This being said, the rate independent definition of hysteresis and the methods used to measure hysteresis loops are somewhat artificial and tend to simplify intrinsically rate dependent phenomenon, as will be seen when the role of domain wall motion and magnetic rotation in hysteresis are discussed. The energy dissipated as heat via a single magnetic reorientation can be represented mathematically as (Zhen 1977).

$$E_h = \oint H dB \qquad \textbf{(1)}$$

If an alternating magnetic field is applied then the hysteresis loop is traversed once every cycle and the power loss can be represented as the following (Wetzel and Fink 2001)

$$P_h = f E_h \qquad \textbf{(2)}$$

where f is the frequency in Hertz. This equation is exact if the hysteresis loop is known for the processing parameters such as temperature, applied field amplitude, and frequency

(Wetzel and Fink 2001). However it is rare to find hysteresis curves for varying field frequency and temperature, and it is much more common to find DC saturation hysteresis loops, where the loop is measured under gradually varying field strengths at a constant temperature. The figure below depicts the common form of a DC hysteresis loop. The size and shape of these loops depend on and vary widely with not only the above mentioned parameters, but also with the composition of the material, and the metallurgical conditions of the material (Zhen 1977). Some hysteresis loops are narrow, wide, irregularly shaped, slanted, square, or some combination of these characteristics. As seen in the figure below some of the defining characteristics of a hysteresis loop are B_r, the remnance (units of Gauss, Tesla or $(kg/s^2\,A)$), B_s, the saturation magnetization (units of Gauss, Tesla or $(kg/s^2\,A)$), H_c, the coercivity (units of Oersted or (A/m)), and μ, magnetic permeability (units of (H/m) or $(m*kg/s^2\,A^2)$. B_r is the value of induction which remains in the material after magnetic saturation and after the magnetic field has been reduced to zero (Goldman 1990). B_s is the maximum attainable intensity of magnetization per unit volume of a ferromagnetic material (Zhen 1977). H_c is the value of the reverse field needed to reduce the induction of a magnetically saturated material back to zero (Goldman 1990). μ is the ratio of the material's induction , B, to the magnetizing field, H (Goldman 1990).

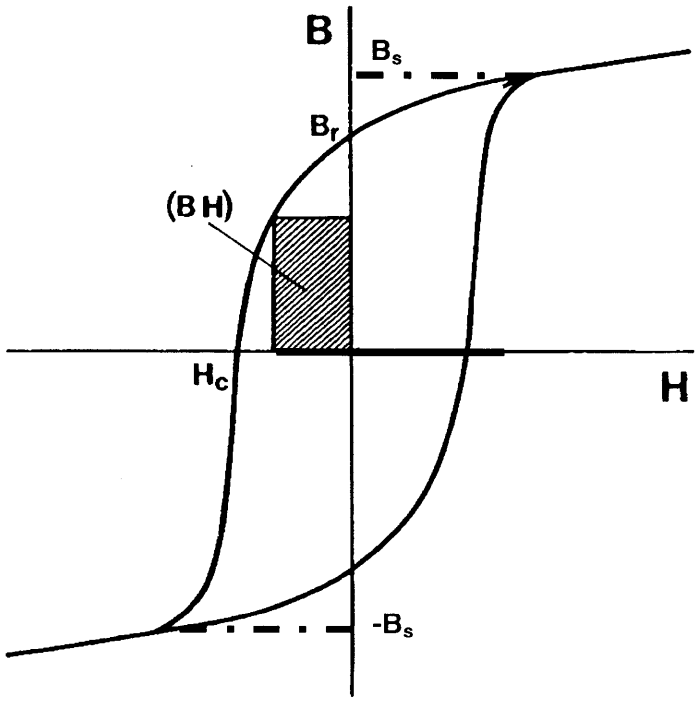

Figure 4: General form of ferromagnetic materials hysteresis loop (modified from (Goldman 1990)).

If a material is not forced to its saturation magnetization it will not trace its full saturation hysteresis loop. Instead, it will trace what is known as a minor hysteresis loop. The shape of this minor hysteresis loop tends to be similar to the shape of the saturation loop but the area inside the loop is less. The figure below gives an example of a range of minor hysteresis loops inside a saturation loop. The curve which points A, B, C, and D lie along is known as the magnetization curve. It represents the induction which is induced in the material when it is magnetized from a magnetically unorientated state.

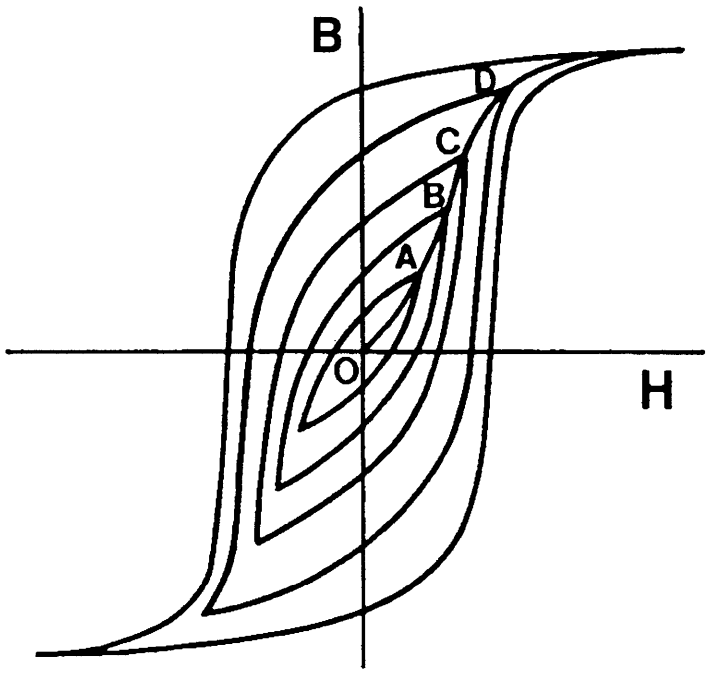

Figure 5: Minor hysteresis loops with magnetization curve (modified from (Goldman 1990)).

When you are attempting to heat a material via a hysteresis loss mechanism, it may be the case that you do not reach the full DC saturation hysteresis loop. This can be the case if the applied field is not strong enough to force the material to its saturation magnetization, and so the material traverses one of these smaller minor hysteresis loops. It can also be the case that temperature or the applied field frequency changes the shape of the hysteresis loop from that of the DC saturation hysteresis loop, making the loop smaller. These affects can be taken into account by adding a correction factor, c, to the power loss equation. This new power loss equation is shown below.

$$P_h = cfE_h \qquad (3)$$

To understand the mechanisms and properties which cause hysteresis heating, and determine the values of H_c, B_r, B_s and the size and shape of a materials hysteresis loop one must understand the concept of magnetic domains.

A macroscopic piece of ferromagnetic material is composed of numerous regions known as magnetic domains. A domain consists of material which is magnetically saturated and aligned in the same direction (Zhen 1977). Domains are usually on the size order of microns and contain around 10^{12}-10^{14} atoms (Goldman 1990). Magnetic domains are not the same thing as a material's microstructure; the size of a domain can be larger or smaller than the grain size of a material although it is rare to find domains larger than a material's grain structure (Bozorth and Metals 1959). The physical reason magnetic domains are formed in a material is to minimize the material's free energy. An example of this free energy is illustrated by the potential energy contained in field lines that connect north and south poles of a piece of ferromagnetic material. These field lines tend to travel outside the material and have a certain potential energy associated with them. This potential energy is known as magnetostatic energy (Goldman 1990). By creating domains, the length of these field lines can be shortened, thus lowering the free energy of the material. Domains will continue to be formed in a material as long as they reduce the material's energy by more energy than it takes to form new domains.

A ferromagnetic material's magnetic energy can be classified into four major categories: magnetostatic energy, magnetocrystalline anisotropy energy, magnetostrictive energy, and domain wall energy. Minimizing these four energies, as well as taking into account microstructural imperfections such as voids, non magnetic inclusions, and grain boundaries, will provide much information about the size, shape, and local variations in

domain structure which will in turn provide insight into a material's hysteresis loop (Goldman 1990). The domain structure of a material greatly affects which heating mechanisms are exhibited when a material is exposed to an alternating magnetic field. A brief overview of these four different forms of energy will be useful in understanding the forces involved in determining domain size and structure.

2.2.1.1 Magnetostatic Energy

Magnetostatic energy is the work which needs to be done in order to place magnetic poles in special geometric configurations (Goldman 1990). This energy can be calculated from a generalized equation found below (Goldman 1990),

$$E_{msta} = G_c d M_s^2 \qquad \textbf{(4)}$$

where G_c= constant determined by geometry of domain, d=width of domain, and M_s=magnetization intensity. From this equation it can be seen that magnetostatic energy decreases with the width of a domain. This is a driving force in making domains smaller and therefore increasing the number of domains in the same volume of material.

2.2.1.2 Magnetocrystalline Anisotropy Energy

Magnetocrystaline anisotropy energy is the greater amount of energy needed to create magnetic alignment in a 'hard' lattice direction rather than an 'easy' lattice direction. The 'easy' direction of magnetization may be an edge or a diagonal of the crystal unit cube (Goldman 1990). The anisotropy energy of the material can be lowered by aligning magnetic moments (ferrimagnetic material) or magnetic spins (ferromagnetic material) along an easy direction of the material (Goldman 1990).

2.2.1.3 Magnetostrictive Energy

A small change in dimension occurs when a magnetic material is magnetized or conversely when a magnetic material is stressed. The direction of magnetization will tend to align parallel or perpendicular to the direction of stress (Goldman 1990). The dimension change which occurs during magnetization is on the scale of several parts per million, but the energy associated with this can have an effect on domain size and structure (Goldman 1990). The magnetostrictive energy can be represented mathematically by the following equation (Goldman 1990),

$$E_{mstr} = 3/2\,\lambda\sigma \qquad \textbf{(5)}$$

Where λ = magnetostriction constant, and σ =applied stress.

Inducing stresses in a material during processing by machining, grinding, or for ferrites by firing can affect the magnetostrictive energy of a material and thus the domain structure and *power loss* mechanism (Goldman 1990).

2.2.1.4 Domain Wall Energy

A domain wall is that portion of a domain structure where the magnetization direction of one domain is gradually changed to the direction of a neighboring domain (Snelling 1969). In a 180° domain wall, the magnetic orientation direction changes 180° across the length of the domain wall, as illustrated in the figure below.

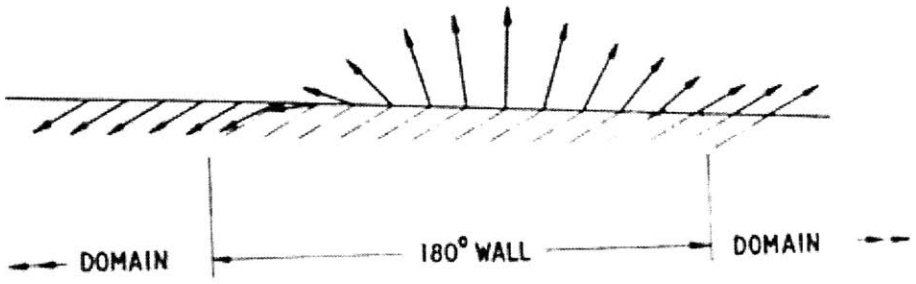

Figure 6: Illustration of a 180° domain wall (Snelling 1969).

The arrows denote the direction of magnetic orientation. There are also domain walls which differ by less then 180° in magnetic orientation.

If the domain wall thickness is ∂, this being proportional to the number of atomic layers in which the magnetic orientation changes from one domain to the other, there is a certain amount of energy stored in this transition due to spin interactions (Goldman 1990). This stored energy, known as exchange energy, can be represented mathematically as the following (Goldman 1990):

$$E_e = kT_c / a \qquad (6)$$

where k=Stefan Boltzman constant, T_c=Curie temperature, kT_c=thermal energy at the Curie point, and a= distance between atoms.

This shows that energy decreases as the width of the wall or the number of atomic layers in the wall is increased (Goldman 1990). There are, however, a number of other effects. If the material is crystalline, there is going to be a change in anisotropy energy as the magnetic orientation changes from an easy direction to a hard direction or vice versa across domain walls. Another effect is the magnetostrictive energy associated with the changing magnetic orientation across the domain wall. Accounting for these other effects, an equation which describes domain wall energy is the following (Goldman 1990).

$$E_w = 2(kT/a)^{1/2}(K_a + 3\lambda_s\sigma/2)^{1/2} \quad (7)$$

Where K_a = Anisotropy Constant and λ_s = saturation magnetostriction.

The typical values of domain wall energies are between 1-2 ergs/cm^2, with domain wall widths between 10^{-6} cm for soft magnetic materials and up to 10^{-4} cm for hard magnetic materials (Goldman 1990). The form and organization of magnetic domains in a material will be dictated mainly by the minimization of the above four energies (Goldman 1990).

2.2.1.5 Dynamic Losses at Domain Walls

When a material is exposed to a magnetic field, its domains begin to experience a reorientating force. Domain walls begin to shift and move in response to the magnetic field. Figure 7 (Snelling 1969) illustrates a simplified rendition of the magnetization process. The lines in the diagram represent domain walls and the dots represent voids or imperfections in the material. In (b) and (c), the domain which is most closely aligned with the applied field begins to grow, bulging, pushing, and engulfing the other domains that are not aligned with the applied field, much like a membrane bulging due to an applied pressure. At the lower field strengths the domain walls remain pinned by voids and imperfections in the material, preventing complete domain alignment. These initial domain movements are largely reversible and are restricted by the stiffness of the domain walls. In (d) we see what happens as the field strength is increased and the domain walls experience enough pressure to jump past voids and imperfections. These jumps are irreversible and are known as Barkhausen jumps. These are what cause hystereses heating in multi-domain ferromagnetic materials (Zhen 1977). In (e) and (f) we see the processes of domain rotation, where the orientation of the domain rotates and aligns with

the applied field. This magnetic rotation process tends to be reversible. At this point, the material is said to be saturated, and no further increase in magnetization is possible.

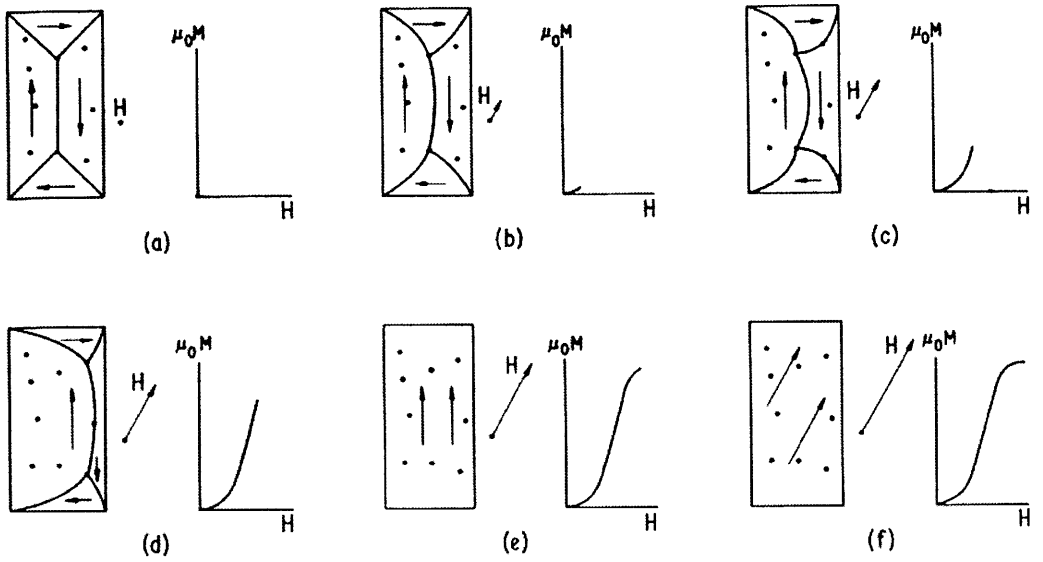

Figure 7: Simplified representation of domain boundary movement during magnetic reorientation (Snelling 1969).

This illustration is a simplified version of what happens in reality, but it gives a good overview of the basic role domain wall motion and magnetic rotation plays in the hysteresis *power loss* of multi-domain ferromagnetic material. It also gives some insight into how domain shapes and structures can influence the quantitative value of *power loss.*

The time scale that domain wall motion and magnetic rotation occur on are finite and thus the losses associated with them have some dependence on the rate at which the external field is applied. This is what was meant in section 2.2.1 when it was mentioned that hysteresis is inherently rate dependant.

At very high frequencies the material does not have time to respond to applied fields, and so does not fully magnetize (Wetzel and Fink 2001). This leads to different loss characteristics, which will be called low amplitude domain wall losses, since domain

wall motion is literally diminished in amplitude. It is conjectured that since the domains are not given enough time to fully reorientate, and undergo all the Barkhausean jumps at the higher frequencies, that heat generation from domain wall motion should be diminished at increasing frequencies. However, at a critical frequency a material enters a state of magnetic resonance, where low amplitude losses are maximized (Wetzel and Fink 2001). It is not known, and it is beyond the scope of this thesis, to determine whether the resonant low amplitude domain wall losses are comparable to the lower frequency domain wall losses, but it is something to keep in mind for future research. This magnetic resonance usually occurs somewhere between 100 MHz and 10 GHz (Wetzel and Fink 2001), and so is far above the frequencies used in this thesis.

Another interesting and potentially important change in loss mechanism occurs as particle sizes approach the size of single domains. In this case, typically reversible processes can become irreversible. For example, in single domain ellipsoidal particles it has been observed that hysteresis losses are generated solely by a magnetic rotational mechanism (Zhen 1977). The drastic difference in the *power loss* behavior of single domain or sub-domain size particles and multi-domain size particles is something that should be kept in mind when selecting the particle size of material that is to be used for inductive heating applications.

It is beyond the scope of this thesis to discuss the specifics of domain wall motion and magnetic rotation, but for further information on these topics I refer the reader to references (Magana et al. 1986), (Lin et al. 1984), (Escobar and Valenzuela 1983), (Kittel 1949), and (Bonet et al. 1999).

2.2.2 Eddy Current Loss

An electrically conductive material placed in an alternating magnetic field has alternating electrical currents induced within it (Wetzel and Fink 2001). The resistance to the flow of electrical currents through the material leads to the production of heat due to Joule (resistive) effects, and this is known as eddy current loss (Wetzel and Fink 2001). An illustration of how these eddy currents are induced to flow is illustrated in the figure below.

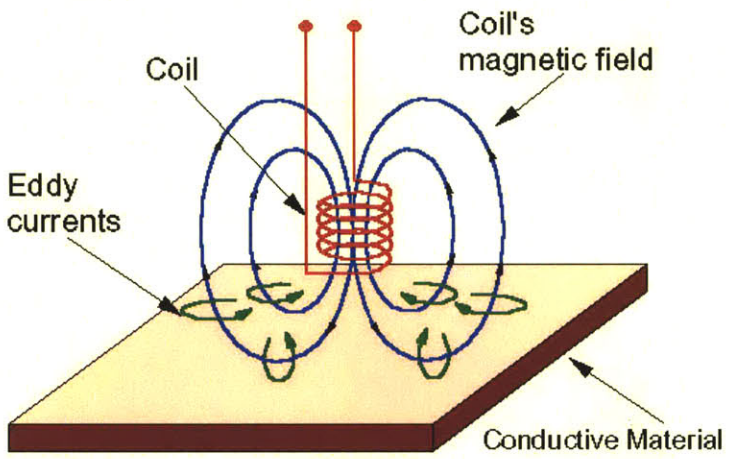

Figure 8: Illustration of induced eddy current. (http://www.ndt-ed.org/EducationResources/CommunityCollege/EddyCurrents/Physics/mutualinductance.htm)

Using Faraday's law, assuming a sinusoidally varying magnetic field and a spherical material geometry of diameter D_o,Wetzel, in "Feasibility of Magnetic Particle Films for Curie Temperature-Controlled Processing of Composite Materials" derives the following equation to describe the power loss associated with eddy currents (Wetzel and Fink 2001),

$$P_e = \frac{(\pi f B_p D_o)^2}{20\rho_\Omega} \quad \textbf{(8)}$$

where ρ_Ω is the material's resistivity (ohm-meter), B_p is the field amplitude (Tesla), f is the field frequency (Hz), and P_e the volumetric power dissipation (W/m^3).

The eddy current heating mode is not controlled by the Curie temperature of the material because the loss mechanism is caused via the Joule heating caused by the flow of electrical currents. If an electrically conductive material is heated above its Curie temperature, it will still heat via an eddy current loss mechanism because the material is still electrically conductive, thus offering no Curie point thermoregulation. For this reason it is desirable to minimize the eddy current heating mechanism of the heating particles dispersed in the SMP. As can be seen from the above equation, reducing the particle diameter and increasing the material's resistivity will reduce the magnitude of the eddy current losses. It may not be possible to completely eliminate eddy currents, but if they are minimized so that they only contribute a small fraction of the energy for heating, with the majority of the energy for heating being generated by a hysteresis loss mechanism, the advantages of the Curie temperature thermoregulation can still be realized.

3 Materials

3.1 Shape Memory Polymer and Sample Preparation

The SMP material used was an esterbased thermoset polyurethane, MP 5510, purchased from Memry Corp., distributor for Mitsubishi Heavy Industries, Ltd. One of the major reasons this class of SMP was used is that polyurethanes are generally biocompatible, making them particularly well suited for medical applications involving internal short-term use (Lamba et al. 1998). The material was supplied in a two part liquid system consisting of a resin (A) and a hardener (B).

Because certain factors in the environment, such as air humidity and room temperature, were not controlled during sample preparation, these parameters were recorded so that their potential affects could be identified. All prepared samples were stored in a desicator to ensure a consistent dry storage environment. No significant effects on the mechanical properties of SMP due to the moderate changes in room humidity (32%-56%) or room temperature (22°C-24°C) between sample preparations were noticed.

Two types of sample geometries were prepared, a cylindrical rod for DMTA testing, and a flat rectangular sample for recovered tensile strain testing. The heating samples were also obtained from these flat pieces by using a 9.52mm circular punch to make disc shaped samples that would fit inside a test tube. It is worth noting that attempts were made to use the flat rectangular samples for DMTA testing, but difficulty with test repeatability was encountered. The cylindrical rod samples yielded more repeatable DMTA test results. A picture of the mold used to make these flat rectangular samples is shown in the figure below. This mold had two levels allowing 12 samples to be made in one molding cycle.

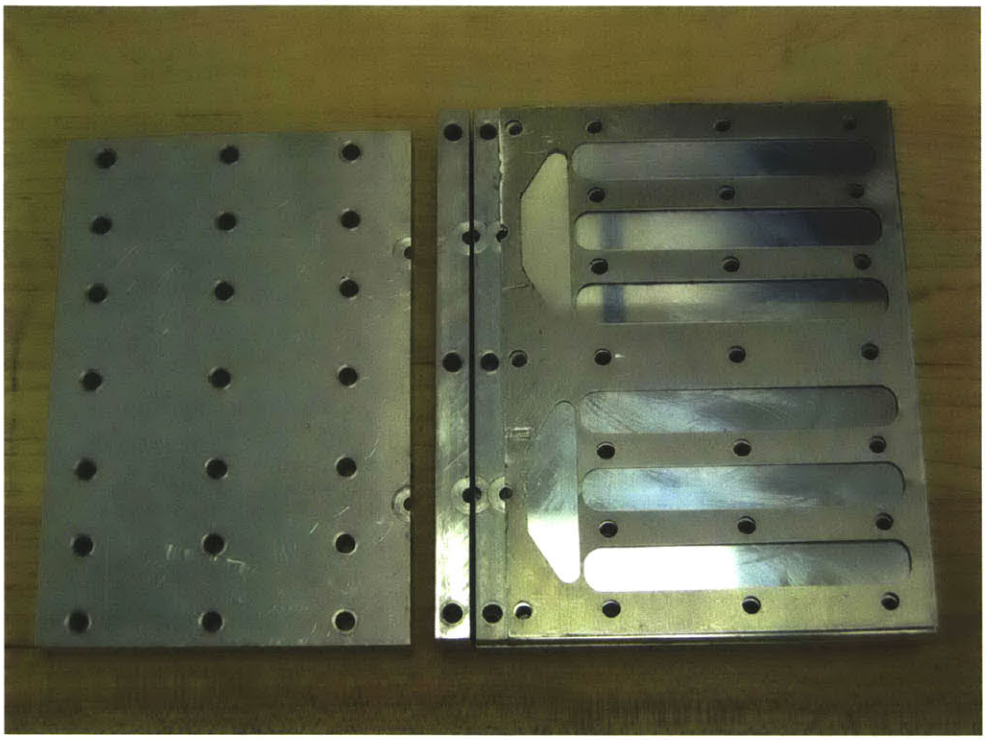

Figure 9: Mold used to make flat rectangular samples.

The cylindrical rod samples were prepared by drawing SMP into a 1ml Becton Dickinson tuberculin syringe and allowing it to harden in this form. The sample was then recovered by cutting the ends off the syringe and pulling the hardened SMP rod out. These samples had a diameter between 4.65mm and 4.70 mm. The flat rectangular samples were prepared using the mold pictured above. The mold allowed four different types of samples to be prepared in one molding run and was designed so that three of each sample type were molded at once. This allowed a total of 12 samples to be made in one molding run, a molding run being one curing cycle at 80°C. The samples had the following geometry: width of 12.5 mm, thickness of 1mm, and length of 80mm. Manufacturer recommended procedures were used when preparing samples. The procedure used was as follows:

1. Components A and B were vacuum dried for 60 minutes at 80°C under vacuum.

2. Components were then allowed to cool to room temperature while being stored in a desicator to ensure a dry environment.
3. Mold surfaces were cleaned using acetone and were treated with one of the following release agents: DuPont FEP solution with fluropel PFC 801A additive, or TFE MS-122V Teflon spray from Miller Stevenson. After this treatment the mold was dried under vacuum in an oven for one hour at 80°C under vacuum. After this drying the mold was reassembled and set aside.
4. If a sample called for the addition of magnetic particles, they were added to component B and mixing was performed by hand using a mixing stick, a vortexer machine, or a combination of these two techniques.
5. Components A and B were mixed together in the following ratio, A:B 2:3 by weight, using the same method as above. It should be noted that this ratio was calculated before the addition of magnetic particles, so the weight of particles did not factor into this ratio.
6. The mixture was degassed under a vacuum for approximately one minute or until bubbling had subsided.
7. The mixture was then poured into a syringe and immediately injected into the mold until excess poured out of the relief ports, or was drawn into 1ml Becton Dickinson tuberculin syringes.
8. The SMP began to harden in about 3 minutes time, making it necessary to move quickly when mixing and injecting the SMP mixture.
9. After injection, the samples were allowed to sit at room temperature for a minimum of one hour.

10. The molds were then placed in an oven and cured at 80°C for a minimum of 4 hours.

3.2 Nickel Zinc Ferrite Particles

Ferrites are an attractive class of material for Curie temperature thermoregulated inductive heating. As mentioned previously, it is important to maximize hysteresis losses while minimizing eddy current losses in order to ensure a thermoregulation set by the Curie temperature. Ferrite's very high resistivity, on the order of 10^6 to 10^{10} ohm-cm, helps to minimize eddy current heating (Zhang 2003). Ferrites also have other attractive qualities such as environmental stability, a wide range of material compositions and magnetic characteristics, and an adjustable Curie temperature through Zn substitution (Zhang 2003). This last quality of an adjustable Curie temperature is illustrated below in the below figure for a nickel zinc ferrite material.

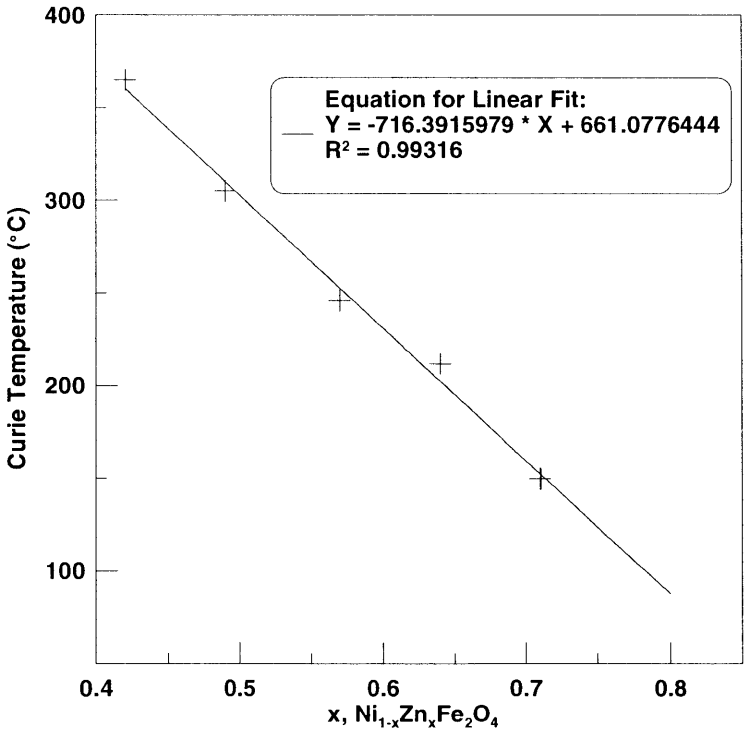

Figure 10: Effect of Zn substitution on the Curie temperature of NiZn ferrite (Zhang 2003).

The above figure illustrates how much a ferrite's Curie temperature can be affected by Zn substitution and how easy it is to predict a Curie temperature from the amount of Zn in the ferrite. There are other effects of adding Zn to a ferrite material that are not as easily pre-determined. An example of this is the change in a ferrite's magnetic coercivity. This property does not have a nice linear response to Zn substitution.

Three compositions of NiZn ferrite were used in this thesis. The composition of these materials was unknown but they were all obtained from Ceramic Magnetics Inc.. The three classes of material used were C2050, CMD5005, and N40. According to the manufacturer, C2050 and N40 were specifically designed for use in applications up to 1000 MHz in power supplies, linear amplifiers, UHF, and VHF. N40 was designed for applications between 1-100 MHz in pulse applications, RF power amplifiers, current transformers for EMP, and deflection magnets for particle accelerators. The smallest particle size available from the manufacturer was said to have an average size of 50μm, and was obtained from the 'fines' of the manufacturing process. Due to the processing technique these particles had a spherical shape to them. The following material properties were supplied by the manufacturer, with the exception of the densities, which were measured by the author using a standard volume displacement technique.

	C2050	CMD5005	N40
Initial Permeability	100	1600	15
Max Permeability	390	4500	50
Max Flux Density* (gauss)	3400	3000	1600
Remnant Flux Density* (gauss)	2400	1800	700
Coercive Force* (oersted)	3.0	0.23	7.5
Curie Temperature (°C)	340	130	510
Density (g/cm^3)'	5.57	6.16	5.65
Resistivity (ohm-cm)	10^6	10^9	10^{10}

Table 2: Magnetic and material properties of Nickel Zinc Ferrite used in sample preparation. (* designates measurement taken at 40 oersted applied field strength)(' designates values which were measured by author and not provided by the manufacturer)

A fourth material, magnetite (Fe_3O_4), also known as iron oxide, was obtained from Nanostructered & Amorphous Materials inc., and also experimented with. The manufacturer claimed a particle size of 20-30 nm and a spherical particle shape. When attempts were made to disperse this material into SMP, two problems were encountered. One was that the SMP began to foam, making it impossible to make useful samples, and second, the particles did not appear to be the 20-30nm size which the manufacturer claimed. Using light microscopy to view the particles, it appeared that they had aggregated into larger, irregularly shaped particles on the size scale of 10's of microns.

Two techniques were employed to combat these problems. The first was to dry the powder in an attempt to eliminate all the moisture that may have been trapped in the material. It was hypothesized that this water may have been causing the SMP to foam. The material was spread out on a sheet and vacuum dried at 200°C for 4 hours. This appeared to reduce the foaming but it did not eliminate the problem. Second, a dispersant

was used to try and break up the particle aggregates, The dispersant used was Disperbyk-116 from BYK Chemie. It appeared to have minimal effect and caused the SMP to soften, which was undesirable. Due to time limitations the use of this material had to be abandoned. Future work needs to be done to see how this material might be used in SMP, as it shows promise as a heating material.

The NiZi ferrite material was prepared, dried and sorted according to the following procedure:

1. Material was sorted for 15 minutes using a WS tyler model RX-29 shaker and the following mesh screens: 53μm, 43μm, 25μm, 16μm, and 8μm pore sizes.
2. Some of the material larger then 53μm was ball milled for 5 hours using a United Nuclear 3 lbs. ball mill and 1.27cm diameter stainless steel balls. These balls were recommended by and purchased from Ceramic Magnetics inc., the manufacturer of the Nickel Zinc ferrite powder.
3. Ball milled material was vacuum dried at 200°C for 4 hours. All other material was vacuum dried between 80-90°C for at least 1 hour. The ball milled material was dried at this higher temperature because it exhibited a resistance to drying at the lower temperature.
4. After drying, the material was stored in a sealed glass jar inside a desicator. This was done to ensure a dry environment for all samples.

Particle size was determined by dispersing a small amount of powder in glycerol and mounting the suspended particles on a slide. Light microscopy was used to magnify the image by 200x and a digital photo was taken. A photo of a 1mm ruler dash under the same magnification was also taken in order to serve as a calibration distance. These

photos were then analyzed using a digital image processing program named ImageJ. This program was obtained from the NIH website, http://rsb.info.nih.gov/ij/. A scale was determined by measuring the number of pixels present across a 1 mm distance. Next, the threshold command was used to convert the images of the suspended particles into black and white. It was assumed that particles were of a spherical shape and so would have an image area of $\pi\left(\frac{D}{2}\right)^2$, where D is the diameter of the particle. A minimum and maximum pixel rejection setting was set to + 10μm and -10μm of the maximum and minimum screen mesh size the particles were sorted between. For example, the powder collected between the 53μm and 43μm mesh screens had a maximum and minimum pixel setting such that the maximum and minimum diameter counted as a particle was 63μm and 33μm respectively. For the powder collected between the 25μm and 16μm mesh, this maximum and minimum diameter particle setting was 35μm and 6μm respectively. Because the ball milled material was not sorted through a mesh, the maximum and minimum diameter size particle rejection was set to 53μm and 1μm respectively. The method described above, using the above mentioned settings, gave average particle diameters presented in the table below.

Preparation Description	53μm - 43μm	25μm-16μm	Ball Milled 5 h
Average Particle Diameter	43.6μm	15.4μm	6.71μm

Table 3: Average diameter of ball milled and sorted powders as calculated using ImageJ digital image processing.

4 Inductive Heating Tests

4.1 Equipment and Field Strengths

The induction heating equipment used in this thesis was selected primarily based on a budget constraint. This constraint limited the frequency and field strength of the equipment that could be obtained. A machine that could generate a high frequency, on the order of MHz instead of kHz, and lower amplitude field strengths, on the order of A/m instead of kA/m was selected because it was more affordable. This high frequency/low field strength approach to heating is not necessarily the best approach and it may be useful to investigate the use of lower frequencies and higher field strengths in the future. The machine used for induction heating tests was an Ameritherm Nova 1M power supply with a remote heat station with faraday cage and a copper wound solenoid coil with a 2.54cm diameter, 7.62cm length, and a total of 7.5 turns. This unit had an adjustable power setting capable of outputting 27 to 1500 Watts at between 10 and 15 MHz frequency. This frequency could not be adjusted manually; it was determined by the inductance of the coil, so if a change in frequency was desired, a coil with a different number of turns would have to be used. This was not a concern for the tests conducted for this thesis because only one coil and thus one frequency was used. The tubing that the solenoid coil was made from was hollow, so cooling water could be run through it to ensure that the coil did not overheat. This water was then cooled in a water to air heat exchanger. A photograph of the unit layout is shown in the figure below.

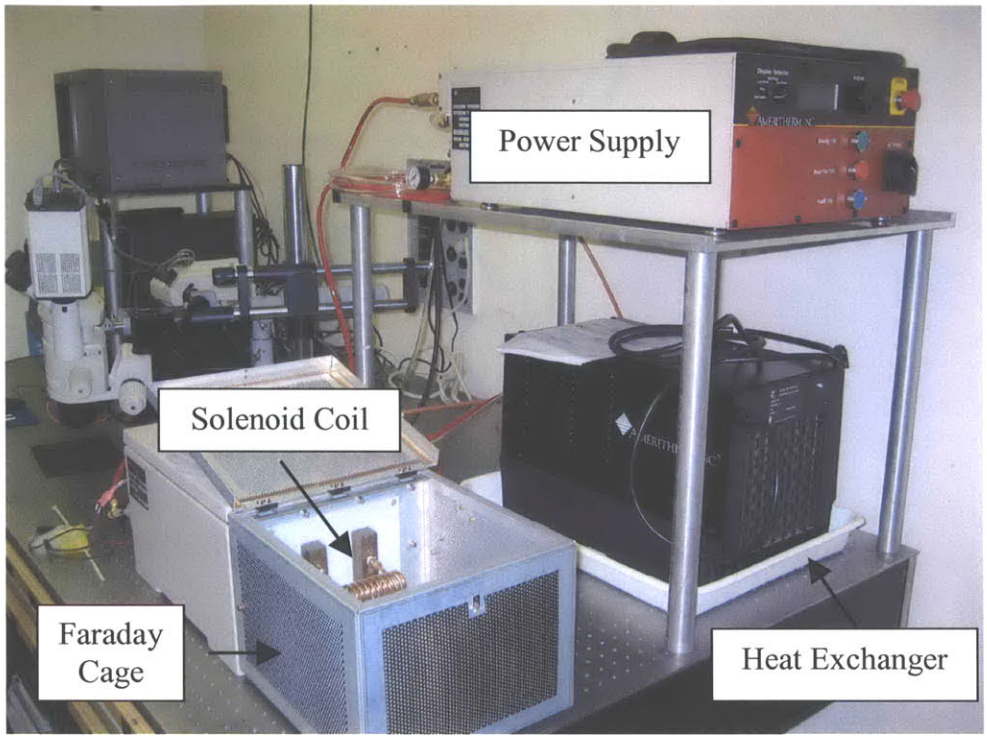

Figure 11: Ameritherm Nova 1M Induction Heating unit with remote heat station, faraday cage, and heat exchanger.

To determine the magnetic field strength generated in the solenoid coil it was necessary to perform some tests to characterize the system. The impedance of the 7.5 turn solenoid coil was measured using a Hewlett Packard 4285A 75kHz-30MHz LCR meter. At a frequency of 12.96MHz, a value of 525 nH was obtained for the coil. The voltage drop across the coil was then measured at a number of different machine power settings. To make these measurements a 20:1 voltage divider was made and hooked to an oscilloscope. Assuming that the electrical resistance of the copper coil was negligible compared to the resistance created by the inductive reactance, it becomes possible to calculate the current through the coil using the following equations:

$$2\pi fL = X_L \qquad \textbf{(9)}$$

$$\frac{V}{X_L} = i \qquad \textbf{(10)}$$

where L is the impedance in Henry, f is the frequency in Hz as measured using an oscilloscope, X_L is the inductive reactance, V is the rms voltage as measured using an oscilloscope in volts, and i is the calculated current in Amps. It was only possible to take voltage reading up to a power setting of 800 Watts because the resistors in the voltage divider began to overheat. It was desirable to have an estimate for the current flow at power settings up to 1000 Watts, so the points were plotted and a fit was made to the data. A log fit was found to have the highest coefficient of determination, R^2, of all the fits tried and so was used to extrapolate values of current for power settings up to 1000 Watts. This fit and the equation for the line can be seen in the figure below.

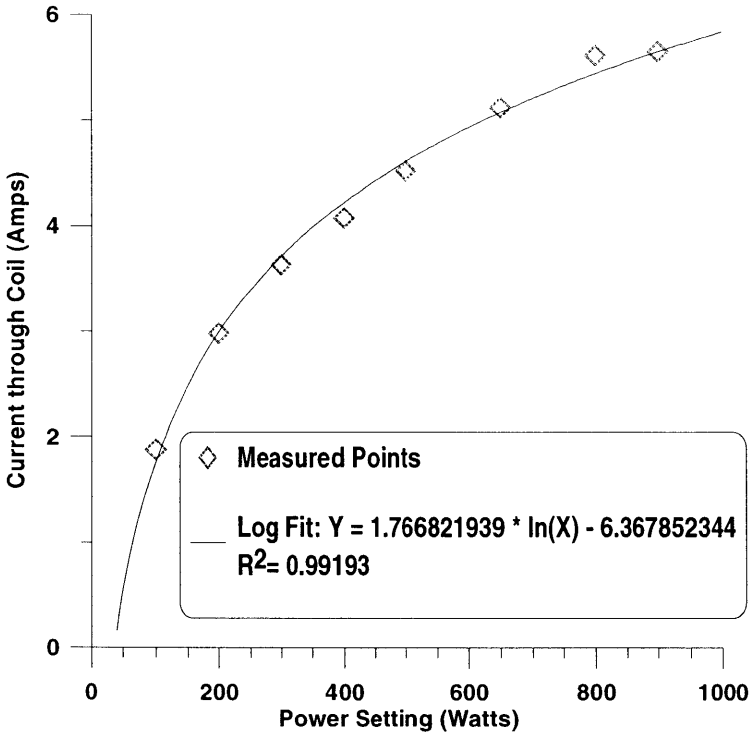

Figure 12: Measured coil currents and log fit for extrapolation of currents out to power setting of 1000 Watts.

Once the current through the coil was determined, it became possible, using Biot Savarts law, to develop a mathematical model to determine the field strength inside the

coil. Assuming the coil can be modeled as an ideal solenoid, the magnetic field at the center of the coil can be described as follows (Rudnev 2003),

$$\frac{\mu_o Ni}{\sqrt{(4R^2 + L^2)}} \times \frac{10^7}{4\pi} = H \qquad \textbf{(11)}$$

where μ_o is the permeability of free space and is equal to $4\pi \times 10^{-7}$ Henry/meter, N is the number of turns in the coil, i is the current through the coil in amps, R is the coil radius in meters, L is the coil length in meters, $\frac{10^7}{4\pi}$ is a conversion factor, converting from units of Tesla to amps/meter, and H is the field strength in A/m.

Using the above techniques the magnetic field strength at the center of the coil was calculated, and the values obtained are shown in the table below.

Power Setting (Watts)	H (A/m)
100	175.4
200	278.4
300	338.8
400	380.5
500	422.3
650	478.0
800	524.4
900	527.6
1000	545.0

Table 4: Calculated value of magnetic field with corresponding power setting of power supply.

4.2 Testing Procedure

A calorimeter was made using a 2.54cm diameter styrofoam cylinder. A 1.27cm hole was bored through the center of the styrofoam to accommodate a 1.27cm diameter plastic test tube. A Styrofoam top was fashioned to cover the exposed top of the test tube. This configuration left a 6.35mm thick wall of insulating styrofoam around the entire test tube; this was seen as sufficient to prevent significant heat loss over the time scale of the testing, which was no longer then 45 seconds per sample.

12 different SMP samples with varying magnetic particle sizes, volume content, and material types were tested. The information on the samples' makeup is presented in the table below. There was also a control sample tested, which is not shown in the table below. This control was an SMP disc of the same geometry as the other samples but with no magnetic particles.

Particle Volume Content (%)	Materials and Particle Diameters tested		
	C2050	CMD 5005	N40
1	43.6μm, 6.71μm	X	X
5	43.6μm, 6.71μm	X	X
10	43.6μm, 15.4μm, 6.71μm	43.6μm	43.6μm
20	43.6μm, 6.71μm	X	X

Table 5: Composition of heating samples tested.

The heating samples were prepared by punching 9.52mm circular pieces from the 1 mm thick rectangular samples prepared for and used in the tensile strain recovery tests. A 9.52mm leather hole punching tool and a hammer were used to do this. Each of the 12 samples was placed in its own test tube and 4 ml of double distilled and deionized water was added to the test tube, as measured using a 5000 micro-liter Eppendorf Research pipette, model 436324. Regular tap water was used at first but it was soon realized that the frequency and field strength being used was directly and rapidly heating the tap water. It is believed that there was a coupling between the magnetic field and the dissolved minerals and salts in the water, which caused this heating. Each test tube was covered with a paraffin film to ensure that water did not evaporate between tests.

The heating tests were performed by placing a test tube in the Styrofoam calorimeter, stirring the entire unit using a vortexer to help ensure there was a convective flow of water over the sample to help dissipate the heat generated by the sample into the water. The calorimeter with the test tube and sample loaded into it was then placed into

the heating coil and positioned such that the sample was roughly in the center of the coil. The position of the calorimeter in the heating coil was constant for all tests thanks to the use of a stop set in the coil. An alternating magnetic field was then applied for a designated amount of time. The calorimeter was then immediately removed from the coil and the temperature rise of the water measured using a thermocouple set up. This set up consisted of two Omega T thermocouples hooked to an Omega model HH23 microprocessor thermometer. One thermocouple was placed in a test tube with 4 ml of water and allowed to remain at room temperature, this served as the base line temperature measurement. Before any testing was performed, the temperature of the water in all test tubes was allowed to equilibrate with room temperature, and so it was assumed that before heating the temperature of all test tubes was the same as that of the baseline thermocouple measurement. A second thermocouple was fed through a narrow stainless steel tube which protruded down from a Styrofoam top which fit over the top of the test tube; this was the probing thermocouple. Immediately after the alternating field had been applied to the sample, the thermocouple fitted top replaced the plain top and the narrow stainless steel tube punctured the paraffin film and protruded into the water, allowing the thermocouple to measure the temperature of the water. Both the baseline thermocouple and the probing thermocouple were hooked into the Omega microprocessor thermometer which subtracted the probing thermocouple temperature from the base line temperature and then displayed the calculated temperature rise of the water. Prior to any testing the two thermocouples were zeroed out against each other. This involved placing both thermocouples into the same test tube of water and recording any difference in temperature measurements the two thermocouples displayed. This difference was then

added or subtracted from the test results, depending on if the baseline or probing thermocouple recorded a higher temperature during this zeroing procedure. The correction factor was never greater then 0.3 °C.

Tests were performed at a power setting of 500 and 1000 Watts on the Ameritherm power supply. These settings correspond to field strengths of 422 and 545 A/m as calculated using the above method. Heating curves for all the samples at these two field strengths were generated by measuring the temperature rise for a number of different field exposure times. These times and the number of repeat tests performed are shown in the table below.

Field Strength (A/m)	Field Exposure Time (sec)				
	5	10	20	30	45
422	0	III	III	III	III
545	III	III	III	0	0

Table 6: Testing times and field strength, roman numerals represent the number of repeat tests performed at each setting and time.

A few samples, namely the 10% volume content 15.4μm and 43.6μm particle diameter and 20% volume content 43.6μm particle diameter C2050 samples, experienced rapid heating at the 545 A/m field strength setting. These samples began to melt at the 20 second time setting and so were not tested at this time setting. It appears that for the testing setup used sample melting began to occur when heating rates of the water were greater than .300 K/s. A severe case of this is shown in the figure below. In some cases this melting appeared to be polymer degradation, the proof of this being a white residue left on the surface of the melted polymer samples. This heating rate corresponds to an average volumetric power generation in the SMP samples of 82 W/cm^3. If this material is ever used for a medical device and the heating and actuation of the device is to occur over the course of 20 seconds it will be safest to be below this 82 W/cm^{3}average

volumetric power generation. This is just a rough guideline, as there will be other factors, such as the device's surface area and the flow of blood around the device that will affect how efficiently the device is cooled.

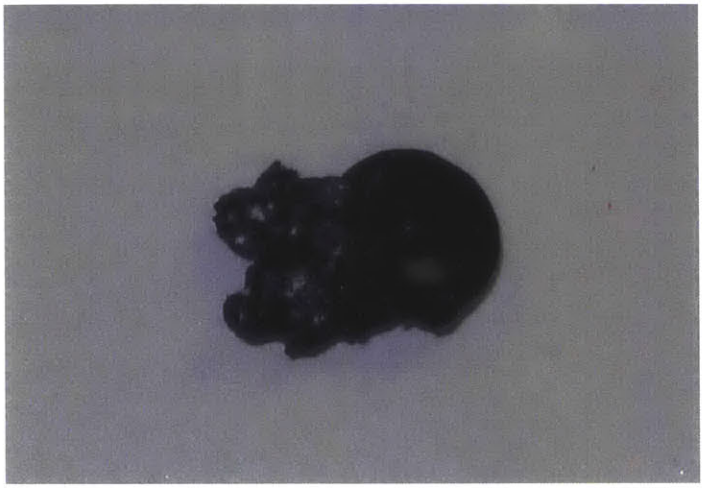

Figure 13: Example of melted calorimetry sample, initially circular in shape.

4.3 Test Results

The heating curves from Appendix A were used to calculate a rate of power generation for each set of testing parameters. Power generation of the samples is the same as the power loss, or power dissipation, discussed in Chapter 2; these wordings will be used interchangeable. Two assumptions were made about the heating process that greatly simplified the calculations that needed to be done. The first assumption was that the heat lost to the environment due to convection over the time period of the test was negligible. A calculation was performed which estimated the coefficient of convection to be 4.507 W/m^2K for the geometry of the calorimeter and free air convection. Using this number the time for the system to reach 95% of its steady state temperature, meaning that the amount of heat being inputted into the system is approximately equal to the amount of heat being carried away by the environment, was calculated to be 464.4 seconds. This is an order of magnitude longer time then the longest test, which was 45 seconds. In

addition to this, the temperature rise data did not appear to be approaching any steady state value, as would be expected if the system was losing significant heat to its surroundings. The second assumption made was that the mass of the sample disc had negligible effect on the thermal properties of the system. This was seen to be a fair assumption since the sample disc was less than 3%, by mass or volume, of the 4 ml of water. Using these two assumptions, the power generated by the magnetic particles is equal to the power needed to heat the 4ml of water. This allows the power generated in the magnetic particles to be calculated using the following equation:

$$\frac{\rho_w c_p v_w}{v_p}\frac{dT}{dt} = P_g \qquad \textbf{(12)}$$

where ρ_w is the density of water in units of g/cm^3, c_p is the specific heat of water in units of J/gK, v_w is the volume of water in units of cm^3, v_p is the volume of magnetic particles in units of cm^3, *dT/dt* is the rate of temperature increase of the water in units of K/s, and P_g is the volumetric power generation of the material in units of W/cm^3.

In reality there are slight losses of heat to the environment that are not accounted for in this equation. This means that, if anything, the calculated values of power generation are underestimated. For the above mentioned reasons, the calculated values should not be significantly erroneous. It is potentially useful to know in which direction potential errors lie.

The slopes of the fitted lines shown in the graphs of Appendix A were used as the values of dT/dt for calculating the volumetric power generation. The volumetric power generation of the magnetic particles was corrected by subtracting the rate of temperature increase of the plain SMP sample from the rate of temperature increase of the

magnetically loaded SMP samples. This ensured that the calculated power generation was due solely to the magnetic particles and not due to the heating of the SMP. The average volumetric power generation of the samples was calculated using the volume of the entire sample chip instead of just the volume of the magnetic particles, so v_p in equation 12 was set equal to the volume of the sample instead of just the volume of the magnetic particles. Also the average volumetric power generation is calculated from the uncorrected *dT/dt* values, as the purpose of this average value is to represent all heating that occurs in the sample materials, magnetic particles, and SMP matrix. The volumetric power generation data from the heating curves in Appendix A is presented in the tables below.

Magnetic Material	Volume %, Particle Diameter	Volumetric Power Generation of Magnetic Particles (W/cm^3)	Average Volumetric Power Generation of Samples (W/cm^3)
C2050	1, 6.71 μm	219	6.7
C2050	1, 43.6 μm	527	9.7
C2050	5, 6.71 μm	252	17.1
C2050	5, 43.6 μm	436	26.3
C2050	10, 6.71 μm	187	23.1
C2050	10, 15.4 μm	356	40.1
C2050	10, 43.6 μm	375	42.0
C2050	20, 6.71 μm	135	31.4
C2050	20, 43.6 μm	282	60.9
N40	10, 43.6 μm	292	33.7
cmd5005	10, 43.6 μm	311	35.6
None	Plain SMP	X	4.5

Table 7: Volumetric Power Generation of magnetic particles and Average Volumetric Power Generation of samples for 12.2 MHz and 422 A/m magnetic field.

Magnetic Material	Volume %, Particle Diameter	Volumetric Power Generation of Magnetic Particles (W/cm^3)	Average Volumetric Power Generation of Samples (W/cm^3)
C2050	1, 6.71 μm	596	12.8
C2050	1, 43.6 μm	1100	17.9
C2050	5, 6.71 μm	546	34.1
C2050	5, 43.6 μm	846	49.1
C2050	10, 6.71 μm	429	49.7
C2050	10, 15.4 μm	755	82.4
C2050	10, 43.6 μm	825	89.3
C2050	20, 6.71 μm	316	70.0
C2050	20, 43.6 μm	625	132
N40	10, 43.6 μm	521	58.9
cmd5005	10, 43.6 μm	529	59.8
None	Plain SMP	X	6.8

Table 8: Volumetric Power Generation of magnetic particles and Average Volumetric Power Generation of samples for 12.2 MHz and 545 A/m magnetic field.

4.3.1 Hysteresis Loss or Eddy Currents

For inductively heated SMP it is important to determine whether the magnetic particle material is heating via eddy currents or hysteresis loss. This determination will tell us if we can expect the material to have a Curie temperature thermoregulation mechanism. No tests were done to see if heating was limited by the Curie temperature of the materials. Testing the materials to see if they would stop heating in an alternating magnetic field once they reached their Curie temperature would be an easy way to test if the material was heating primarily by hysteresis loss; if the material heated beyond its Curie temperature this would indicate that there was heating via eddy current losses. Unfortunately, there was not time to run these tests, but these tests should be kept in mind for future work. Despite not doing this test there is other evidence that suggests that the material used was heating mainly via hysteresis losses. According to equation **(8),** which describes eddy current losses in a spherical particle, the particle size and material which would generate the largest amount of heating via eddy currents of all materials tested

would be 43.6μm particle diameter C2050. Calculations done using this equation revealed that there should only be a volumetric power generation due to eddy currents of $6.54*10^{-6}$ W/cm^3. When this is compared to the 500-1000 W/cm^3 recorded for this material during testing it becomes clear that if this equation is indeed accurate, which it should be, then eddy current losses are negligible. It is therefore fair to assume that the materials tested in this thesis were heating primarily via hysteresis losses.

4.3.2 Field Strength

It can be seen clearly that the power generated by the particles is greater for the higher field strength. This is an expected result, because as the magnetic material is forced to trace a larger minor hysteresis loop, due to larger magnetic field strengths, the material will undergo greater magnetic losses due to domain wall motion as described in Chapter 2. This leads to a greater amount of heat generated by the material.

4.3.3 Volume Fraction

One unexpected trend that is present in this data is that there appears to be a decrease in the volumetric power generation of the magnetic particles as the volume fraction of particles in the SMP increases. This can be seen at both the higher field strength and lower field strength. This trend is presented in the two figures below.

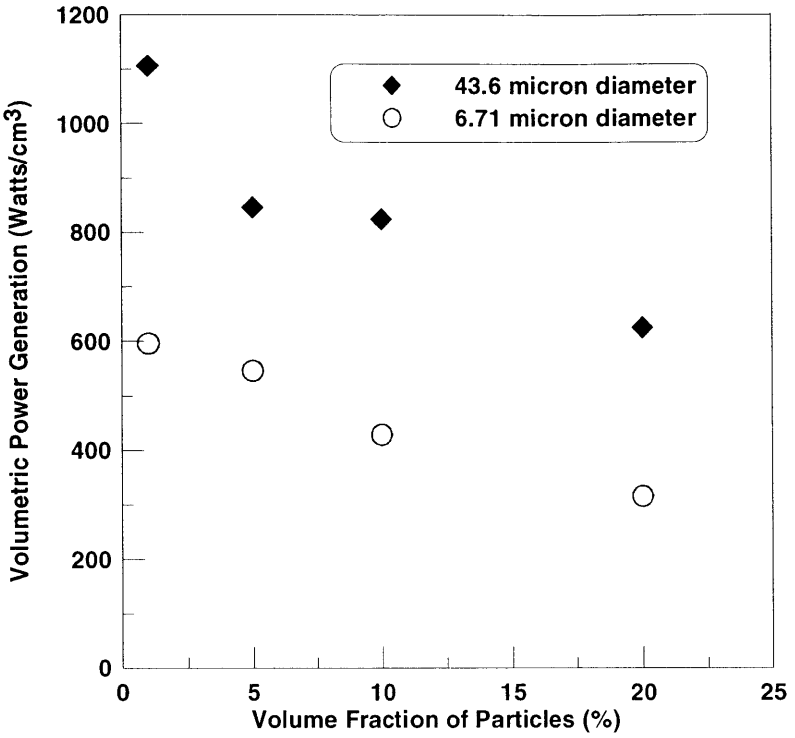

Figure 14: Volumetric Power Generation of magnetic particles vs. Volume Fraction of Particles, 12.2 MHz and 545 A/m.

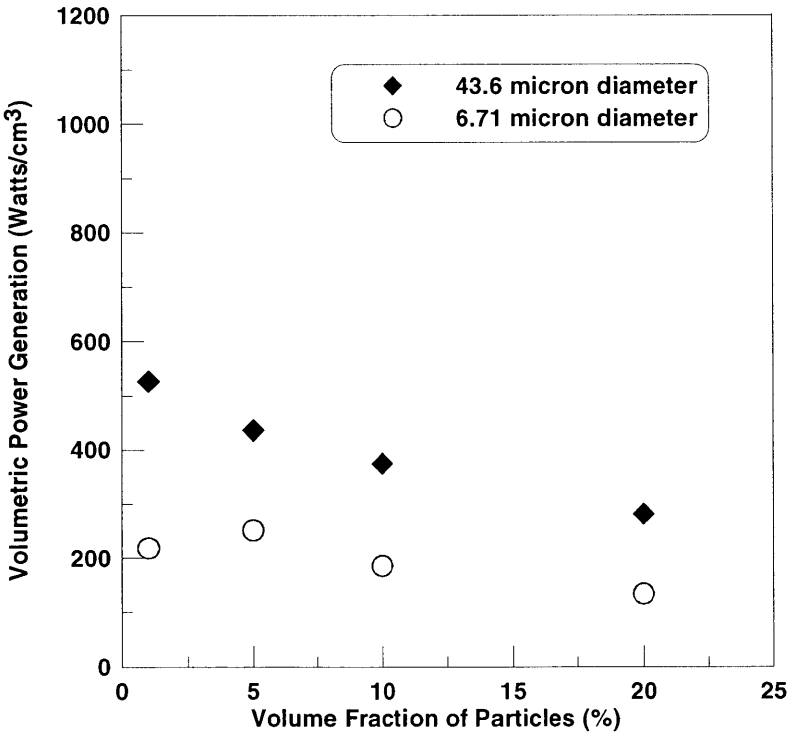

Figure 15: Volumetric Power Generation of magnetic particles vs. Volume Fraction of Particles, 12.2 MHz and 422 A/m.

There are two possible causes for this trend; one is that the inaccuracies of measuring small temperature rises affected the lower volume content samples to a greater degree than the higher volume content samples. It is possible that this inaccuracy led to the lower volume fraction samples having an artificially higher temperature reading recorded for them. The thermocouples used only measured temperatures to the closest 0.1 K and there appeared to be a greater variation of readings at lower temperatures, as can be seen by the error bars of the 1% and 5% volume fraction samples in Appendix A. As the volume percent of the particles increased to 10% and 20%, the temperature rise measured during experiments also increased and the error caused by the limited 0.1K resolution of the thermocouple had less of an effect on the data, as can be seen by the tighter error bars for the 10% and 20% volume fraction samples in Appendix A. The second possibility is that as the particle volume percentage increases the magnetic particles began to have a shielding effect on each other. This shielding would lower the magnetic field strength experienced by the particles and thus lower the volumetric power generation of the particles in the sample. Investigating the possibility of such a shielding effect is beyond the scope of this thesis but it may be a topic for research in the future.

4.3.4 Particle Diameter

Another interesting trend can be identified by examining the volumetric power generation of varying particle diameter samples. As particle diameter decreases the volumetric power generation of the material decreases. This would be expected if the material was heating via an eddy current loss mechanism, as the equation in Chapter 2 suggests, but if heating is via hysteresis loss, as is suspected for these particles, the effect of particle size is not as clear. There is a particularly sharp drop in volumetric power

generation between 15.4 and 6.71 micron particle diameter. This can be seen in the figure below for both 422 A/m and 545 A/m field strength.

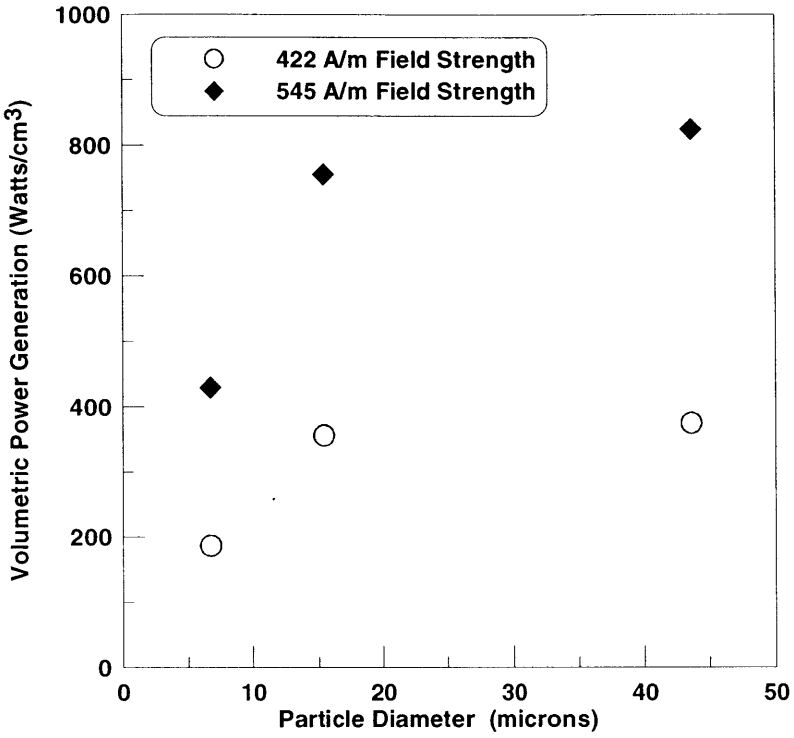

Figure 16: Particle Diameter vs. Volumetric Power Generation for 10% volume content C2050 exposed to a 12.2 MHz, 422 A/m, and 545 A/m magnetic field.

It is hypothesized that the relatively rapid drop in volumetric power generation of the magnetic particles seen between 15.4 and 6.71 microns is the result of a change in the hysteresis loss mechanisms occurring in the material. As discussed in Chapter 2 a ferromagnetic material experiencing hysteresis loss can undergo different loss mechanisms depending on the domain structure of the material. As particles get smaller, entering the sub domain particle size, loss mechanisms can change dramatically, from domain wall motion to domain rotation. This may be what occurs in this case. A particle size of 6.71μm may be entering the sub-domain size, and if this is the case, single domain particles require much larger coercive field strengths than multi-domain particles (Bozorth and Metals 1959). A material that has a higher coercivity will be more difficult

to get to switch magnetic orientation. If the magnetic field strength is not strong enough to overcome this increase in material coercive force, the material may not dissipate as much energy as a sub-domain particle as it does as a multi-domain particle. This could explain the observed drop in volumetric power generation for the smaller particles. Another possibility is that the ball milling process induced stresses in the material, changing the magnetostrictive energy of the material and thus affecting the material's domain structure, which would change the hysteresis loop of the material and this could have dramatically lowered the material's volumetric power generation compared to the non-ball milled samples. It is beyond the scope of this thesis to determine which of these mechanisms is responsible for the observed drop in volumetric power generation or if it is some other mechanism that is responsible. This is a topic for further investigation by someone who has a solid background in magnetism.

4.3.5 Material

Comparing the three different ferrites tested, C2050 had the highest value of volumetric power generation and was most efficient at heating, suggesting that it had the largest hysteresis loop of all the materials at the tested field strength and frequency. Cmd5005 had the next highest volumetric power generation and N40 had the lowest volumetric power generation of the materials. A rough way of estimating the relative size of a material's hysteresis loop, and so its potential for volumetric power generation is to multiply a material's remnance and coercivity together. This number gives a rough size of the material's full hysteresis loop and so the material with the larger number should generate more heat via hysteresis heating as long as the material is forced to magnetic saturation. According to this rough test C2050 was expected to have the highest

volumetric power generation, but N40 should have been second and cmd5005 third; instead cmd5005 was second and N40 third. The coercivity, remnance, and volumetric power generation of the materials tested are presented in the table below.

Material	Coercivity, B_c (Oersted)	Remnance, B_r (Gauss)	CxR	Power Generation 422 (A/m)	Power Generation 545 (A/m)
C2050	3.0	2400	7200	375	825
cmd5005	0.23	1800	414	311	529
N40	7.5	700	5250	292	521

Table 9: Coercivity, remnance, and volumetric power generation for 43.6μm particle diameter and 10% volume content in SMP for C2050, cmd5005, and N40 .

The relatively high coercivity of N40, 7.0 Oersted compared to 0.23 Oersted and 3.0 Oersted for the other materials, may have been the cause of its lower than expected volume power generation. This high coercivity suggests that N40 has a higher saturation magnetization value than cmd5005 and C2050. While cmd5005 and C2050 will reach their full hysteresis loop at lower field strengths, N40 will be experiencing minor hysteresis loops at these lower field strengths, and therefore may not generate as much heat as C2050 and cmd5005. If a strong enough field strength is used, one that could overcome the 7.0 Oersted coercivity of N40 and force this material to experience its full hysteresis loop, then N40 should have a higher volumetric power generation than cmd5005. From just the two field strengths tested it can be seen that the difference between the volumetric power generation of N40 and cmd5005 is diminishes as the field strength increases; for the 422 A/m applied field the difference is 19 W/cm^3 and for the 545 A/m applied field this difference drops to 9 W/cm^3. This trend supports the hypothesis that N40's high coercivity prevented it from exhibiting its full power generation capabilities. If the field strength was increased further the volumetric power generation of the N40 material should pass that of cmd5005. However, since the field

strength in these experiments was limited, cmd5005 exhibited a higher volumetric power generation then N40.

This result illustrates that the selection of a material for this application should not be based solely on which material has the largest full hysteresis loop but rather which material will have the larger hysteresis loop at the magnetic field strengths and frequencies used. The limitation on the field strengths and frequencies that can be used in a medical setting will dictate the magnetic properties, such as coercivity and remnance, which will maximize the volumetric power generation of a magnetic material.

It is also worth pointing out how much greater the volumetric power generation of the magnetic material is than the plain SMP. The magnetic material dissipated heat at a rate two orders of magnitude greater than just the plain SMP, 6.8 W/cm^3 compared to 600-1000 W/cm^3.

4.4 Heating of Complex Shapes

As mentioned earlier in this thesis, one of the potential advantages of this inductive heating approach is the ability to heat and actuate complex shaped devices. Some preliminary testing was done to demonstrate the heating and actuation of complex shaped devices. Shapes which would be otherwise impossible or extremely difficult to heat or actuate in situ in the body using laser or electro-resistive heating techniques were tested. These tests were very basic and employed an infra-red thermal imaging camera to measure the temperature of the device while suspended in room temperature air and being exposed to an alternating magnetic field. Three shapes were tested: a foam, a collapsed flower, and a flat flower.

The flower shape is a potential component of the clot extraction device discussed in Chapter 1 and is pictured in the figure below. This device was molded in a flat shape and then formed into the conical shape pictured. The initial flat shape was also experimented with as it was easier to see the spokes of the device in this configuration. The conical shape, as pictured below, is the actuated shape of the device. It is meant to take this shape when performing clot extraction. The device is delivered via a catheter by collapsing and compacting it further. The flower petal spoke pattern eliminates excess material which would interfere with this further collapsing and compaction. When in its fully collapsed position the device will be cylindrical in shape. Upon delivery to the site of interest the device is heated to recover the conical shape pictured below. This process is also illustrated in Chapter 1.

Figure 17: Flower shape tested in infrared thermal imaging heating experiment.

A sample of this flower was molded from SMP with a 10% by volume content of 43.6μm diameter particle C2050 magnetic material dispersed within it. Actuation was achieved in under 30 seconds, elevating the temperature of the device from 23˚C to 64˚C using a 12.2 MHz 400 A/m magnetic field. This actuating process is depicted in the figure below. The same coil which was used for the calorimetry experiments was also used in these tests. The outline of this coil can be seen in this image, as it is being slightly heated from the sample radiating heat. Temperature can be deduced from the color scale, white being over 86.7˚C and black being under 30.7˚C, and also the reading of the temperature at the cross is displayed next to the T, for example it is 35.5˚C for the first frame in the series.

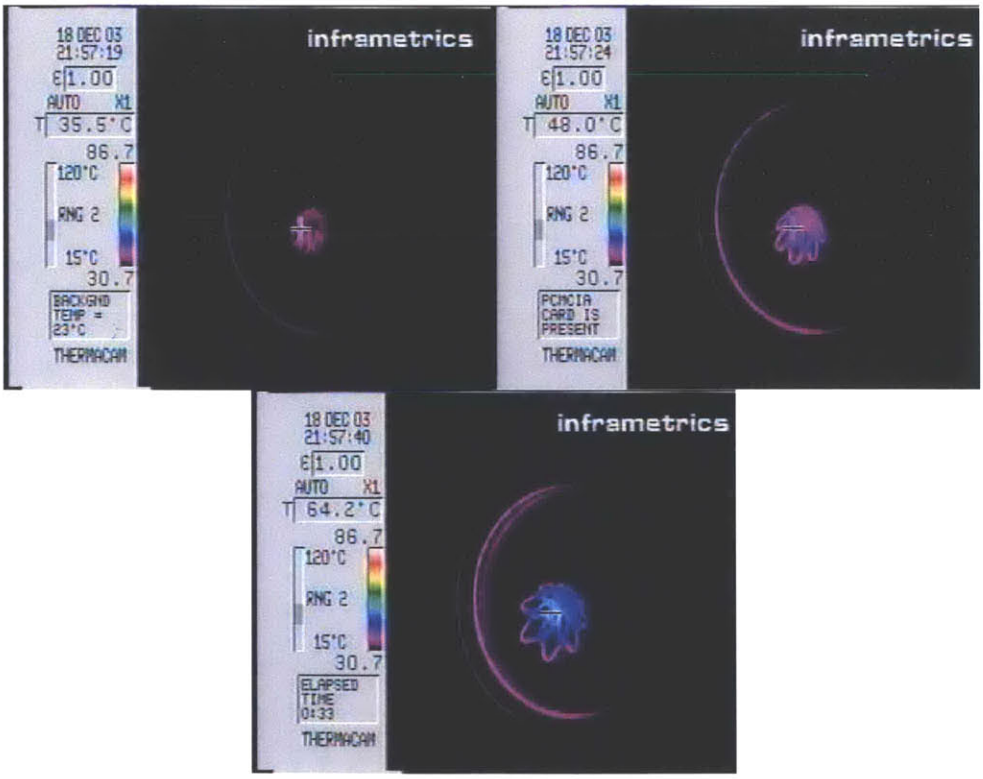

Figure 18: Actuation of SMP flower shape device with 10% volume fraction of 43.6μm particle diameter C2050 magnetic material. 12.2 MHz at 400 A/m applied magnetic field.

The initial flat version of this flower device was also heated. The images taken of this heating are shown in the figure below. The ring around the device is the flash from the molding process; it was left on to give the sample more rigidity for easier handling. While this sample does not demonstrate any actuation it does show an even and consistent heating pattern over most of the sample. The areas that are heating at a more rapid rate are at the outer ring and this is the material that is directly next to the coil where the magnetic field is strongest. The portion of the material that is farther from the coil does show very even and consistent heating. This tells us two things: one, the particles are providing even and consistent heating, and two, the magnetic field is fairly uniform inside the coil as long as you are slightly away from the coils edge, which the samples in the calorimetry tests were. The same settings were used as above and the sample had the same particle material and loading. The sample was heated from 29˚C to roughly 40˚C in 5 seconds with the portion of the sample closest to the coil being heated to 59.1˚C in this same amount of time.

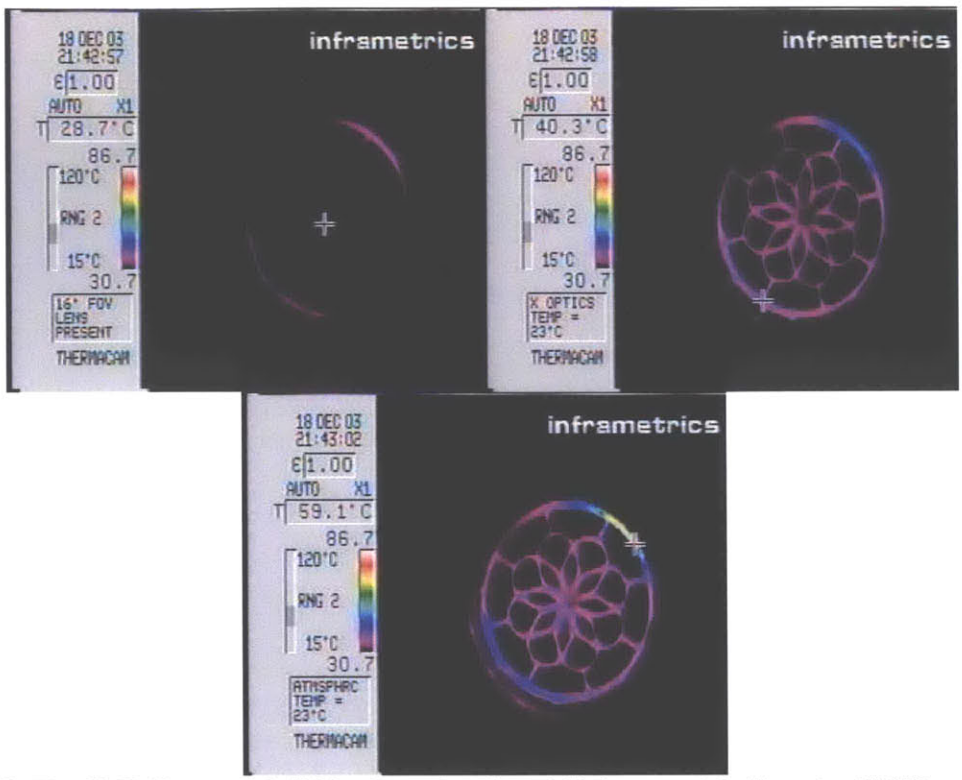

Figure 19: Flat SMP flower with 10% volume fraction of 43.6μm particle diameter C2050 magnetic material. 12.2 MHz at 400 A/m applied magnetic field.

The final device geometry tested was a foam. There is some interest in using SMP foams as a packing material to fill aneurysms. The figure below shows an example of an SMP foam in a collapsed state and in an actuated, expanded shape.

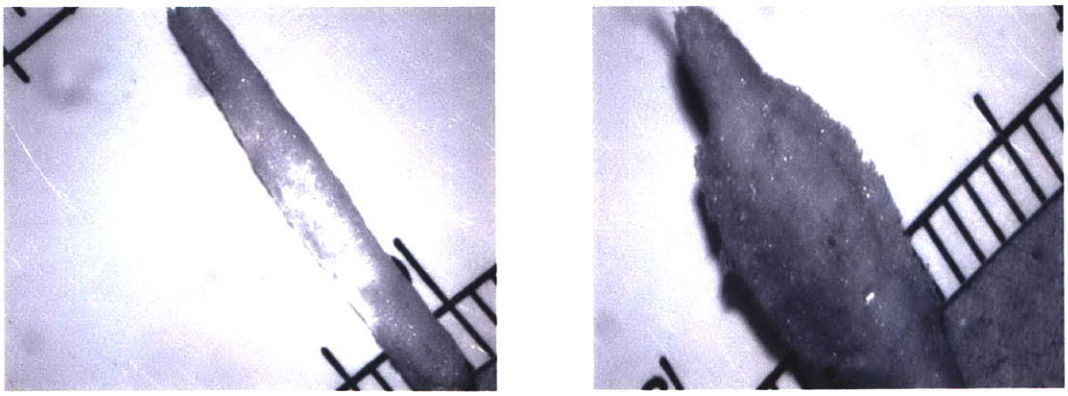

Figure 20: SMP foam in a collapsed and an actuated configuration.

A foam with the same volume content, particle size, and material as those samples previously described was heated in the same field. The foam heated from room temperature to over 78.6˚C in less then 15 seconds. The sample appeared to about double in size upon the heating and subsequent actuation of the SMP.

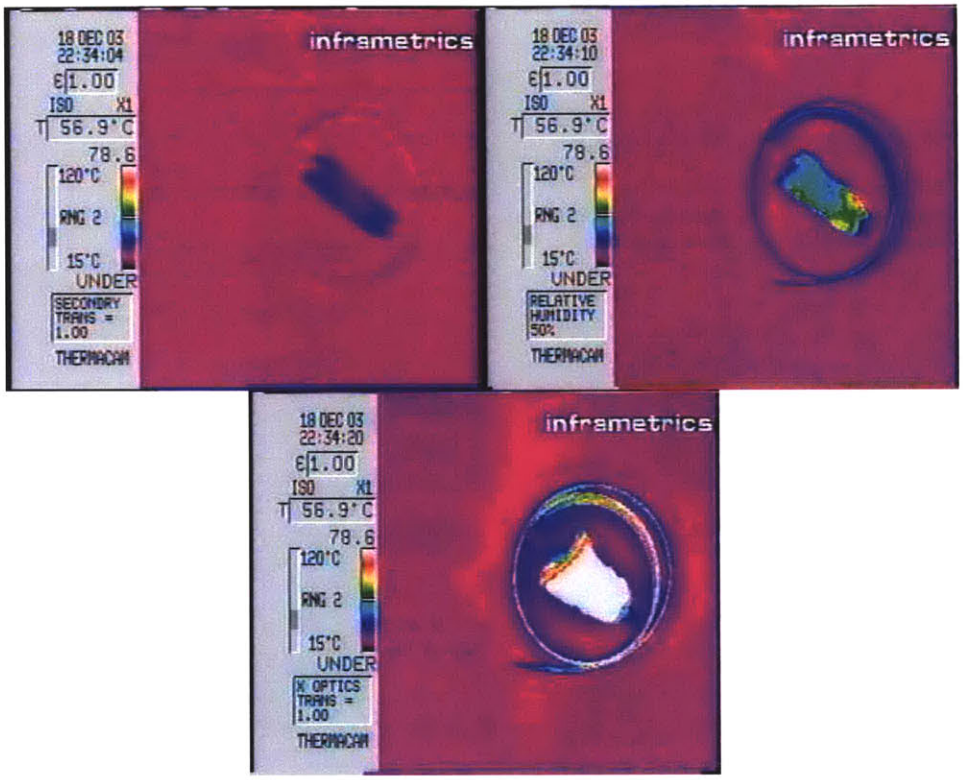

Figure 21: SMP foam with 10% volume fraction of 43.6μm particle diameter C2050 magnetic material. 12.2 MHz at 400 A/m applied magnetic field.

The initial success of these heating experiments is very promising. None of the devices tested had any sort of optimization of magnetic heating particle material. It is believed that with processing improvements in the preparation of the SMP and an optimization of particle volume content, even better shape recovery will be achieved. For example, the foam tested was a first generation process. With improvements in the

production and compression techniques, actuated shape changes on the order of 4 to 5 times the un-actuated sample shape should be possible.

5 Mechanical Testing

The effect that dispersed particles have on the mechanical properties of the SMP is a key concern for this new heating approach. If the addition of particles to the SMP causes it to lose its desired mechanical properties, then this is a great disadvantage for this heating approach. Characterizing any potential change in the shape memory characteristics of the material, including shifts in glass transition temperature, glassy modulus, and rubbery modulus, was seen as important in determining the feasibility of this inductive heating approach. To assess these changes, three different tests were performed, Dynamic Mechanical Thermal Analysis (DMTA), Differential Scanning Calorimetry (DSC), and a strain recovery test performed at 80°C. The result of these tests, as well as a brief description of how these tests were performed, follows.

5.1 Dynamic Mechanical Thermal Analysis

5.1.1 Test Procedure

The DMTA test procedure that follows was prepared by Dr. Tom Wilson and tests were performed by him at the Lawrence Livermore National Laboratory. Measurements were made using a TA ARES-LS2 model rheometer, pictured in figure 22 below. The control software was TA Orchestrator, and the test atmosphere was dry air with heating performed by forced convection. DMTA measurements were made on several thermosetting SMP resins using the following procedure. Samples were first prepared by polymerizing in 1 ml syringes (polypropylene) at manufacturer recommended conditions unless otherwise specified.

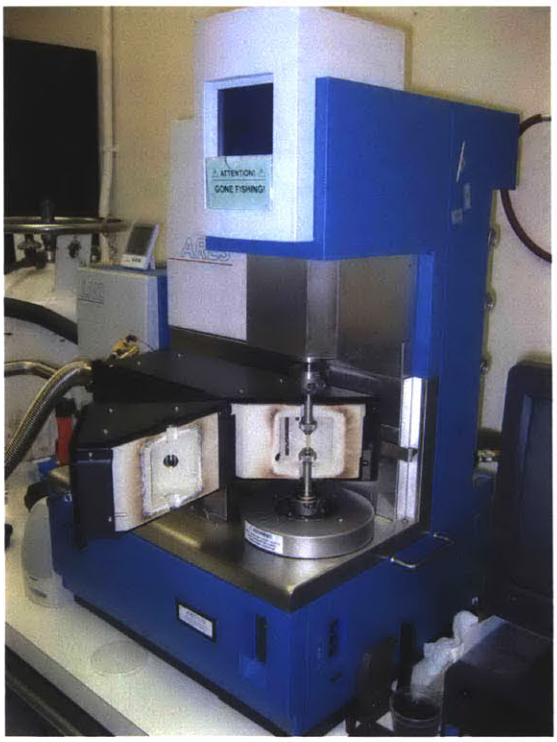

Figure 22: TA ARES- LS2 rheometer, with sample loaded for testing.

Resulting samples were typically 4.65 mm in diameter and up to 70 mm in length. The ARES instrument was set up with a torsion rectangle test fixture and the test geometry typically used was at the molded diameter and with a 25 mm gap between upper and lower fixtures.

Prior to running dynamic temperature ramp tests, dynamic strain sweeps were run on neat SMP samples at a frequency of 6.28 radians/second, and it was determined that a strain of 0.01% was below the linear visco-elastic limit but provided an adequate torque response. DMTA tests were then run on samples using the torsion rectangle geometry and a frequency of 6.28 radians/second (1 Hz). Tests were started at 25°C at a strain of 0.01%, and the temperature was ramped up at a rate of 1°C/minute to 120°C, with data being collected every 15 seconds. The autostrain feature of the Orchestrator software was used to both apply a small tensile force to the test specimen (0 to 10 grams) when the

shear storage modulus was above 5e6 Pa, and to adjust the applied shear strain on the sample to keep the torque above a minimum of 2 gram-centimeters. While the strain reached as high as 5% (set limit) during the experimental procedure, the sample remained in the linear visco-elastic regime as indicated by strain sweep testing at the end of the test for the 'rubbery' sample. The rheological quantities of dynamic shear storage modulus G', dynamic shear loss modulus G", and their ratio tan δ were calculated by the Orchestrator software from the raw torque and angular displacement data using standard formulae (Macosko 1994).

5.1.2 Test Results

The soft phase glass transition temperature, T_g, of SMP is the temperature at which the material actuates and regains its remembered shape. This is an important aspect of any potential device designed from this material. For this reason it is important to understand any changes that occur in the material due to the addition of magnetic heating particles. T_g has been previously calculated as either the temperature at which the loss modulus, G'' peaks (Metzger Maitland 2002), or as the temperature at which the loss tangent, tan (Delta) peaks (Kim 1996). The physics of the processes that become active at the glass transition temperature can be qualitatively described as the onset of long-range, coordinated molecular motion in the polymer (Sperling 1986). The maximum in loss modulus and loss tangent signal different degrees of molecular motion in the polymer (Wilson 2004), with the maximum in the loss modulus signaling shorter range motion associated with the onset of the glass transition region, and the maximum of the loss tangent signaling longer range, rapid coordinated molecular motion associated with approaching the end of the glass transition region and the beginning of the rubbery

plateau region (Sperling 1986). As can be seen in the sample DMTA graph in the figure below, the maximum of G'' occurs at a temperature just to the left of the center of the glass transition region and the maximum of tan (Delta) occurs just to the right of center of the glass transition region. Because of this, it was seen as a reasonable approach to calculate T_g as the average of the temperature at the peak loss modulus and the peak loss tangent.

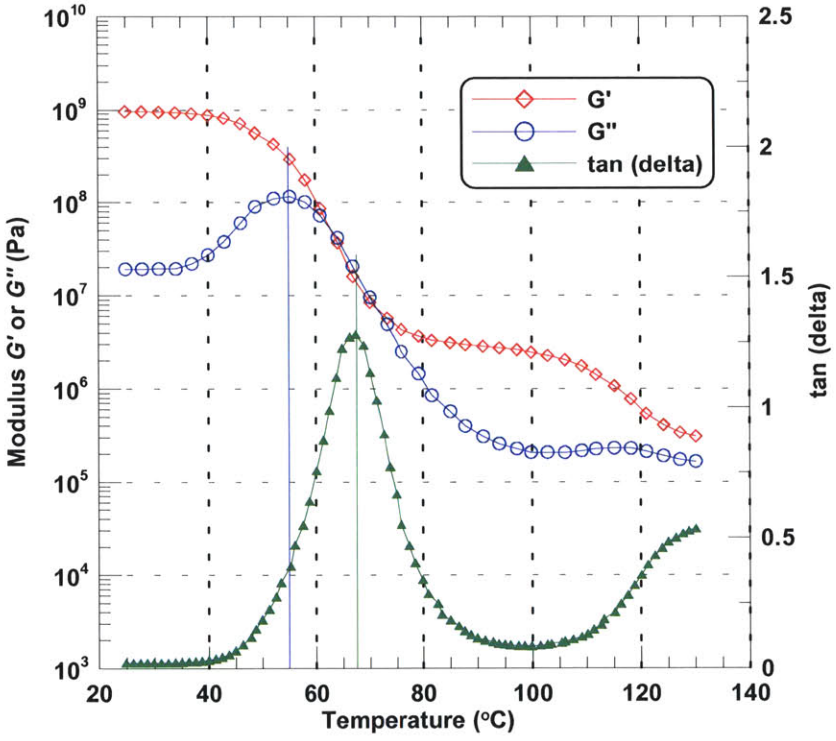

Figure 23:DMTA test results for 5% volume content, 43.6μm particle diameter C2050 loaded SMP illustrating G'' maximum and tan (delta) maximum to the left and right of glass transition region on dynamic storage modulus curve. Vertical lines indicate the T_g values found at the G'' and tan (delta) peak values.

This data is compiled from the DMTA graphs in Appendix B and displayed in the table below. The plain SMP samples are presented with the time that they were allowed to sit at a room temperature cure before being placed in the oven at 80˚C. For example ,0% SMP 0.5h 25C designates plain SMP with no magnetic particles, allowed to sit at room temperature, 25˚C, for a half an hour before being cured at 80˚C.

Volume (%), Particle Diameter (μm), Material	Temp. at G" max (˚C)	Temp. at Tan(delta) max (˚C)	T_g (˚C)
1%, 6.71μm, C2050	54.5	67.3	60.9
1%, 43.6μm, C2050	55.7	67.7	61.7
5%, 6.71μm, C2050	53.2	66.6	59.9
5%, 43.6μm, C2050	54.9	66.9	60.9
10%, 6.71μm, C2050	50.9	63.9	57.4
10%, 15.4μm, C2050	53.5	65.5	59.5
10%, 43.6μm, C2050	55.3	67.5	61.4
20%, 6.71μm, C2050	49.6	62.5	56.1
20%, 43.6μm, C2050	54.4	65.9	60.1
10%, 43.6μm, cmd5005	49.8	63.5	56.7
10%, 43.6μm, N40	49.9	63.0	56.4
0%, SMP 0h 25C	50.6	61.9	56.3
0%, SMP 0.5h 25C	45.5	56.9	51.2
0%, SMP 1h 25C	49.2	62.4	55.8
0%, SMP 2h 25C	48.9	62.1	55.5

Table 10: DMTA results for the shift of T_g in SMP for varying particle volume fractions, particle size and particle material.

The T_g of SMP appears to be effected by the addition of varying particle sizes and particle volume contents in a peculiar way. There is an initial jump in T_g with the addition of any particles into the material, but after this jump at 1% volume fraction, the effect of additional particles, even up to volume fractions of 20%, seems to be negligible for 43.6 micron size particles and actually drops for 6.71 micron size particles. These trends are illustrated in the figure below. The glass transition temperature never varies by much more than 6˚C due to the addition of particles. When this 6˚C difference is compared to the 5˚C difference observed between the plain SMP samples with varying 25˚C cure times, it seems that the effect of particles on T_g is minimal.

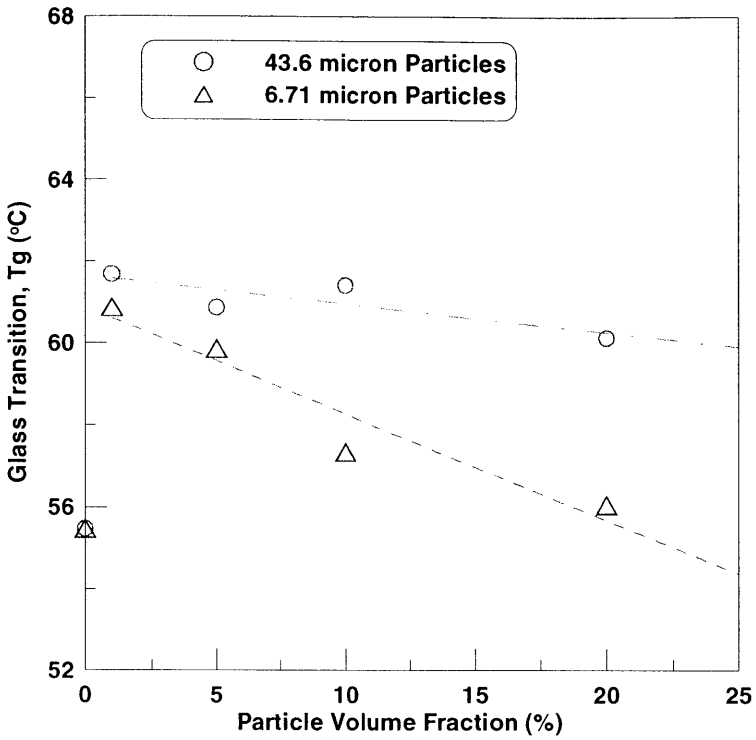

Figure 24: Glass transition temperature vs. particle volume content, illustrating the effect of particle volume fraction and particle size on the T_g of SMP.

Other useful information that can be gleaned from the DMTA test data are the glassy modulus, often used for assessing shape memory behavior and defined as the modulus at a temperature of T_g -20°C, and the rubbery modulus, again often used for assessing shape memory behavior and defined as the modulus at a temperature of T_g+20°C. These two pieces of information are potentially useful for the design of medical devices, giving some information about the rigidity and compliance of the material above and below its actuation temperature.

The ratio of glassy modulus over rubbery modulus, known as the storage modulus ratio, is a measure of the size and breadth of the glass transition (Maitland et al. 2002). This measure is an indication of the strength of the shape recovery effect and has been previously reported for other shape memory polymers (Kim et al. 1996). This information is compiled from the graphs in Appendix B and displayed in the table below.

Volume (%), Particle Diameter (μm), Material	Glassy Modulus (MPa)	Rubbery Modulus (MPa)	Storage Modulus Ratio
1%, 6.71μm, C2050	742	3.02	245
1%, 43.6μm, C2050	734	2.68	273
5%, 6.71μm, C2050	878	4.37	200
5%, 43.6μm, C2050	856	3.45	248
10%, 6.71μm, C2050	1030	5.44	189
10%, 15.4μm, C2050	1060	7.03	150
10%, 43.6μm, C2050	1010	4.85	208
20%, 6.71μm, C2050	1440	16.8	85
20%, 43.6μm, C2050	1620	13.9	116
10%, 43.6μm, cmd5005	1130	6.53	173
10%, 43.6μm, N40	1180	9.64	122
0%, SMP 0h 25C	757	1.72	440
0%, SMP .5h 25C	786	9.32	84
0%, SMP 1h 25C	753	4.18	180
0%, SMP 2h 25C	646	3.9	165

Table 11: DMTA results, Glassy Modulus, Rubbery Modulus, and Storage Modulus Ratio.

The effect of a particulate filler on a continuous polymer matrix has been studied in great detail and there exists a number of models to predict the effect that increasing volume fractions of particle material has on the modulus of a polymer/particle composite system (Bliznakov et al. 2000). One well known model is the Guth and Smallwood equation, which is the following (Bliznakov et al. 2000):

$$G = G_m(1 + 2.5\phi + 14.1\phi^2) \qquad \textbf{(13)}$$

where G is the predicted modulus of the polymer/particle composite, G_m is the plain polymer matrix modulus, and ϕ is the volume fraction of particles. Comparisons between the data collected, presented in the table above, and the predictions of the Guth-Smallwood model will be used to show how closely the SMP particle composite matches theoretical predictions. For reasons that will become clear later the data was fit around the 1% volume fraction data point instead of the plain SMP modulus data point which was recorded. That is to say that G_m was calculated by using the measured value of G at

1% volume content (actually the averaged value of the 6.71μm and 43.6μm particle diameter 1% volume content modulus measurements).

As can be seen below, in figure 25, the rubbery modulus increases with the volume content of particles but at a much more rapid pace then what is expected from the Guth-Smallwood model. There is also a large jump in the value of the modulus at a 20% volume fraction of particles.

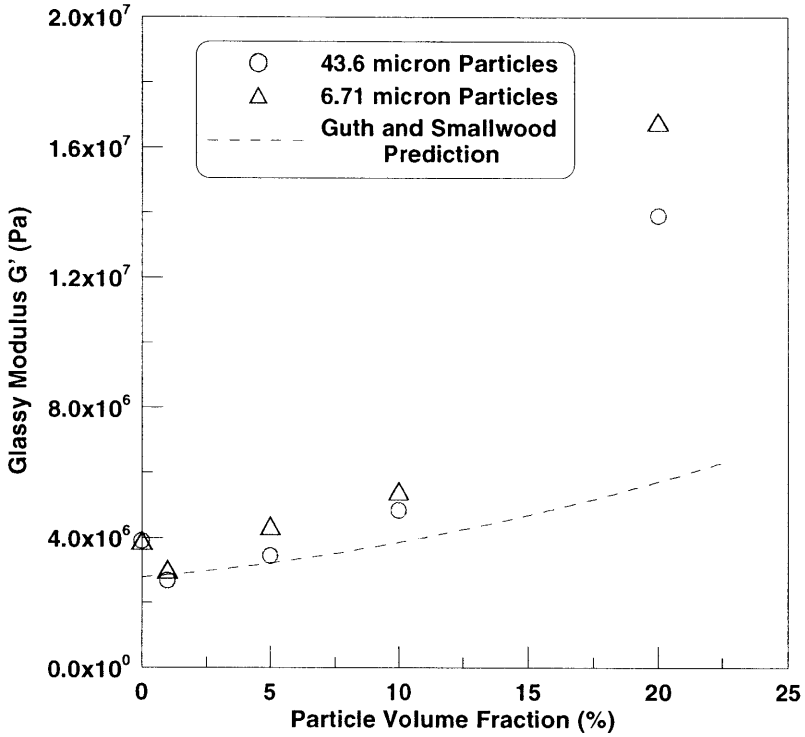

Figure 25: Rubbery dynamic storage modulus vs. particle volume fraction, illustrating increasing SMP rigidity in the rubbery region with increasing volume fraction of particles.

The plain SMP sample used in this graph is the 2 hour, 25°C cure. It is not clear if the initial drop in modulus between the plain SMP and the 1% volume content sample is a repeatable effect. There appears to be quite a bit of variation in the properties of the plain SMP depending on the amount of time the material is allowed to cure at 25°C before being cured at 80 °C. This is the main reason the plain SMP data point was not used to determine G_m in the Guth-Smallwood model. The rubbery region of the material

appears to be especially sensitive to this cure time (or at least more so than the glassy region) as can be seen in the figure below. The rubbery modulus varies by as much as 82%, 1.72 MPa to 9.32 MPa, while the glassy modulus only varies by 18% between 646MPa and 786MPa.

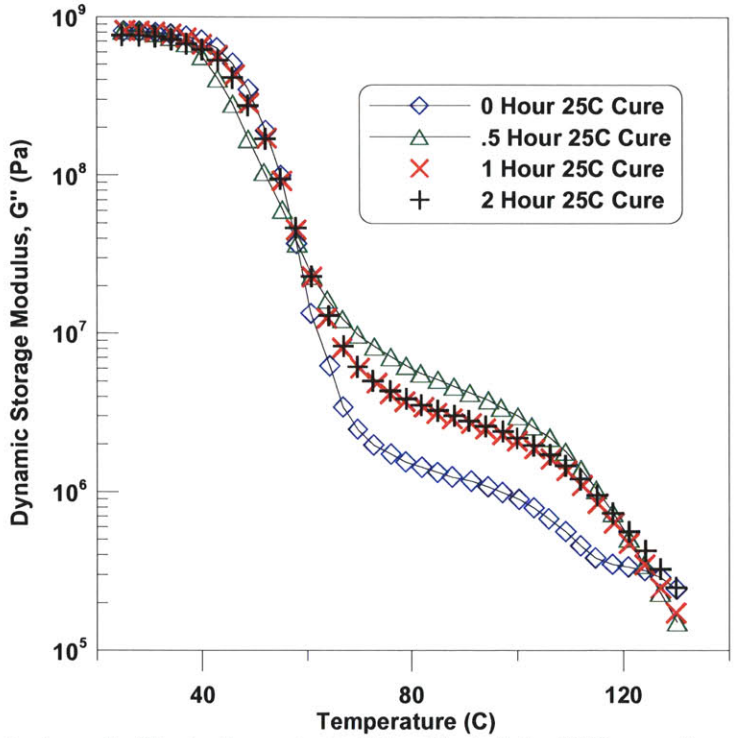

Figure 26: DMTA test results illustrating extent of the effect of the 25˚C cure time on the mechanical properties of SMP.

It also appears that it is in the first hour of the room temperature cure that the material changes its properties the most. After a one hour cure, it appears that whatever reactions are occurring in the material and causing this change in material properties are completed. As can be seen in the figure above, the one hour and two hour curves lay almost directly on top of each other. Another interesting trend in this data is that during the first hour of a 25˚C cure, the mechanical properties of the material appear to fluctuate before reaching the final steady one hour and two hour cure values. For example, the rubbery modulus is a low 1.72 MPa if there is no room temperature cure. This value

jumps to 9.32 MPa if the material is allowed to cure at room temperature for a half an hour, and then this comes back down to a value of approximately 4.0 MPa for materials allowed to cure at room temperature for one hour or two. This same fluctuation can be seen in the values of T_g, reported in table 10, where for a material with no room temperature cure, the glass transition temperature is 56.3°C, dropping to 51.2°C for a half an hour room temperature cure, and then rebounding to a value of roughly 55.5°C for materials allowed to cure for one or two hours. This overshoot phenomenon may be the result of competing processes occuring in the material during the initial room temperature cure (Mckinley 2004).

SMP by its nature is a two phase system, with hard and soft phases. A comparison can be drawn with tapioca pudding; the pudding being the soft phase of the material and the tapioca beads being the hard phase of the material. The initial room temperature cure has a profound effect on the degree of phase separation and the size of microphase domains (tapioca beads) in the material (Wilson 2004). Some of the processes which are believed to be occurring during this cure are diffusive mixing of parts A and B, condensation polymerization, side reactions, and phase separation. The potential impact of each one of these processes will be briefly discussed.

Diffusive mixing occurs at a slower rate than the initial mechanical mixing the material is subjected to. As the material is allowed to sit at room temperature for longer periods of time the two parts may become more thoroughly mixed via this diffusive mechanism. This mixing would affect the rate that chemical reactions occur in the material.

Condensation polymerization may occur during a room temperature cure in the form of hydroxyl groups reacting with isocyanate, to form urethane linkages (Wilson 2004). However, if the A and B components are mixed in an ideal ratio, there should be no crosslinking, as both components are di-functional (Wilson 2004). The rate of this condensation polymerization could have an effect on the mechanical properties of the material

Side reactions may occur during a room temperature cure in the form of isocynate abstracting the hydrogen on the urethane nitrogen leading to a nitrogen-carbon bond and an allophanate group (Wilson 2004). This allophanate group is a cross link site, but without knowing the thermodynamics of the phase separation of the A and B rich materials into soft and hard phases it is unclear how this allophanate cross linking would effect the material's modulus (Wilson 2004). If there was no phase separation this crosslinking would increase the material's modulus, but if this cross linking inhibits the separation of the soft and hard phases in the material it could decrease modulus (Wilson 2004). This side reaction should be reversible above 70°C and so can be discounted as having an effect during the 80°C cure (Wilson 2004).

Phase separation between of the urethane rich phase and the oligo-ester rich phase may be occurring during the room temperature cure and effecting the mechanical properties of the SMP (Wilson 2004). The phase diagram for this two part system is not known but it is suspected that there is an upper critical solution temperature (Wilson 2004).

During the first hour of a room temperature cure these competing processes may be causing this fluctuation in properties. After an hour at room temperature these

processes may be finished or may become insignificant in changing the properties of the SMP. It is beyond the scope of this thesis to investigate this effect but it may be a topic for future research.

When this room temperature cure time effect was noticed, the sample preparation protocol was adjusted so that all samples sat at room temperature for at least one hour before being cured at an elevated temperature of 80 °C. It was believed that implementing this simple room temperature hold time would help ensure consistency in the properties of the SMP between samples. It would have been ideal to prepare all samples with exactly the same cure times but this was not possible due to the constraints of the molding process.

There appears to be a more predictable effect of increasing volume content of particles on the glassy modulus of the material, with increasing volume contents leading to an increase that is predicted by the Guth-Smallwood model. It also appears that just as with the rubbery modulus the particle size has little effect on the glassy modulus until a volume content of 20% is reached. These two effects are illustrated in figure 27 below.

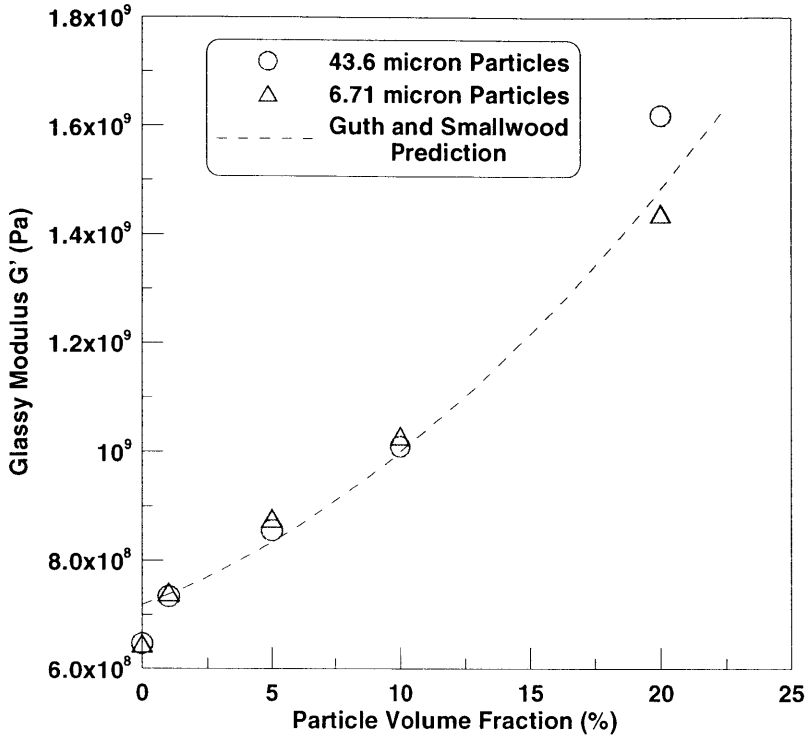

Figure 27: Glassy dynamic shear storage modulus vs. particle volume fraction, illustrating increasing SMP rigidity in the rubbery region with increasing volume fraction of particles.

The plain SMP sample used in this graph was cured at 25°C for 2 hours. The plain SMP sample point shown in figure 27 is believed to be more reliable then the rubbery modulus plain SMP data point because the 25°C cure time did not have as large an effect on the glassy modulus as it did on the rubbery modulus of the material, as discussed above (see figure 26). Comparing the effect of particles on the glassy and rubbery phase it is clear that particle volume content has a much greater impact on the rubbery modulus than on the glassy modulus. At a 20% volume content the rubbery modulus increased by roughly 394% while the glassy modulus increased by roughly 137% from the plain SMP modulus. While this large difference is not predicted by the Guth-Smallwood model it is not a counter intuitive result. The glassy modulus of the SMP is closer in value to the modulus of the particle material than is the rubbery modulus of the SMP and this may account for the greater effect of the particles on the rubbery modulus. Intuitively, one

would expect that the addition of hard particles to a soft material, the SMP in the rubbery phase, would cause it to stiffen by more than the addition of hard particles to a hard material, the SMP in the glassy phase.

One effect that is unexpected is the difference in the effect of particle size on modulus at 20% volume fraction for both the glassy modulus and rubbery modulus. In both cases the particle size appears to have a significant effect, causing the modulus to vary by more than 10% of the lower modulus value recorded (13% for the glassy modulus and 21% for the rubbery modulus), however, the effect is in the opposite direction. The smaller 6.71μm particles cause the rubbery modulus to be enhanced more while it is the larger 43.6μm particles that cause the glassy modulus to be higher. A cause of this may be the greater amount of particle surface area which exists for the smaller particles, as compared to the larger particles. This increased particle surface area would interfere more significantly with any type of semi crystalline structure of the SMP in the glassy phase, causing the material to lose some of its rigidity which is due to this crystalline order. The rubbery phase of the material does not rely on a crystalline structure for its rigidity and so the above mentioned effect would have no influence. The material in the rubbery phase undergoes greater molecular motion and it is plausible that the increased surface area offered by the smaller particles does more to retard this motion by coupling the relaxation of the polymer chains to surface interactions with the particles (Wilson 2004). It is beyond the scope of this thesis to explore this hypothesis further and the cause of this observed effect, however the structure-morphology interactions in shape memory polymers would be an interesting future project for material scientists and microscopists.

5.2 Strain Recovery

DMTA provides a great deal of information about a material under small strains. However, medical devices, such as stents or the clot extraction device described in Chapter 1, function at much larger strains than those seen in DMTA tests. The ability of SMP to undergo large strains is one of the reasons this material is such an attractive candidate for certain types of devices. Due to time limitations, only a limited number of strain tests were performed, investigating the effects that varying particle volume content had on the modulus and larger strain recovery at an elevated temperature of 80°C. Tests were performed as described below.

5.2.1 Test Procedure

Strain recovery tests were performed using a Synergy MTS Tensile machine with a 5 kN load cell. The samples were tested starting at a 25.0 mm gaped test jaw setting. The samples were roughly 10mm longer than this, allowing the sample to be held at both ends by clamping jaws. The sample was 12.5 mm in width, and 1mm in thickness. These samples were made using the mold and injection molding technique described in Chapter 3. Samples were loaded between testing jaws and then allowed to warm, from room temperature to 80 °C, for at least three minutes. During this period the sample would increase in length due to thermal expansion, putting a negative force on the load cell. This force would be zeroed out manually before the testing began. After the three minute temperature equilibration time the test would begin and the sample would be extended at a rate of 12.5mm/min in a nitrogen environment of 80°C. Once the sample reached 50% strain, the extension would stop and the sample would be held at this extension for 30

seconds. At the end of this 30 seconds the sample would be relaxed by allowing the testing jaws to compress at the same rate of 12.5 mm/min.

The following test setup made this testing possible. A cylindrical housing, made of poly(tetrafluoroethylene) was built around the testing jaws to act as an oven. A line of heated nitrogen gas was fed into the bottom of this housing and was allowed to escape from the top of the housing, which was intentionally left open. The temperature of the nitrogen air was monitored and controlled by a LOVE Control model 2600 control system which had an input from a thermocouple which was placed inside the housing, near the sample. This test set up is pictured in the figure below. The load cell was insulated from the flow of hot nitrogen, which was exiting the top of the housing, by a piece of foam. In addition to this, a flow of room temperature nitrogen was directed over the load cell to help cool it and ensure that it was minimally influenced by the hot air exiting the top of the chamber.

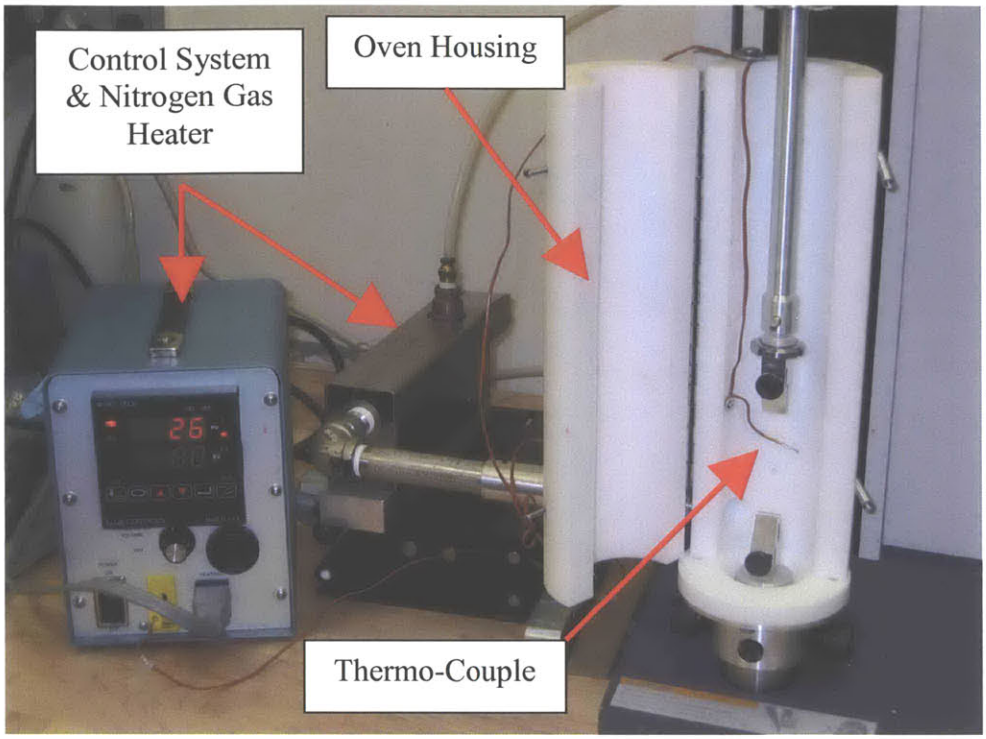

Figure 28: Tensile testing setup, LOVE Control model 2600, and thermo-couple.

5.2.2 Test Results

A representative sample of one of these strain recovery plots is depicted in the figure below. There is a consistent artifact in the sample data which occurs between 0.25 and 0.5 MPa where the value of stress jumps a small amount quite suddenly. This small 'blip' is believed to be the result of some sort of switching mechanism in the load cell. The loads measured during testing were never more than 40 N and the load cell was designed to measure up to 5000 N, so the tests were conducted at the lower limit of the capability of the load cell. This was not an ideal testing situation but it was the best available.

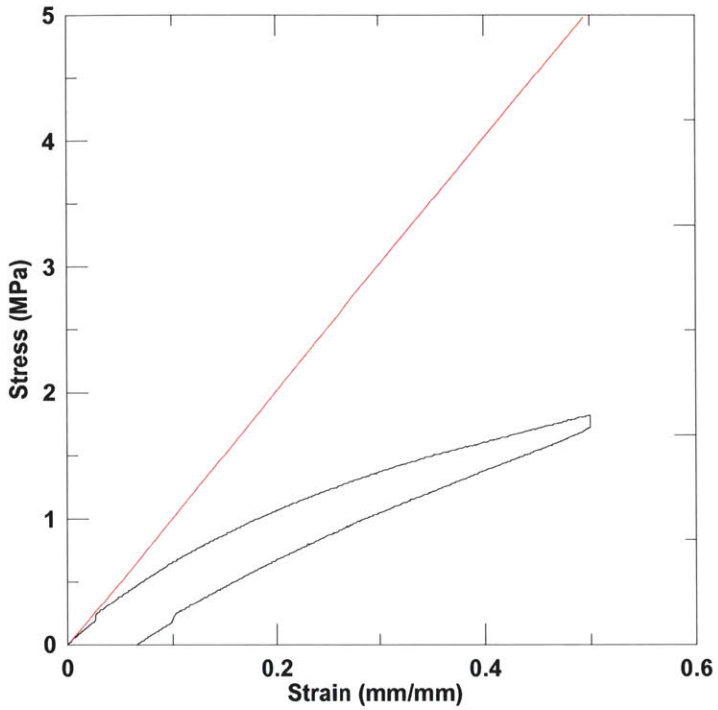

Figure 29: Stress vs. strain plot of tensile strain recovery test, 5% particle volume content, 43.6μm particle size, and C2050 particle material, red line represents slope that the Young's modulus was calculated from.

All strain recovery curves can be found in Appendix D. The key results were tabulated from these graphs and are presented in the table below. The Young's Modulus was calculated using data points between 0.1% and 0.4% strain. This provided a minimum of 4 data points in each test to fit a line which was seen as the minimum which should be used. It is important to point out that the plain SMP samples used in this test were not from the same prepared batch of SMP samples used in the DMTA tests. This is important, because each time a sample was prepared, there was a slight difference in the ratio of part A and part B of the thermoset. Usually this measurement was accurate to within +/- 0.1 grams of either part; of the either 7.5 g or 15 g mixing batches that were typically used in this thesis. It is unknown how these small variations between sample batches affect the properties of the SMP however it is prudent to point out when samples with nominally identical compositions and preparation protocols are mixed and prepared

in different batches. The particle loaded samples used in the tensile strain recovery tests were from the same batch of prepared samples as those tested in the DMTA tests.

Volume %, Particle Diameter, Material	E, Young's Modulus @80°C (MPa)	Hysteresis Area (MPa)	Max Stress (MPa)	Recovered Strain (%)
0%, SMP 2h 25C	7.00	0.144	1.35	85.6
1%, 43.6µm, C2050	8.09	0.115	1.58	88.4
5%, 43.6µm, C2050	10.1	0.156	1.82	86.7
10%, 43.6µm, C2050	12.4	0.322	2.54	80.4
0%, SMP 0h 25C	15.5	0.246	1.86	84.7

Table 12: Strain recovery test results, Young's Modulus, Hysteresis Area, Max stress, Recovered strain

The trends in this data, with respect to modulus and particle volume content, are very similar to those in the DMTA test data. This is an expected result. As particle volume content is increased the Young's modulus and dynamic shear storage modulus both increase. This is shown in the figure below. The plain SMP samples are shown as a reference, but as mentioned above they were not from the same sample batch, and for this reason the DMTA storage modulus and Young's modulus obtained from tensile testing should not be quantitatively compared.

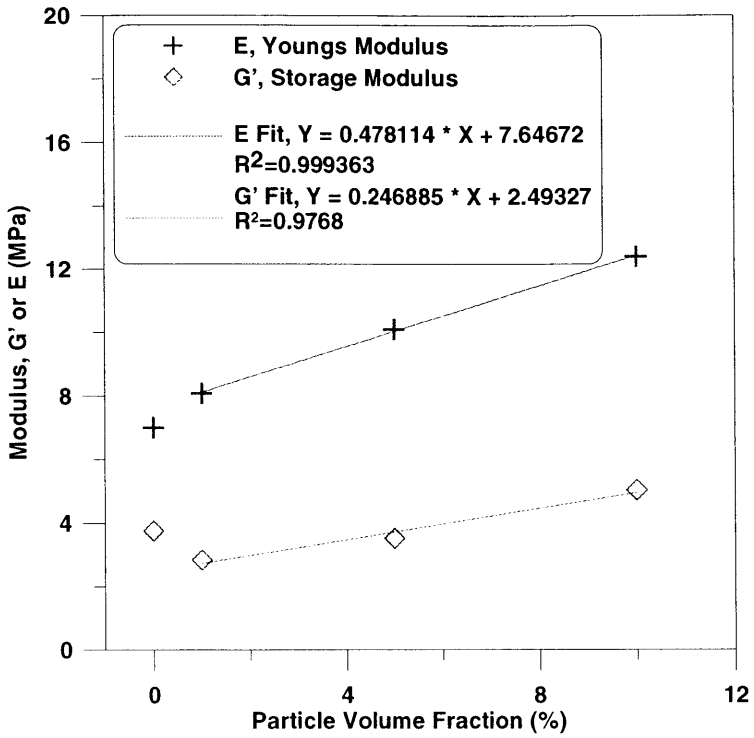

Figure 30: DMTA dynamic shear storage modulus, G', compared with tensile test Young's modulus, E, for increasing volume content of particles. Magnetic material C2050 with 43.6μm diameter dispersed particles.

The recoverable strain appears to increase at first with the addition of 1% by volume of particles and then decreases slightly with increasing volume content of particles, up to at least a 10% volume content. This change in recovered strain is never more then + or – 5% of the plain SMP material. Magnetic particle loaded SMP appears to have roughly the same strain recovery capabilities as plain SMP, at least up to 10% volume content.

The area of the hysteresis loop traced during the strain recovery test is a measure of how much energy is irreversibly lost during strain recovery. One would expect that this mechanical hysteresis loss would be greater, that is the area of the hysteresis loop would be greater, for materials that have lower values of strain recovery. This is because energy that is not stored elastically in the material and used to recover the material's original shape is dissipated viscously as heat. This is exactly what is seen in the data from the

tensile tests. The sample with the most recovered strain, 1% particle volume content SMP with 88.4% recovered strain, has the lowest hysteresis loss, 0.115 MPa, and the samples with the least recovered strain, 10% particle volume content with 80.4%, has the highest hysteresis loss, 0.322 MPa.

5.3 Differential Scanning Calorimetry

5.3.1 Test Procedure

The DSC test procedure that follows was prepared by Dr. Tom Wilson and tests were performed by him at the Lawrence Livermore National Laboratory. DSC tests were run using a Perkin Elmer Diamond DSC equipped with an intracooler 2. Samples with a mass of approximately 5 mg were cut from test rods as polymerized and placed in standard, closed aluminum pans. The instrument was previously calibrated against an Indium standard. Tests were run in multi-ramp sequences in which the sample was first cooled to -20°C, next ramped up to 200°C at 20°C/minute, ramped down again to -20°C at 20°C/minute, and then ramped up again to 200°C at 20°C/minute. The resulting heat flow is adjusted using an empty aluminum pan as the baseline. Glass transitions were calculated from the heat flow data using the instrument Pyris® (Meesiri et al. 1982) software (Pyris Data Analysis Module, ver. 5.00.02, Perkin Elmer Instruments LLC.), based on the temperature at which one half the change in the heat capacity has occurred due to the transition (Meesiri et al. 1982) using the method of temperature at half the glass transition, temperatures of the soft and hard phase transition of each material were calculated from the data at the half height of the heat capacity transition.

5.3.2 Test Results

The results of a DSC test are shown in the figure below. The arrows indicate the direction the test was conducted in, increasing temperature for arrows pointing to the right and decreasing temperature for arrows pointing to the left. The entire set of test curves can be seen in Appendix C. The glass transition of the two heating sequences and one cooling sequence were calculated using the method described above.

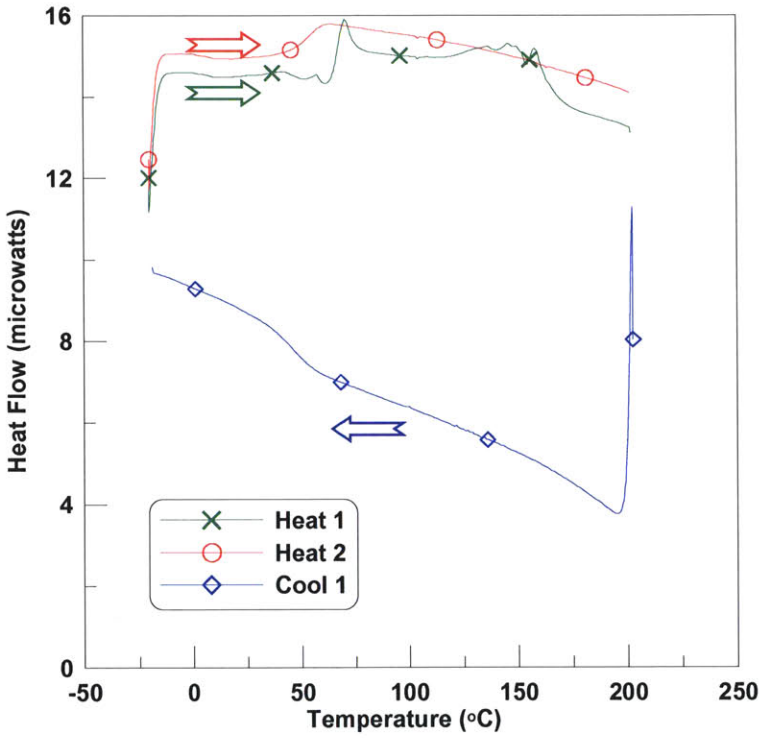

Figure 31: DSC test curve for 1% volume content C2050 SMP, 6.71μm particle diameter.

The glass transition was calculated for all graphs found in Appendix C and this data is presented in the table below. The variation in the calculated T_g between the different heating and cooling sequences is common for these types of tests and is the result of two things. Firstly, the changing thermal history of the material as the test is being run, and secondly the reality of T_g being more a representation of a temperature range over which the glass transition occurs, rather than just one particular value of

temperature (Cassel 2004). During the first heating cycle any residual morphology resulting from sample preparation is eradicated and so for the sake of comparing DMTA and DSC results, the T_g calculated from the 2nd heating sequence will be used.

Volume %, Particle Size, Material	T_g 1st Heat (°C)	T_g 1st Cool (°C)	T_g 2nd Heat (°C)
1%, 6.71μm, C2050	66.2	46.0	53.2
1%, 43.6μm, C2050	63.1	44.4	53.6
5%, 6.71μm, C2050	61.8	43.1	53.2
5%, 43.6μm, C2050	61.0	42.8	52.1
10%, 6.71μm, C2050	52.7	46.0	55.4
10%, 15.4μm, C2050	59.5	47.2	55.4
10%, 43.6μm, C2050	61.3	44.0	50.2
20%, 6.71μm, C2050	44.6	44.7	55.0
20%, 43.6μm, C2050	54.4	47.9	53.5
10%, 43.6μm, cmd5005	50.1	45.2	49.3
10%, 43.6μm, N40	50.1	50.4	56.8
0%, SMP 0h 25C	54.7	40.6	47.1
0%, SMP .5h 25C	47.7	41.1	45.4
0%, SMP 1h 25C	55.4	41.3	47.1
0%, SMP 2h 25C	46.5	41.6	45.1

Table 13: Glass transition as calculated from DSC tests, varying thermal history, magnetic particle volume content, particle diameter, and magnetic material.

The DMTA tests gave higher values of T_g than the DSC tests. This is typical and is related to the DSC glass transition being weighted more towards smaller scale segmental mobility, which occur at lower temperatures than the G'' peak (Metzger et al. 2002). The trends between the DMTA and DSC T_g values are similar and are illustrated in the two figures below. It appears that there is an initial increase of T_g when there is a 1% volume fraction of magnetic particles added to the SMP, and then as particle volume is increased beyond this the values of T_g level out or drop. It is not clear what causes this initial increase and subsequent plateau effect.

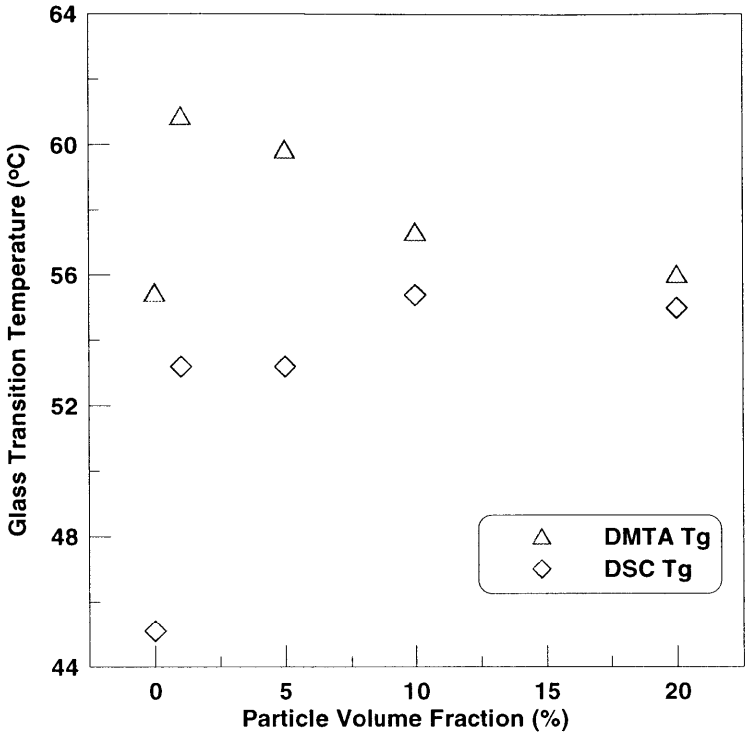

Figure 32: Particle volume fraction vs. glass transition temperature. DMTA and DSC calculated T_g for C2050 magnetic material particle diameter 6.71μm dispersed in SMP.

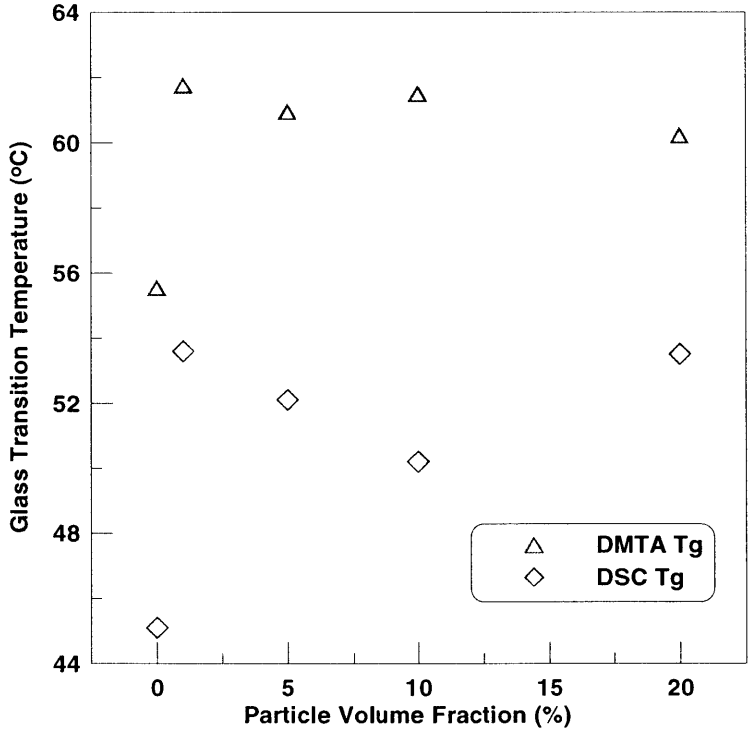

Figure 33: Particle volume fraction vs. glass transition temperature. DMTA and DSC calculated T_g for C2050 magnetic material particle diameter 43.6μm dispersed in SMP.

If the particle diameter is varied for the same volume content, the DSC and DMTA calculated values of T_g show opposite trends. The DMTA T_g increases with larger particles while the DSC T_g drops with increasing particle size. However when trend lines are added to the data points it appears that as particle sizes become infinitly small, for a fixed volume content, the value of T_g converges to approximately 57°C for both the DMTA and DSC data. This interesting trend is shown below.

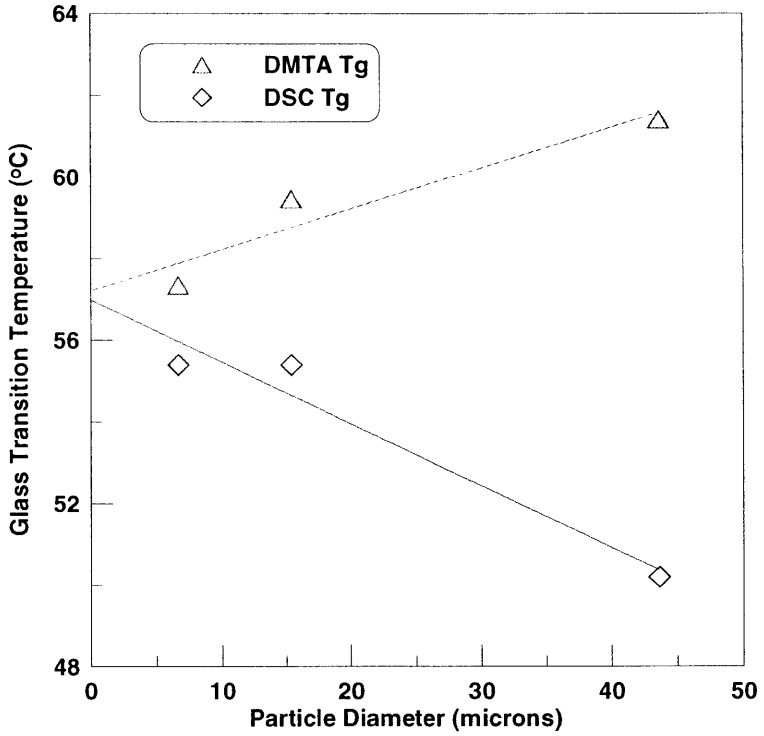

Figure 34: Particle Diameter vs. T_g for DMTA and DSC test method. 10% volume fraction of C2050 magnetic material with varying particle diameter dispersed in SMP.

The convergence point of T_g for the DSC and DMTA tests, at 57°C, suggests that there are some interesting interactions between the particle surface and the polymer which are influencing the glass transition temperature of the composite (Mckinley 2004). The zone where the polymer interacts with the surface of a particle can be called the 'inter-phase', there is more inter-phase present in the bulk material the smaller the particles become due to the increased amount of surface area presented by smaller

particles (Mckinley 2004). A plausible mechanism which would account for the trends seen in figure 34 would be if the inter-phase zone was more ordered then the bulk polymer material but was weakly attached to the bulk matrix (Mckinley 2004). The weak attachment of the inter-phase to the bulk matrix would cause the modulus of the material to drop as the amount of inter-phase increased, or in other words as the particle size dropped. Because DMTA measures T_g based on a mechanical measurement, the modulus drop would translate to a drop in the glass transition temperature. However, the increased order of the inter-phase would require a greater amount of thermal energy to induce chain mobility in the material, and because DSC measures glass transitions based on the thermal properties of the material, this increase in the thermal energy required would translate into an increase in the glass transition temperature as the amount of inter-phase increased, or in other words as the particle size gets smaller (Mckinley 2004). These are the trends seen in figure 34.

A consistent trend between the DMTA and DSC calculated T_g is that when magnetic particles are added to the SMP, T_g is increased; beyond this there does not appear to be any consistent trend in the data for varying particle volume content. This could indicate that there are other processing parameters which affect T_g and were not accounted for in this thesis. Such things may be the humidity during sample preparation, the slight difference in the ratio of part A and B each time a new sample was mixed, or variation in the room temperature cure time. It was mentioned before that all samples were allowed to sit at room temperature for a minimum of 1 hour, but beyond this there was no further control; some samples may have sat an hour and some 2 or 2 ½ hours. Future work is needed to determine if these other parameters affect the T_g of the material.

6 Conclusion

A significant amount of information pertaining to the feasibility of inductively-heated SMP is collected in this thesis. The tests performed and the research conducted will serve as the first steps in determining the feasibility of an inductively-heated shape memory polymer which relies on magnetic heating particles that are thermo regulated by their own Curie temperature. There remains a great deal more work that can be done and this section will serve as a guide for future work as well as a review of what was accomplished in this thesis.

6.1 Results Overview

6.1.1 Inductive Heating Results

Volumetric power generation of nickel zinc ferrite particles between 6.71 and 43.6 microns diameter was demonstrated to be between 135-1100 W/cm^3 for a 12.2 MHz, magnetic field strength of 422-545 A/m. The polymer melted in less than 20 seconds, and in some cases showed signs of polymer degradation, at an average volumetric power generation of 82 W/cm^3. Increased volume fractions of particles in the SMP diminishes volumetric power generation of the particle material; this may be due to a shielding effect the particles have on each other. Smaller particles have lower volumetric power generation; this is thought to be caused by some sort of change in the loss mechanism of the particles. The magnetic mode of heating in the particle material is believed to be via hysteresis losses, but no Curie temperature thermoregulation of the material was demonstrated. Heating and actuation of three complex shaped devices, a foam, a collapsed flower, and a flat flower, using a 10% volume content C2050 magnetic particle loaded SMP, was demonstrated in room temperature air using a 12.2 MHz 400 A/m alternating magnetic field.

6.1.2 Mechanical Test Results

The DMTA and strain recovery test showed that the modulus of the SMP increased as the volume content of particles was increased. The rubbery dynamic shear storage modulus was affected to a greater degree by the addition of particles than was the glassy modulus. With the addition of 20% volume content of particles the rubbery dynamic shear modulus showed an over all increase in modulus of roughly 394% as compared to the 137% increase shown in the glassy dynamic shear storage modulus.

Varying particle size between 6.71μm and 43.6μm did not have a significant effect on SMP mechanical properties until a volume fraction of 20% was reached. At 20% volume fraction the rubbery dynamic shear storage modulus varied by 21% and the glassy modulus by 13% for the above particle sizes. However this effect was in the opposite direction for the rubbery and glassy moduli, the smaller 6.71μm particles causing the rubbery modulus to increase by a greater amount, while the larger 43.6μm particles caused the glassy modulus increase by a greater amount then the rubbery modulus. This effect is believed to be caused by the different effect the increased surface area of smaller particles has on the glassy and rubbery phases of the SMP.

DSC and DMTA tests showed a rise in T_g upon the addition of 1% volume fraction of magnetic particles. Increasing volume content beyond this shows no consistent trends. It is believed that there are other parameters involved with the preparation and handling of the SMP which affect the T_g to a greater degree than the addition of magnetic particles.

The time the SMP was allowed to cure at 25°C before being cured at 80°C had a surprisingly significant effect on the mechanical properties of the material. The rubbery dynamic shear storage modulus and the glassy dynamic shear storage modulus varied by

82%, and 18% from the lowest to highest reading for varying 25°C cure times between 0-2 hours. This variation is almost as great as the variation caused by the addition of 10% by volume of particles.

6.2 Future Work and Improvements

6.2.1 Inductive Heating

A number of magnetic materials which show promise as heating particles in SMP were described in Chapter 2. Calorimetry testing of these materials as well as other promising materials should be conducted. It would also be useful to explore further the effect that particle size has on the volumetric power generation of promising materials. Much of this information may be found in a literature review as there is a rich library of research on a wide range of magnetic materials. Information that is not gleaned from a literature review must be acquired by testing. A calorimetry testing procedure similar to that used in this thesis can be employed but it is recommended that for future testing, medically safe magnetic field strengths and frequencies which lay within the $H_o f \leq 4.85\times10^8\ A\cdot turns/m\cdot s$ limits determined by Atkinson et al should be used (Atkinson et al. 1984), as these are the fields which would be used in a medical setting. This was not done in this thesis due to constraints on the purchasing of equipment.

Ideally, the volumetric power generation of a material could be determined for varying field strengths and frequencies which lay within the above mentioned medical limits. A three-axis plot, with field strength on one axis, field frequency on another, and volumetric power generation on the last would provide the frequency and field strength at which a material heats most efficiently. As described earlier a number of material

properties, such as coercivity and remnance, influence the field strength and frequency where peak effective heating occurs.

Further investigation into the proposed shielding effect that is believed to be the cause of the drop in volumetric power generation of the particles at increasing volume content of particles in the SMP would be interesting to investigate. This is not a high priority as it appears from this initial study that a volume content of less then 10% will be sufficient to heat and actuate the SMP even with the diminished heating efficiency caused by possible shielding. The observed drop in heating efficiency associated with shielding was roughly 40% for the 20% volume fraction SMP as compared with the 1% volume fraction SMP for all particle sizes and magnetic field strengths tested. This is a substantial drop but even greater improvements in the heating efficiency of inductively-heated SMP are offered by optimizing or adjusting other parameters. Some of these possible improvements are outlined below.

A promising method of increasing the hysteresis loss of the magnetic heating particles, and thus lowering the volume fraction of particles needed to heat the SMP, is by using a rotating magnetic field instead of an alternating magnetic field. Ferromagnetic particles between 0.6μm and 0.2μm of size and embedded in a non magnetic matrix have been shown to dissipate as much as 4.5 times the amount of energy when exposed to a rotating magnetic field as compared with an alternating magnetic field (Bottoni et al. 1974). Rotating magnetic fields are not expected to induce any more tissue heating than alternating magnetic fields. However no information about the safety limits of rotational magnetic field exposure for human beings was found. The question of safe field exposure will have to be answered if rotational fields are to be used.

There is also evidence that particles near the sub-domain size, around 50 nm for magnetite, exhibit a dramatic increase in heat production due to hysteresis loss. 46 nm magnetite particles have been shown to produce roughly 3 times the amount of heat energy due to hysteresis loss as 416 nm size particles when exposed to a medically safe alternating magnetic field (Ma et al. 2004). The use of nanometer sized particles not only shows promise to improve the heating efficiency of inductively-heated SMP but particles on the nanometer size scale have also been shown to have a minimal impact on the mechanical properties of a polymer, even at very high volume contents where the average inter-particle distance is only one nanometer (Glotzer 2003).

6.2.2 Mechanical Testing

Time limitations prevented a more extensive array of large strain recovery tests from being performed. More of this type of testing would be a useful next step. In addition, the influence of smaller particle sizes, especially on the nanometer size scale, and varying particle shapes should be investigated. Specifically, particle sizes in the 50 nanometer size range may offer improved heating characteristics and so the impact of these size particles on the mechanical properties of the SMP should be determined. For future it is important to maintain a consistent preparation and processing protocol for the SMP of the material. Especially important is the 25˚C cure time, this should be as consistent as possible between batches. This will help ensure consistent mechanical properties of the SMP material allowing the effects of particle addition to be seen more clearly. If it is not possible to provide each sample with the same thermal history, it is recommended that the material be allowed to cure at 25˚C for at least an hour as it appears that after this time period the properties of the material level out. Further

investigation into the effect of the 25°C cure time on the plain SMP material is also needed.

The effect of particle dispersion on the heating efficiency and the mechanical properties of SMP should be investigated. The systematic testing of different mixing techniques, observing how well particle dispersion occurs for each technique, and how this dispersion affects the mechanical and heating efficiency of the material would be a first good step. The use of coatings or surfactants to improve dispersion may be another possibility and also deserves further research.

The problems with dispersing Fe_3O_4 particles in the SMP should also be solved. An improvement in the process of mixing the SMP or the use of some sort of particle coating may offer solutions to this problem. Once a solution is found, it could potentially be applied to other types of reactive particles which one wishes to add into the SMP.

6.3 Final Comments

The work conducted in this thesis shows the feasibility of inductively-heated SMP using dispersed magnetic particles. From these initial tests, it appears that the addition of a 10% volume content of particles provides sufficient heating for SMP actuation in air. A 10% volume content of particles is also shown to have a minimal effect on the mechanical properties of the SMP, showing an impact that is comparable to allowing the SMP to sit at room temperature for varying amounts of time before an elevated temperature cure.

Research in the field of hyperthermia has demonstrated particle materials which have the benefit of a Curie temperature thermoregulation mechanism. Using such types of particles dispersed in SMP would create a material with a combination of attractive

characteristics for medical devices which are delivered via a catheter. Such a material combination would allow the actuation of a shape memory material, remotely (via magnetic fields), in a simple and safe manner (simplicity being provided by the flip of a switch to turn on the magnetic field and safety due to the built in thermoregulation of the material's Curie temperature). These characteristics are what make this inductively-heated SMP such an attractive and promising material for medical devices. The use of inductively-heated SMP for medical devices has other indirect benefits, such as the following:

1. Because heating and actuation are remote, power transmission lines to a device are eliminated, allowing smaller catheters to be used, increasing the access of a device to narrower vessels.
2. The geometric design of a device is uncoupled from the heating mechanism used. Device shapes that were impossible to heat with laser or resistive elements can be easily heated using dispersed particles.
3. The joint between the device and the power transmission line is eliminated,

The novel properties of inductively-heated shape memory polymer give engineers and physicians another tool for designing new types of life saving devices.

Bibliography

A.H.A. (2003). Heart Disease and Stroke Statistics - 2004 Update. Dallas, Texas, American Heart Association: 13-15.

Atkinson, W., I. Brezovich and D. Chakraborty (1984). "Usable Frequencies in Hyperthermia with Thermal Seeds." IEEE Transactions on Biomedical Engineering **31**(1): 70-75.

Bertotti, G. (1998). Hysteresis in magnetism : for physicists, materials scientists, and engineers. San Diego, Academic Press.

Bliznakov, E. D., C. C. White and M. T. Shaw (2000). "Mechanical properties of blends of HDPE and recycled urea-formaldehyde resin." Journal of Applied Polymer Science **77**(14): 3320-3227.

Bonet, E., W. Wernsdorfer, B. Barbara, A. Benoit, D. Mailly and A. Thiaville (1999). "Three-Dimensional Magnetization Reversal Measurments in Nanoparticles." Physical Review Letters **83**: 4188-4191.

Bottoni, G., D. Candolfo, A. Cecchetti and F. Masoli (1974). "Ratio of the rotational loss to hysteresis loss in ferrimagnetic powders." Magnetics, IEEE Transactions on **10**(2): 317-320.

Bozorth, R. M. and A. S. f. Metals (1959). Magnetic properties of metals and alloys. Cleveland.

Cassel, B. (2004). "Measuring the Glass Transition of Amorphous Engineering Thermoplastics." TA Instruments, www.tainst.com.

Cetas, T. C., E. J. Gross and Y. Contractor (1998). "A ferrite core/metallic sheath thermoseed for interstitial thermal therapies." IEEE Transactions On Bio-Medical Engineering **45**(1): 68-77.

Escobar, M. A. and R. Valenzuela (1983). "Analytical Prediction of the Magnetization Curve and the Ferromagnetic Hysteresis Loop." Journal of Applied Physics **54**: 5935-5940.

Glotzer, S. C. (2003). "Nanoscale science-Complex rules for soft systems." Nature Materials **2**(11): 713-714.

Goldman, A. (1990). Modern ferrite technology. New York, Van Nostrand Reinhold.

Gray, Cammarano and Jones (2003). Heating of Magnetic Materials by Hysteresis Effects Patent US659923B1 issued July 29, 2003. USA.

http://www.ndt-ed.org/EducationResources/CommunityCollege/EddyCurrents/Physics/mutualinductance.htm.

Jonathan Hartmann, M. (2003). Presentation and Conversation November 17, 2004.

Jordan, A., P. Wust, H. Fahling, W. John, A. Hinz and R. Felix (1993). "Inductive heating of ferrimagnetic particles and magnetic fluids: physical evaluation of their potential for hyperthermia." International Journal Of Hyperthermia: The Official Journal Of European Society For Hyperthermic Oncology, North American Hyperthermia Group **9**(1): 51-68.

Jovicich, J. (2004). Presentation and Conversation on MRI equipment at Massachusetts General Hospital April 28, 2004.

Kim, B. K., S. Y. Lee and M. Xu (1996). "Polyurethanes having shape memory effects." Polymer **37**(26): 5781-5793.

Kimura, I. and T. Katsuki (1986). "VLF induction heating for clinical hyperthermia." Magnetics, IEEE Transactions on **22**(6): 1897-1900.

Kittel, C. (1949). "Physical Theory of Ferromagnetic Domains." Reviews of Modern Physics **21**: 541-583.

Lamba, N. M. K., K. A. Woodhouse, S. L. Cooper and M. D. Lelah (1998). Polyurethanes in biomedical applications. Boca Raton, CRC Press.

Lendlein, A. and R. Langer (2002). "Biodegradable, Elastic Shape-Memory Polymers for Potential Biomedical Applications." Science **296**: 1674-1676.

Lin, I.-n., R. Mishra and G. Thomas (1984). "Interaction of magnetic domain walls with microstructural features in spinel ferrites." Magnetics, IEEE Transactions on **20**(1): 134-139.

Ma, M., Y. Wu, J. Zhou, Y. Sun, Y. Zhang and N. Gu (2004). "Size dependence of specific power absorbtion of Fe3O4 particles in AC magnetic field." Journal of Magnetism and Magnetic Materials(268): 33-39.

Macosko, C. W. (1994). Rheology : principles, measurements, and applications. New York, VCH.

Magana, L. F., M. A. Escobar and R. Valenzuela (1986). "Effect of the Grain Size Distribution on the Ferromagnetic Hysteresis Loop." Physica Status Solidi A-Applied Research **97**(2): 495-500.

Maitland, D. J., M. F. Metzger, D. Schumann, A. Lee and T. S. Wilson (2002). "Photothermal Properties of Shape Memory Polymer Micro-Actuators for Treating Stroke." Lasers in Surgery and Medicine **30**: 1-11.

McCurrie, R. A. (1994). Ferromagnetic Materials Structure and Properties. London, Academic Press London.

Mckinley, G. (2004). Personal Communication.

Meesiri, Menczel, Guar and Wunderlich (1982). "Phase-Transitions in Mesophase Macromolecules .3. The Transitions in poly(ethylene terephthalate-co-p-oxybenzoate)." Journal of Polymer Science Part B-Polymer Physics **20**(4): 719-728.

Metzger, M. F., T. S. Wilson, D. Schumann, D. L. Matthews and D. J. Maitland (2002). "Mechanical Properties of Mechanical Actuator for Treating Ischemic Stroke." Biomedical Microdevices **4**(2): 89-96.

Oleson, J. R. (1984). "A Review of Magnetic Induction Methods for Hyperthermia Treatment of Cancer." IEEE Transactions on Biomedical Engineering **BME-31**(1): 91-96.

Otsuka, K. and C. M. Wayman (1998). Shape memory materials. New York, Cambridge University Press.

Paulus, J. A. and R. D. Tucker (1995). Cobalt Palladium Seeds for Thermal Treatment of Tumors Patent US5429583 issued July 4,.

Rudnev, V. (2003). Handbook of induction heating. New York, Marcel Dekker.

Schetky, L. M. (1979). "Shape Memory Alloys." Scientific American **241**(5): 74-82.

Snelling, E. C. (1969). Soft Ferrites Properties and Applications. London, ILIFFE BOOKS LTD.

Sperling, L. H. (1986). Introduction to physical polymer science. New York, Wiley.

Stauffer, P., T. Cetas, A. Fletcher, D. DeYoung, M. Dewhirst, J. Oleson and R. Roemer (1984). "Observations on the Use of Ferromagnetic Implants for Inducing Hyperthermia." IEEE Transactions on Biomedical Engineering **31**(1): 76-90.

Stauffer, P. R., P. K. Sneed, H. Hashemi and T. L. Phillips (1994). "Practical induction heating coil designs for clinical hyperthermia with ferromagnetic implants." Biomedical Engineering, IEEE Transactions on **41**(1): 17-28.

Swain, M. V. (1986). "Shape Memory Behavior in Partially-Stabilized Zirconia Ceramics." Nature **322**(6076): 234-236.

Wetzel, E. and B. Fink (2001). Feasibility of Magnetic Particle Films for Curie Temperature-Controlled Processing of Composite Materials, Army Research Lab.

Wilson, T. (2004). Personal Communication.

Zhen, Z. (1977). Magnetism and metallurgy of soft magnetic materials. Amsterdam ; New York, North-Holland Pub. Co. : sole distributors for the U.S.A. and Canada, Elsevier North-Holland.

Appendix A: Heating Curves

Heating data points for the inductive heating experiments. Each data point is the average of three measurements taken at the same test settings. All error bars are + or – two standard deviations. The curve which is repeated in each plot, denoted by the black dots, represents temperature rises recorded for the control sample which had no magnetic particles dispersed in it. The fitted curves are the linear fits used to calculate power dissipation.

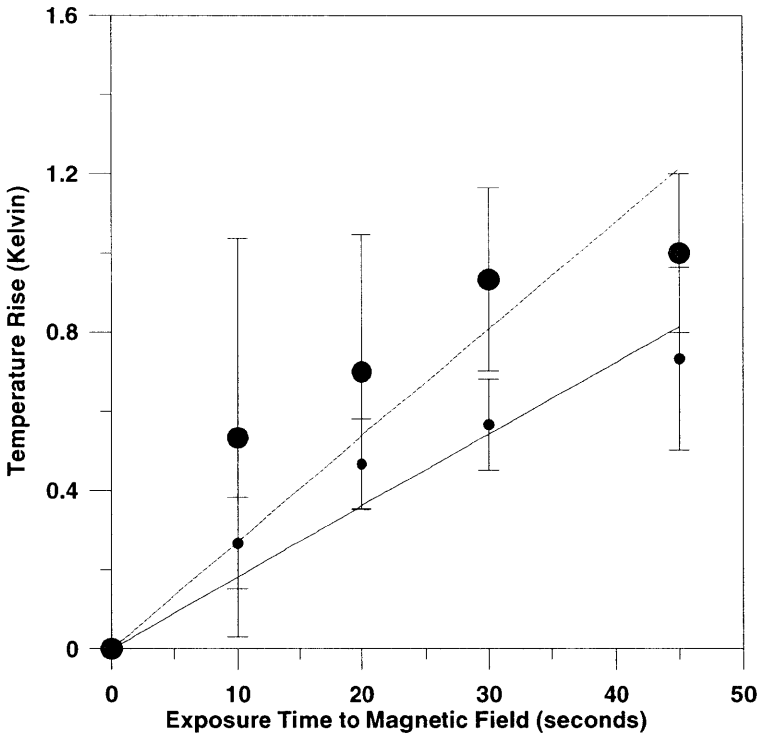

Figure A.1: 1% volume content C2050 SMP, 6.71μ particle diameter and 422.3 A/m field strength.

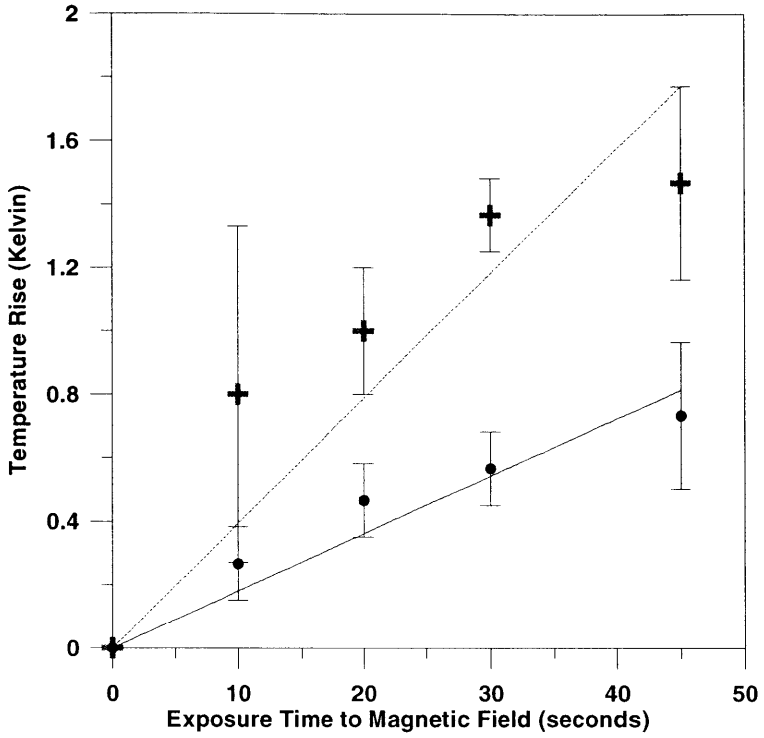

Figure A.2: 1% volume content C2050 SMP, 43.6μ particle diameter and 422.3 A/m field strength.

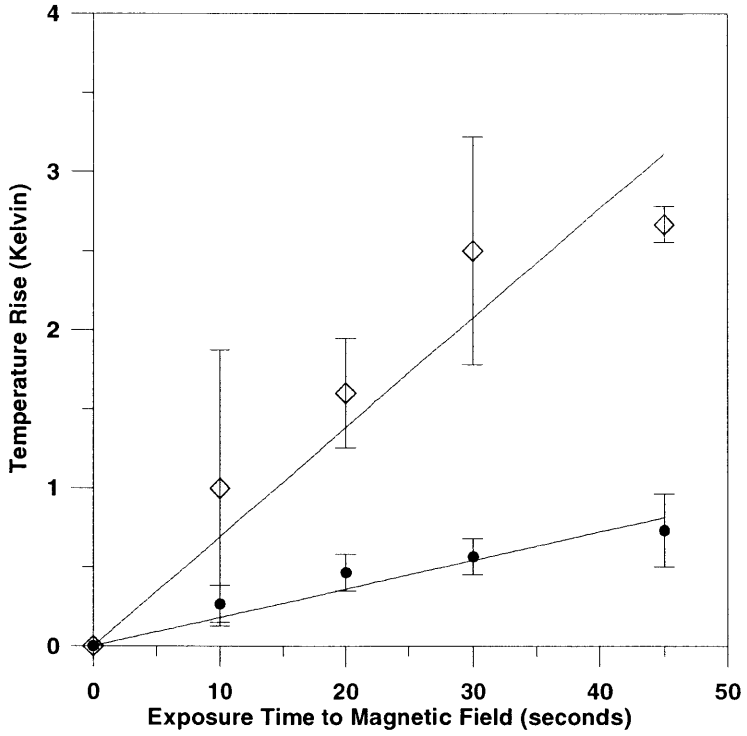

Figure A.3: 5% volume content C2050 SMP, 6.71μ particle diameter and 422.3 A/m field strength.

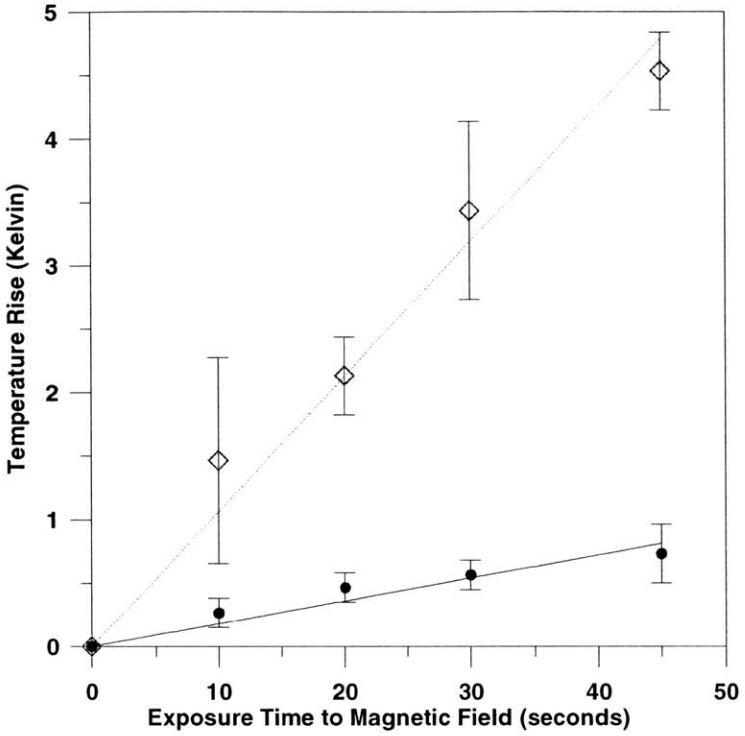

Figure A.4: 5% volume content C2050 SMP, 43.6μ particle diameter and 422.3 A/m field strength.

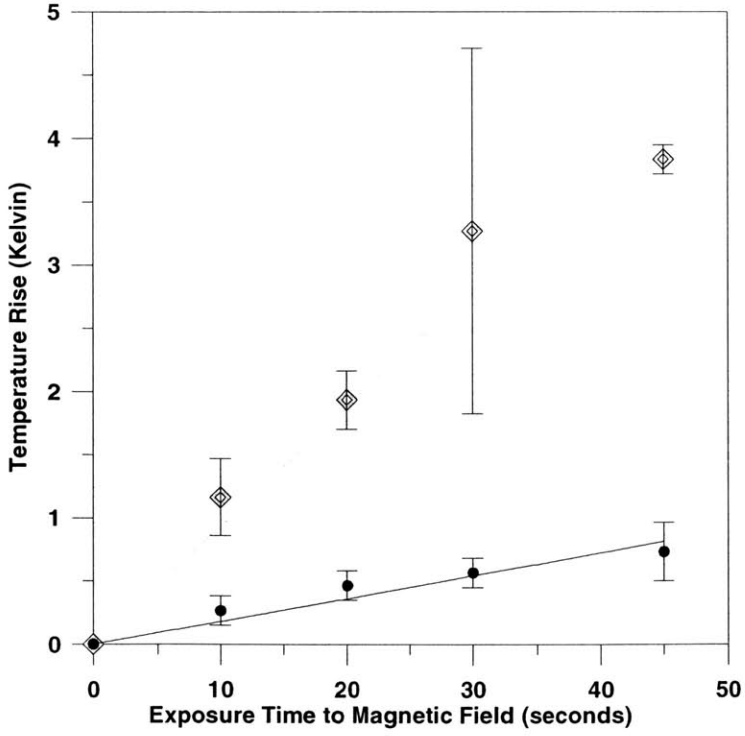

Figure A.5: 10% volume content C2050 SMP, 6.71μ particle diameter and 422.3 A/m field strength.

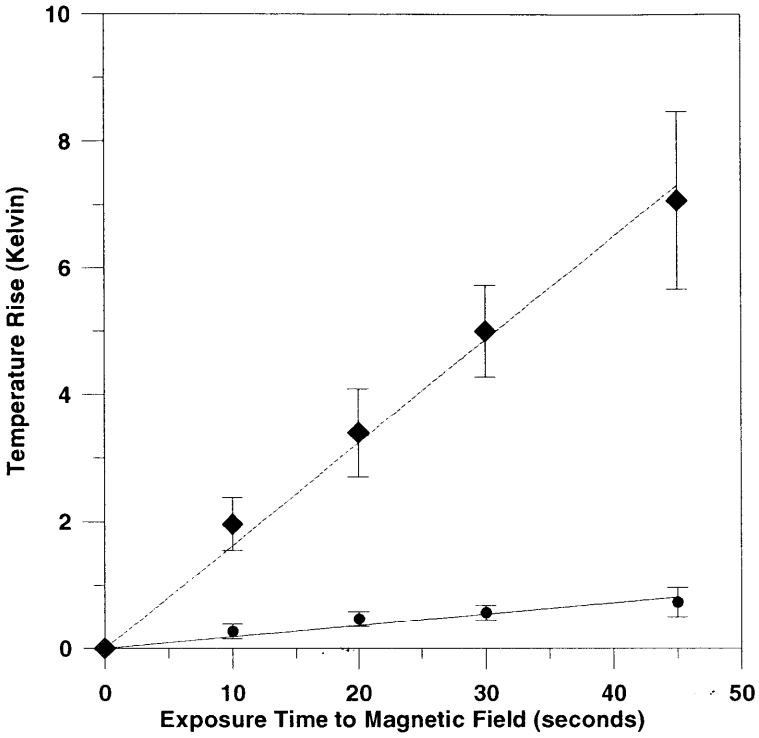

Figure A.6: 10% volume content C2050 SMP, 15.4μ particle diameter and 422.3 A/m field strength.

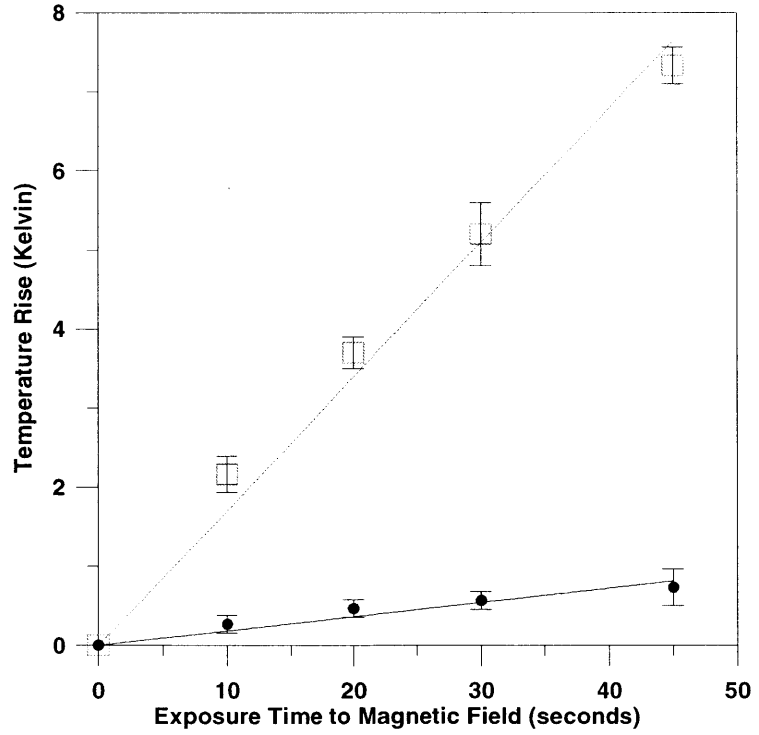

Figure A.7: 10% volume content C2050 SMP, 43.6μ particle diameter and 422.3 A/m field strength.

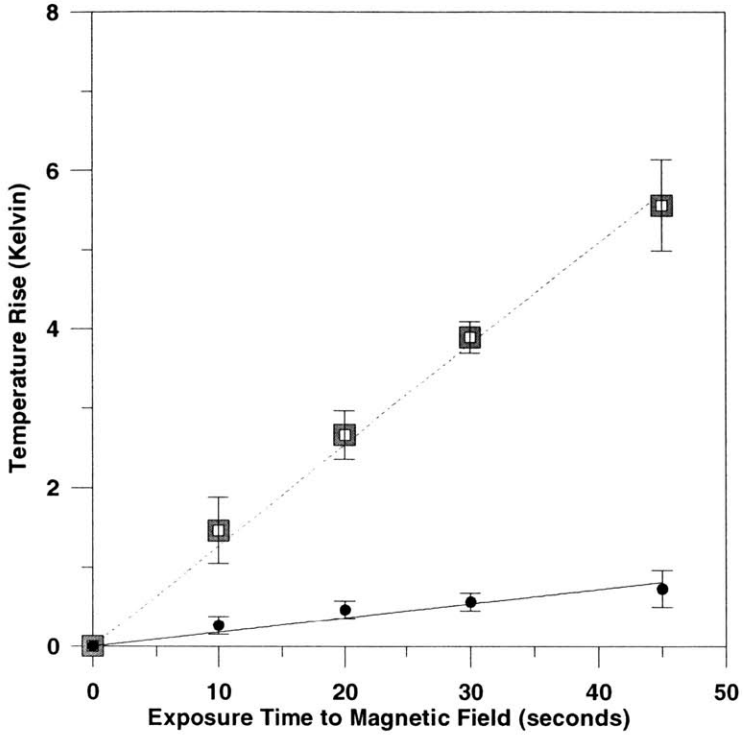

Figure A.8: 20% volume content C2050 SMP, 6.71μ particle diameter and 422.3 A/m field strength.

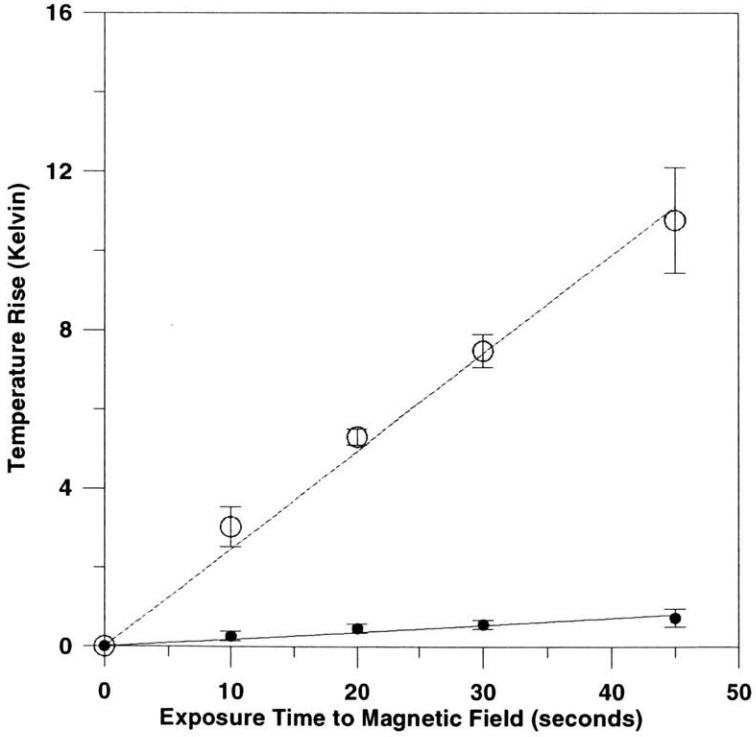

Figure A.9: 20% volume content C2050 SMP, 43.6μ particle diameter and 422.3 A/m field strength.

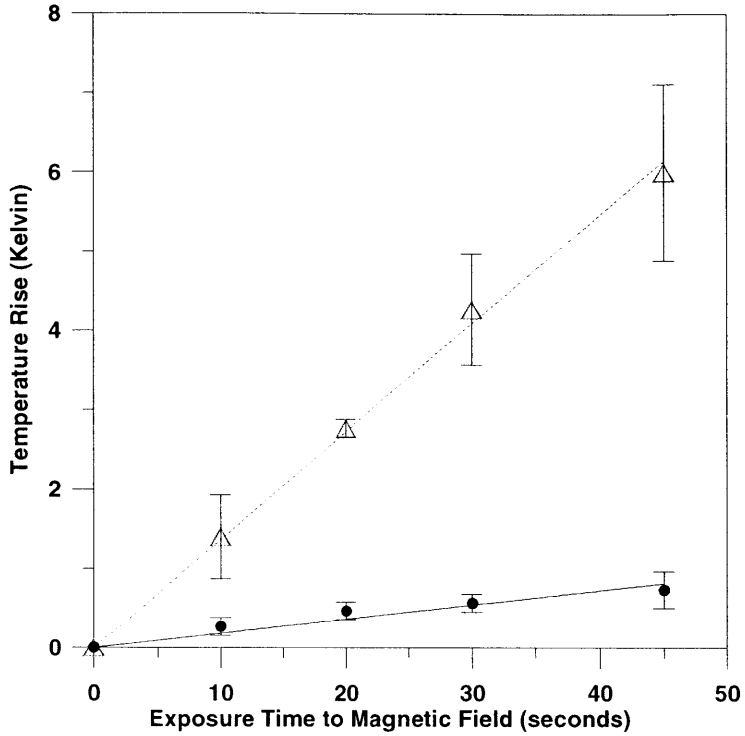

Figure A.10: 10% volume content N40 SMP, 43.6μ particle diameter and 422.3 A/m field strength.

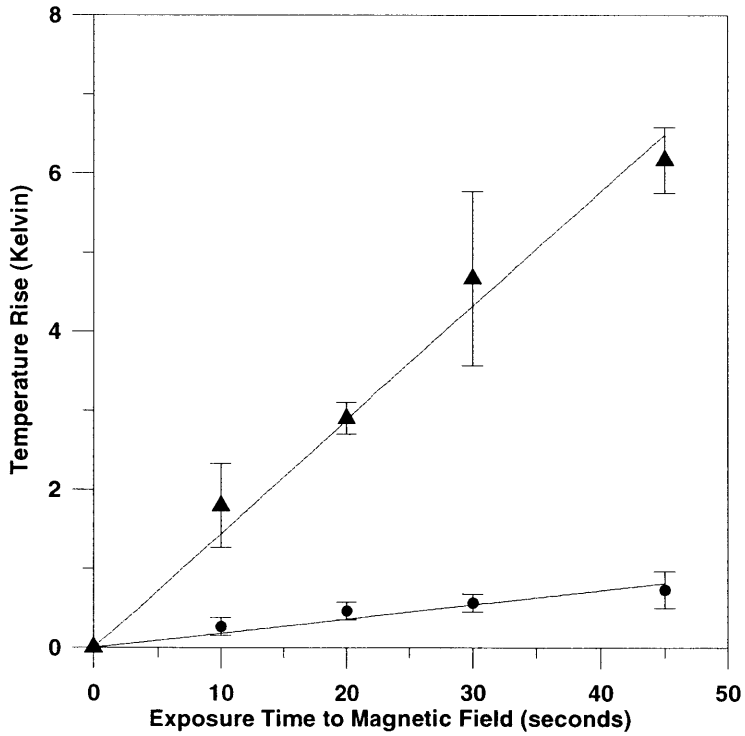

Figure A.11: 10% volume content CMD5005 SMP, 43.6μ particle diameter and 422.3 A/m field strength.

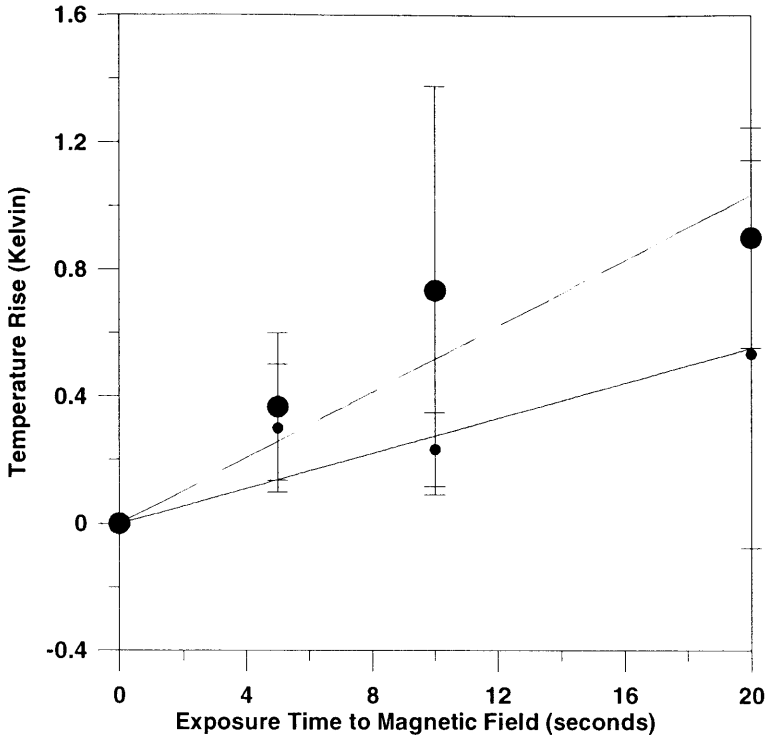

Figure A. 12: 1% volume content C2050 SMP, 6.71μ particle diameter and 422.3 A/m field strength.

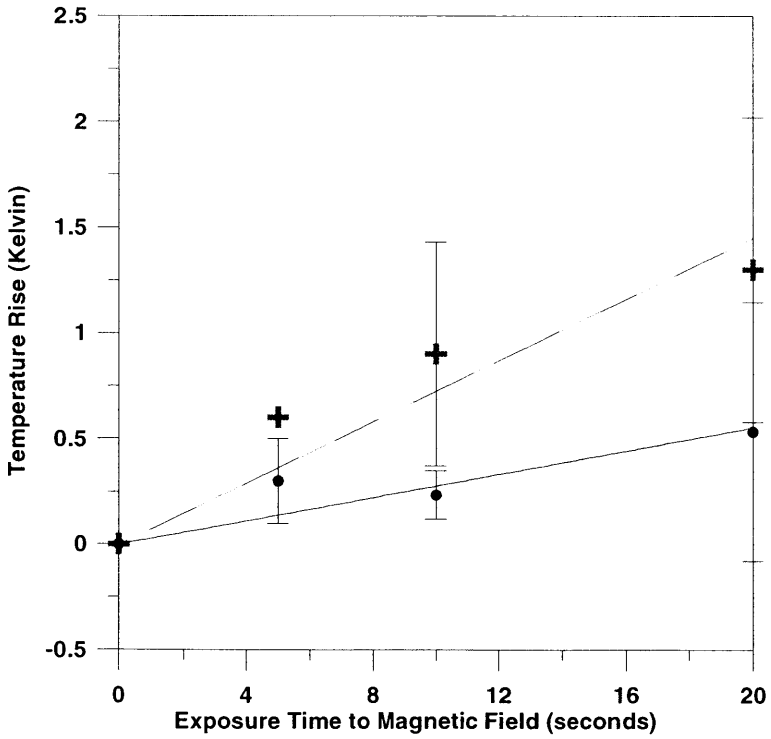

Figure A. 13: 1% volume content C2050 SMP, 43.6μ particle diameter and 422.3 A/m field strength.

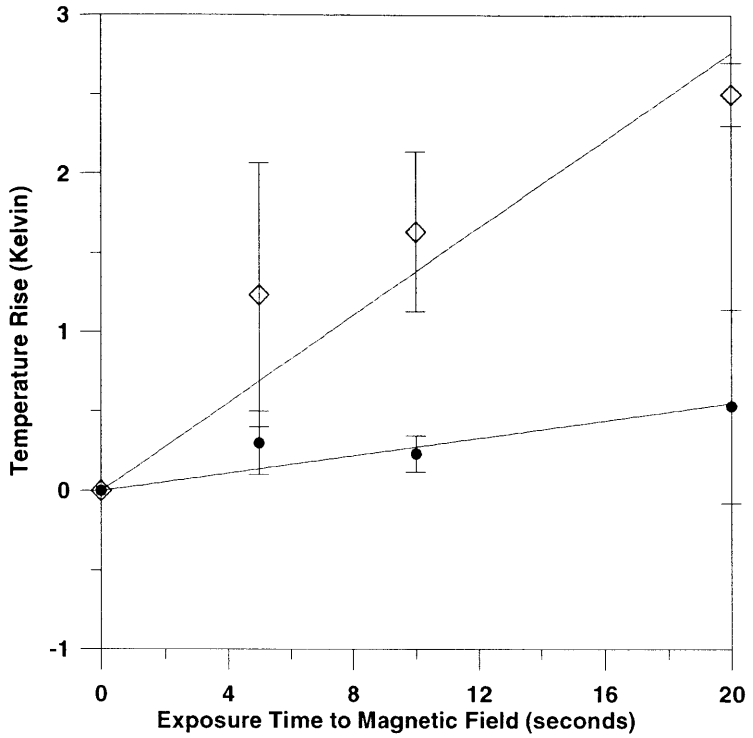

Figure A. 14: 5% volume content C2050 SMP, 6.71μ particle diameter and 422.3 A/m field strength.

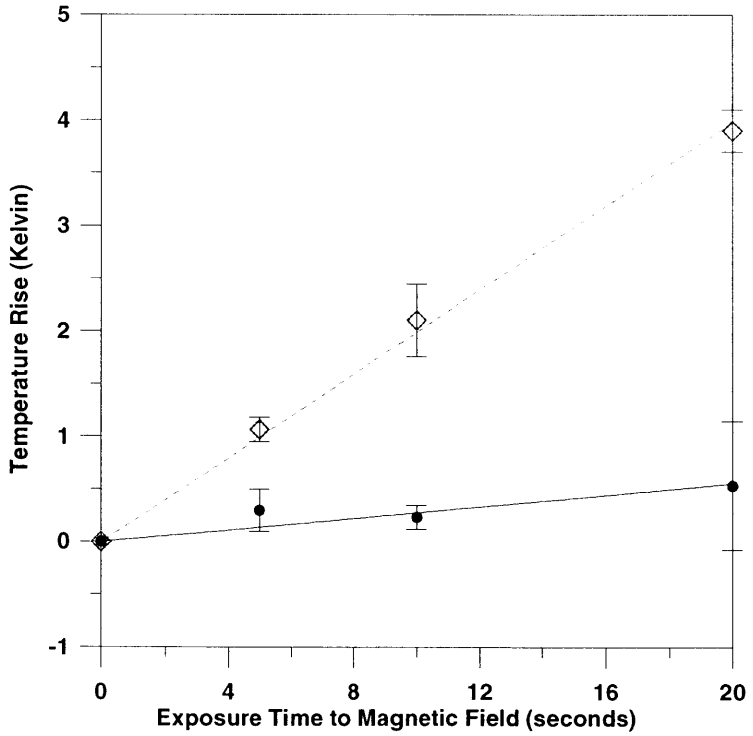

Figure A. 15: 5% volume content C2050 SMP, 43.6μ particle diameter and 422.3 A/m field strength.

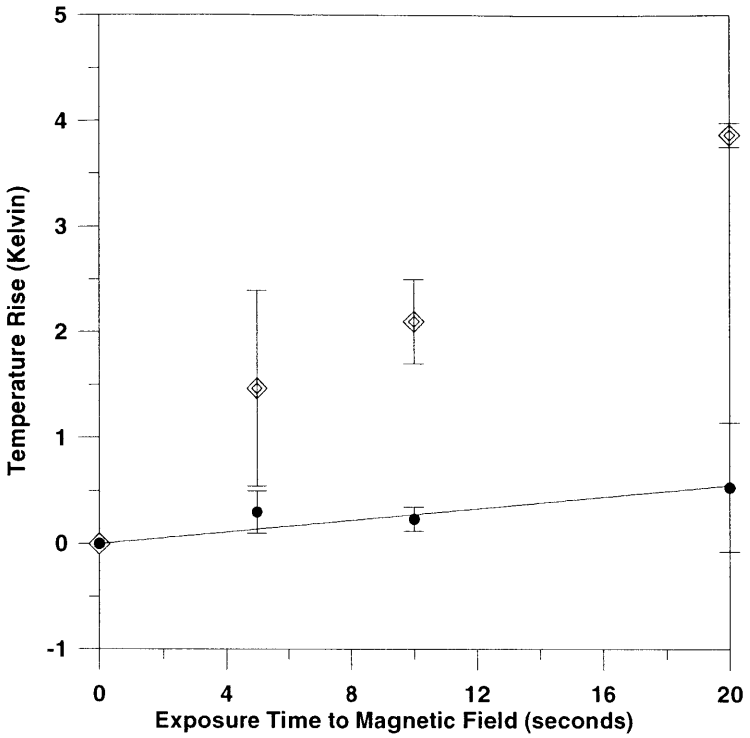

Figure A. 16: 10% volume content C2050 SMP, 6.71μ particle diameter and 422.3 A/m field strength.

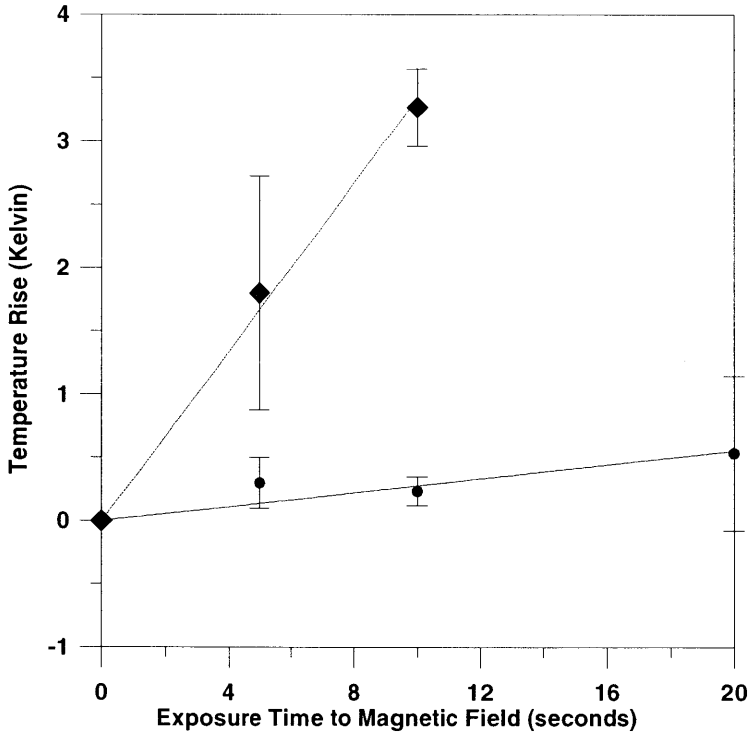

Figure A. 17: 10% volume content C2050 SMP, 15.4μ particle diameter and 422.3 A/m field strength.

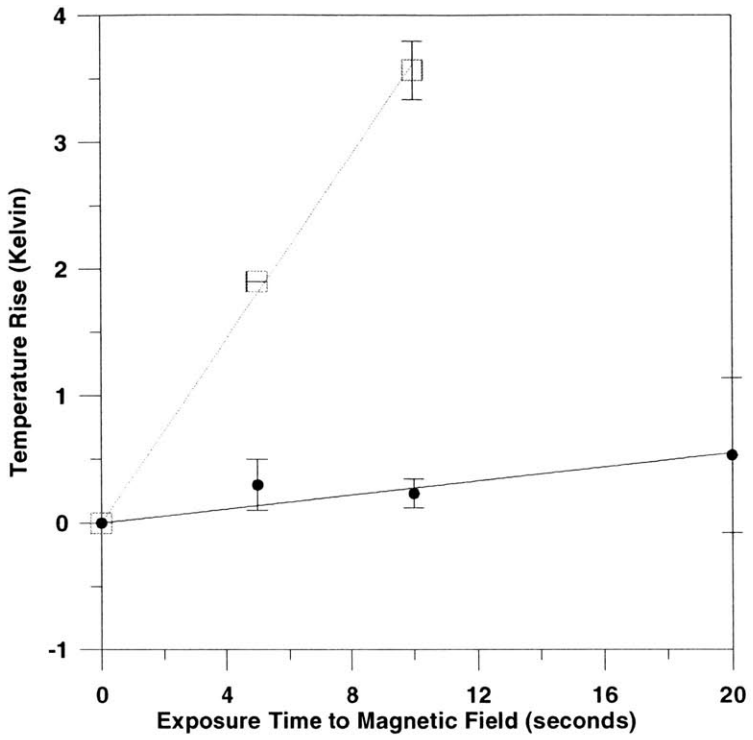

Figure A. 18: 10% volume content C2050 SMP, 43.6μ particle diameter and 422.3 A/m field strength.

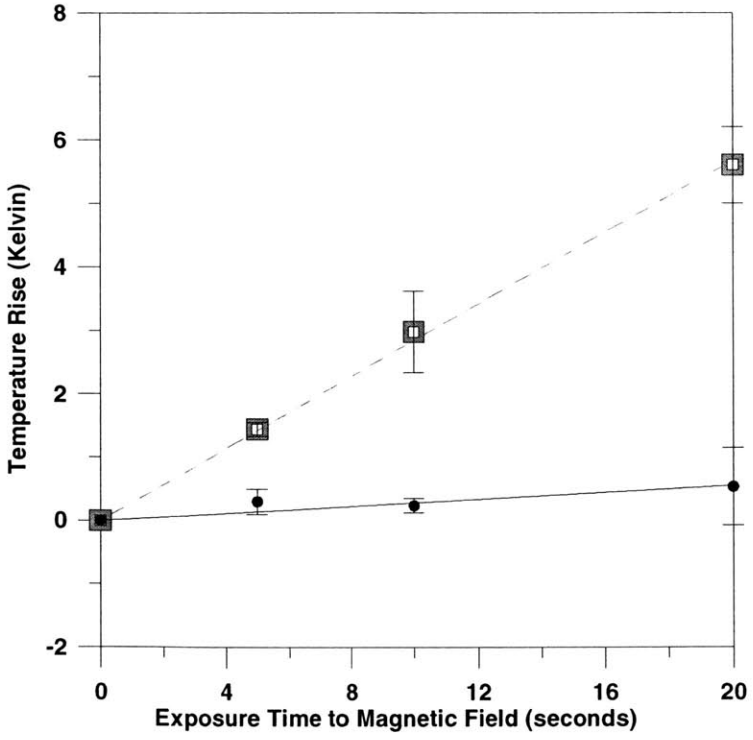

Figure A. 19: 20% volume content C2050 SMP, 6.71μ particle diameter and 422.3 A/m field strength.

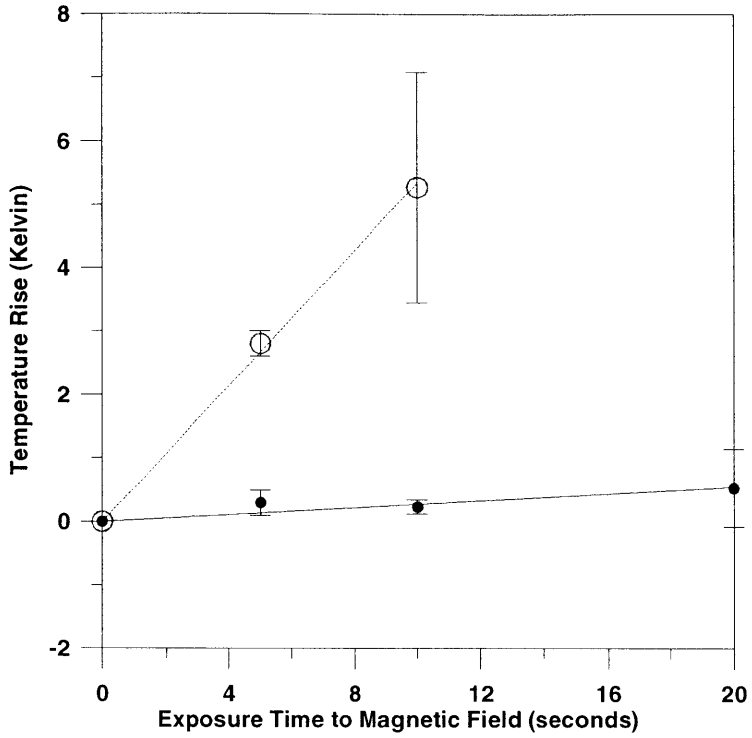

Figure A. 20: 20% volume content C2050 SMP, 43.6μ particle diameter and 422.3 A/m field strength.

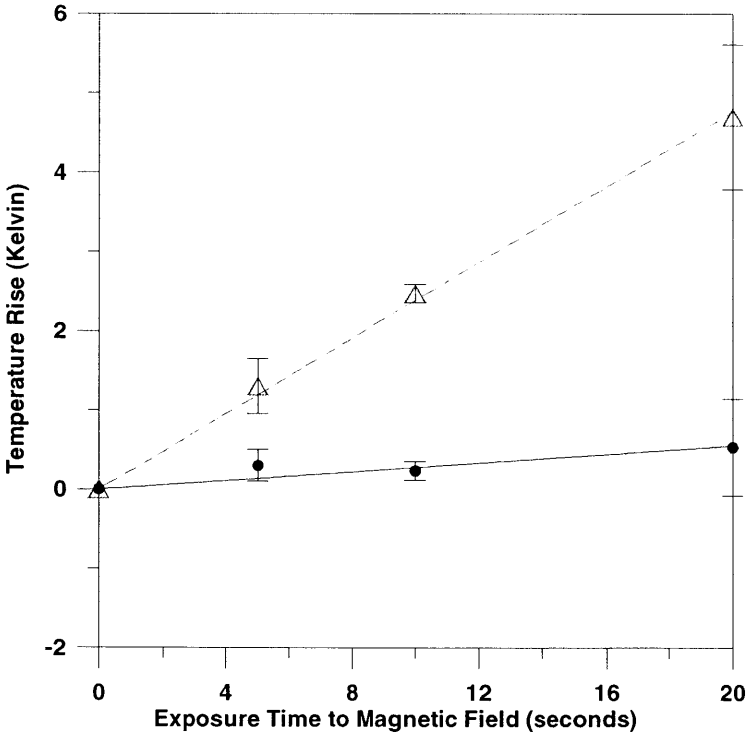

Figure A. 21: 10% volume content N40 SMP, 43.6μ particle diameter and 422.3 A/m field strength.

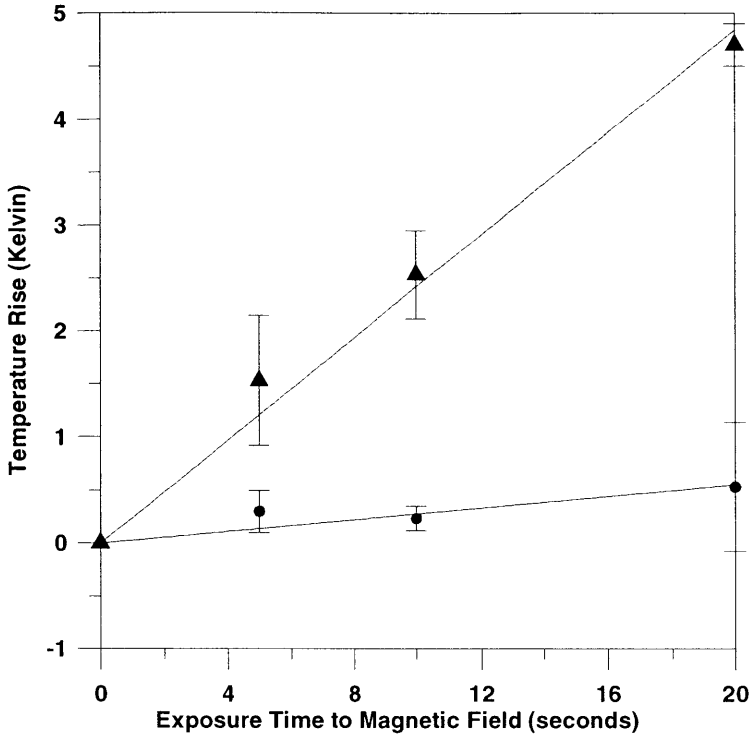

Figure A. 22: 10% volume content CMD5005 SMP, 43.6μ particle diameter and 422.3 A/m field strength.

Appendix B: DMTA Curves

Test curves from the DMTA test are shown below. Dynamic shear storage modulus, G', dynamic shear loss modulus, G'', and the loss tangent, tan (delta), are all graphed.

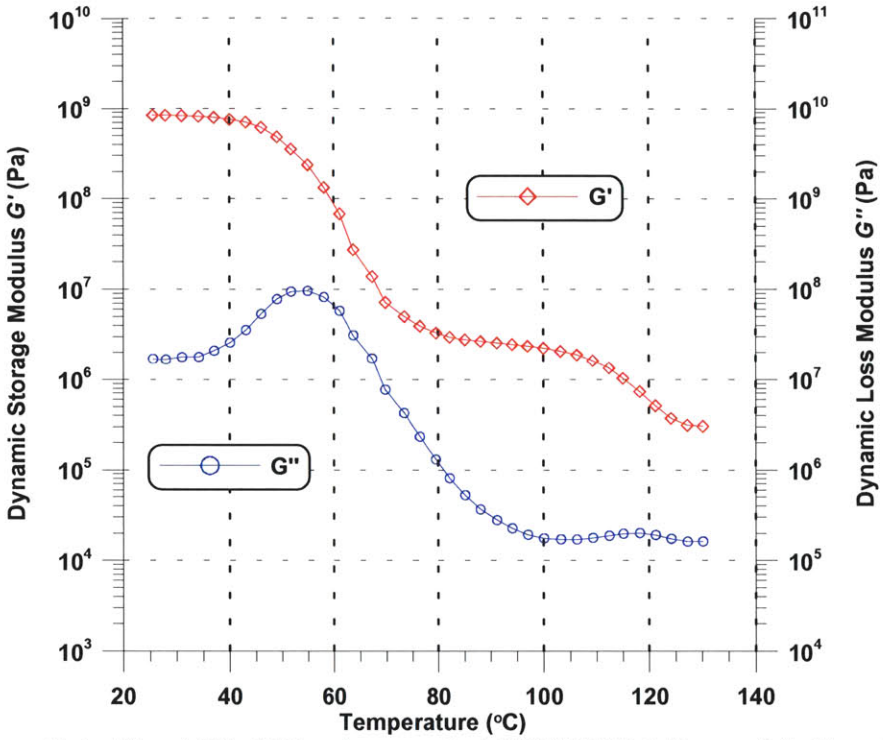

Figure B. 1: G' and G'' of 1% volume content C2050 SMP, 6.71μ particle diameter.

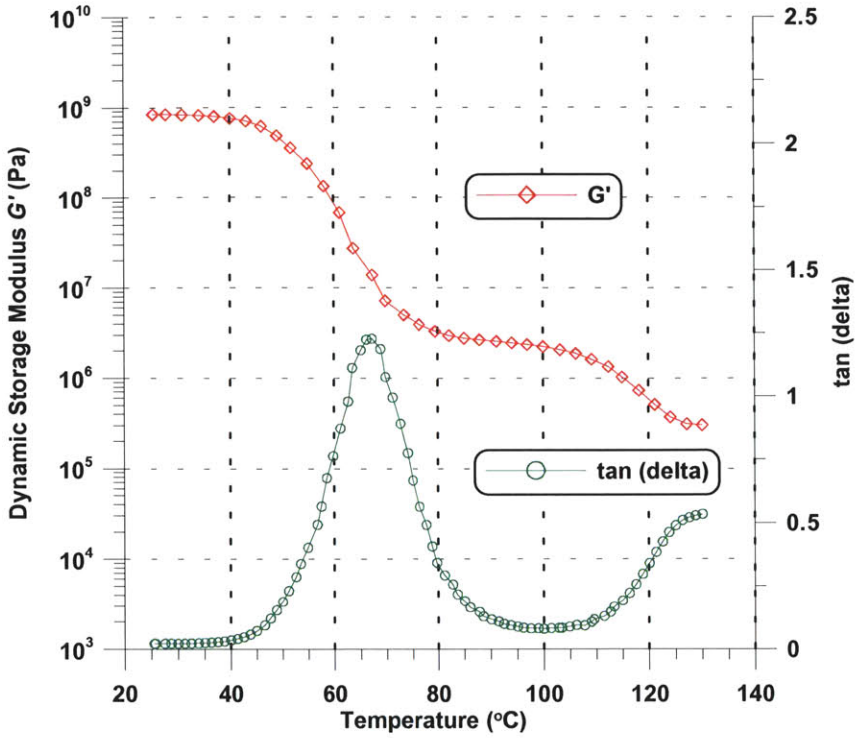

Figure B. 2: G' and tan (delta) of 1% volume content C2050 SMP, 6.71μ particle diameter.

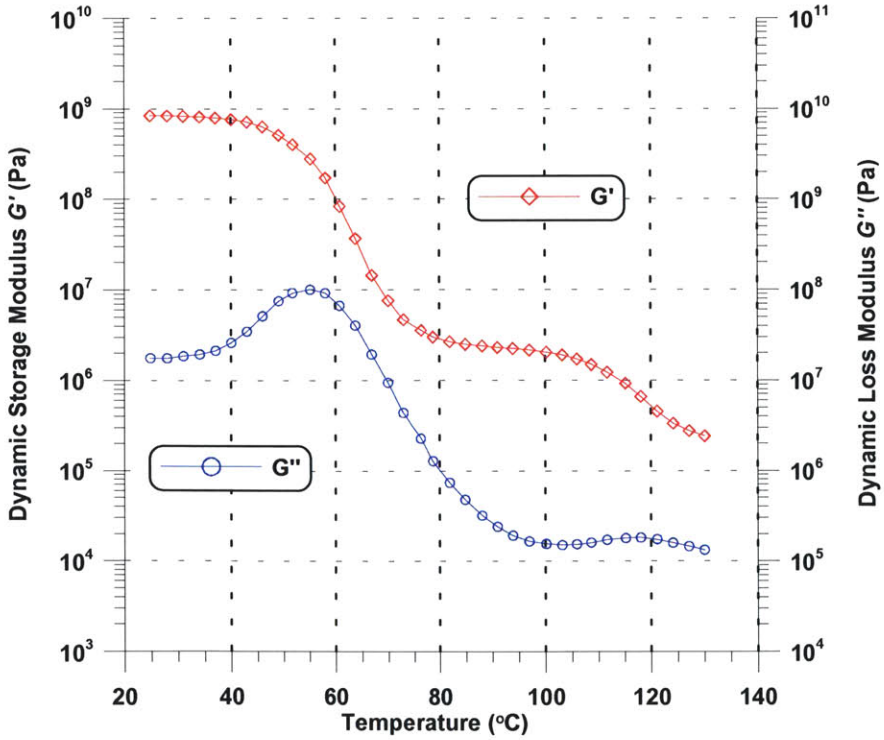

Figure B. 3: G' and G'' of 1% volume content C2050 SMP, 43.6μ particle diameter.

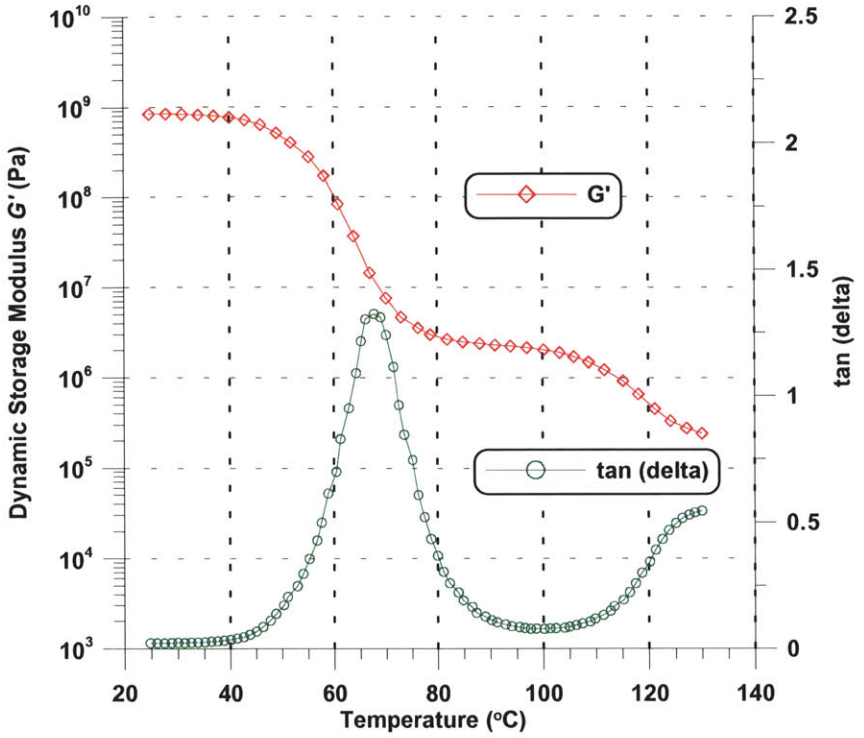

Figure B. 4: G' and tan (delta) of 1% volume content C2050 SMP, 43.6μ particle diameter.

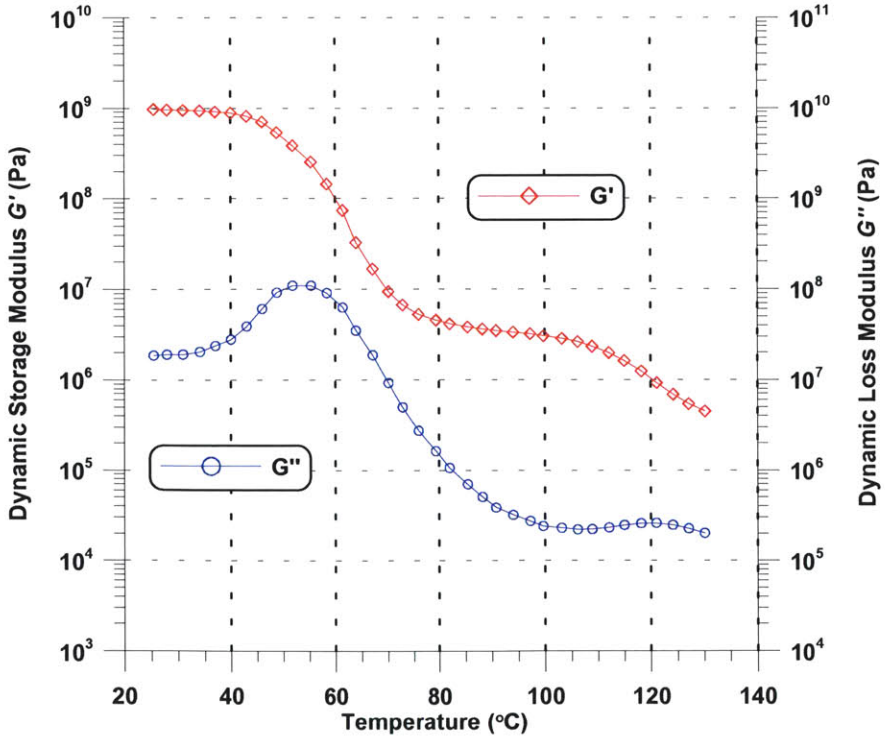

Figure B. 5: G' and G'' of 5% volume content C2050 SMP, 6.71μ particle diameter.

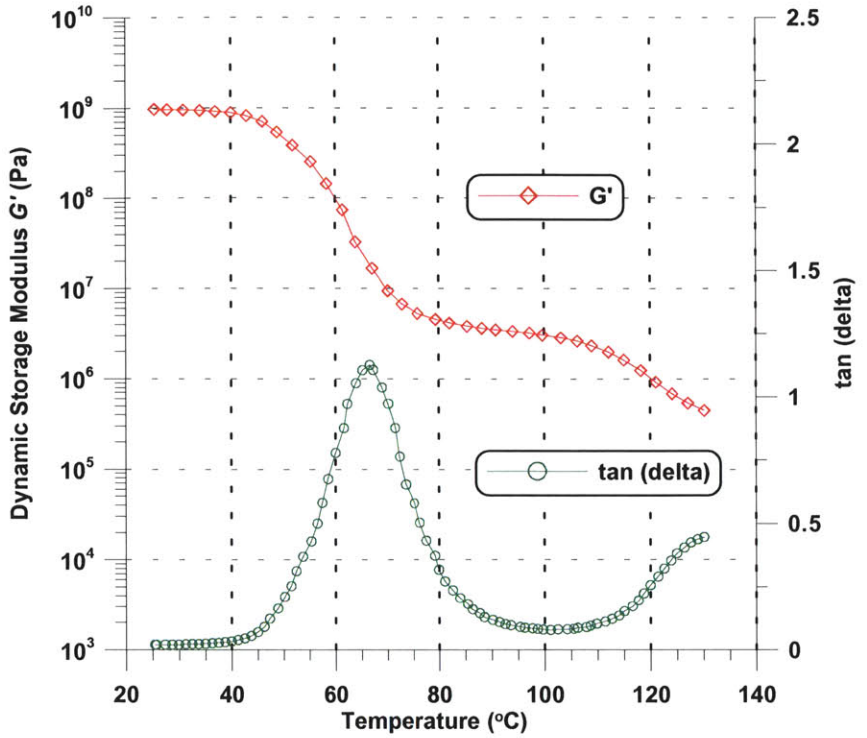

Figure B. 6: G' and tan (delta) of 5% volume content C2050 SMP, 6.71μ particle diameter.

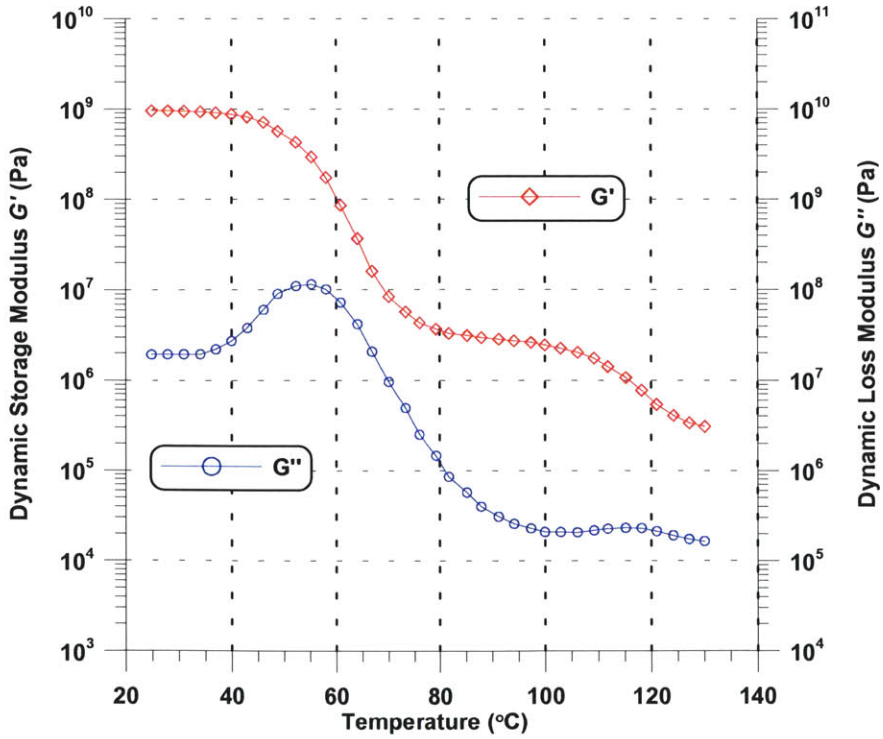

Figure B. 7: G' and G'' of 5% volume content C2050 SMP, 43.6μ particle diameter.

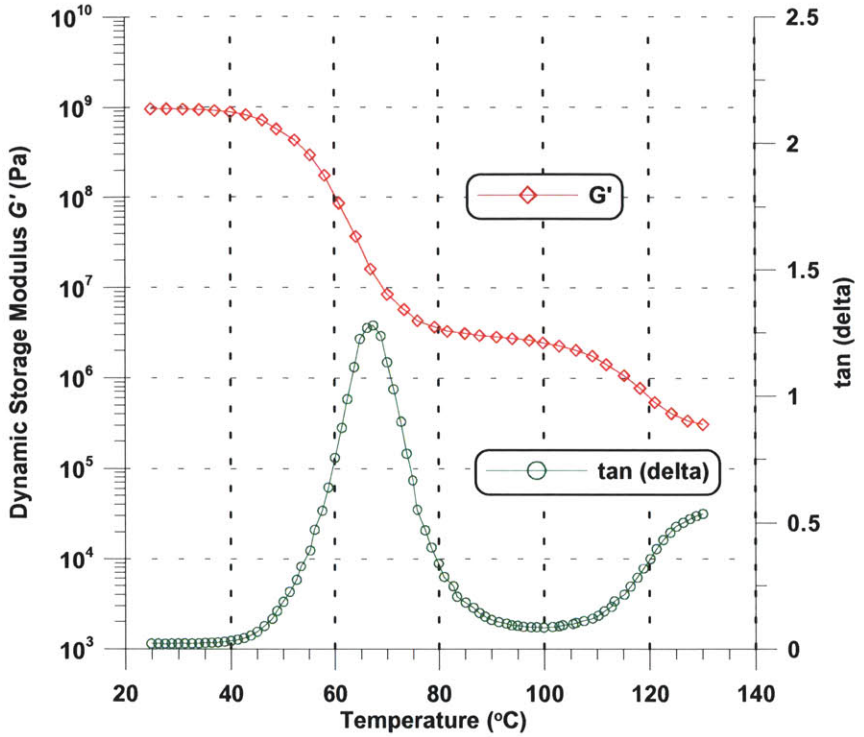

Figure B. 8: G' and tan (delta) of 5% volume content C2050 SMP, 43.6μ particle diameter.

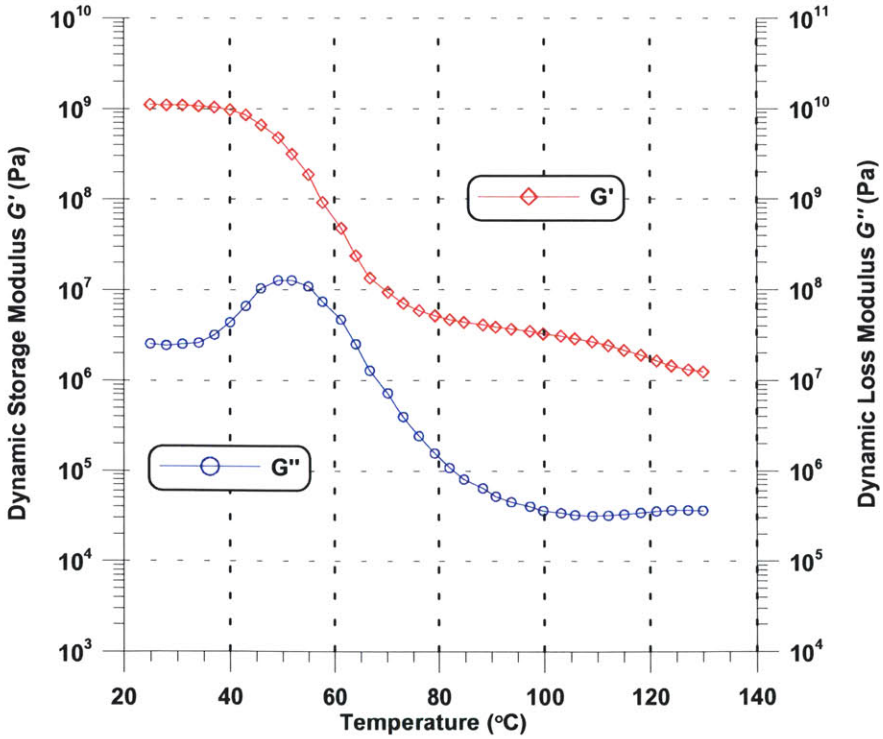

Figure B. 9: G' and G'' of 10% volume content C2050 SMP, 6.71μ particle diameter.

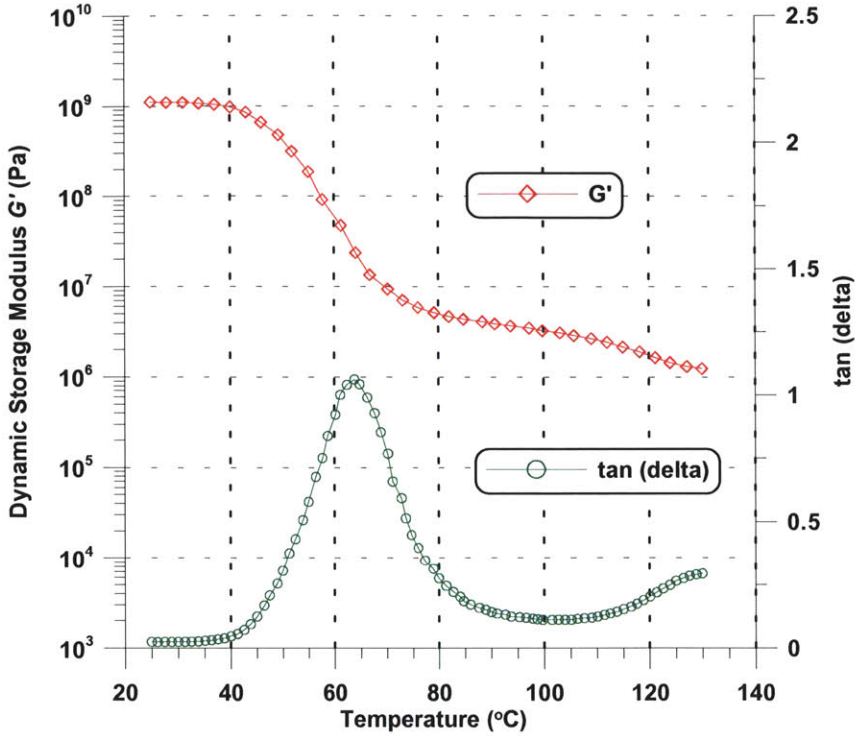

Figure B. 10: G' and tan (delta) of 10% volume content C2050 SMP, 6.71μ particle diameter.

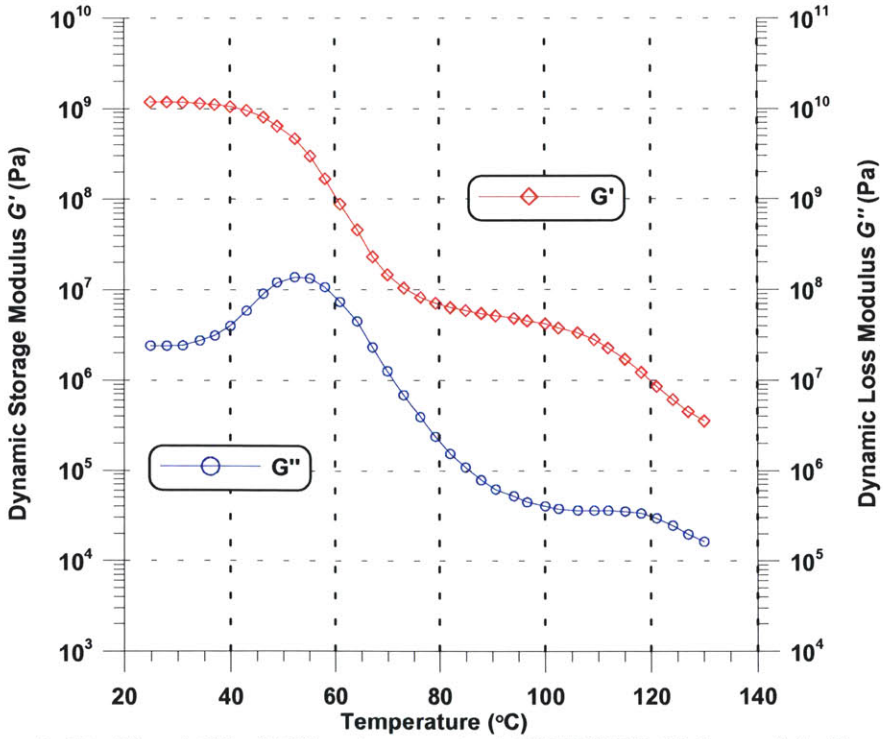

Figure B. 11: G' and G'' of 10% volume content C2050 SMP, 15.4μ particle diameter.

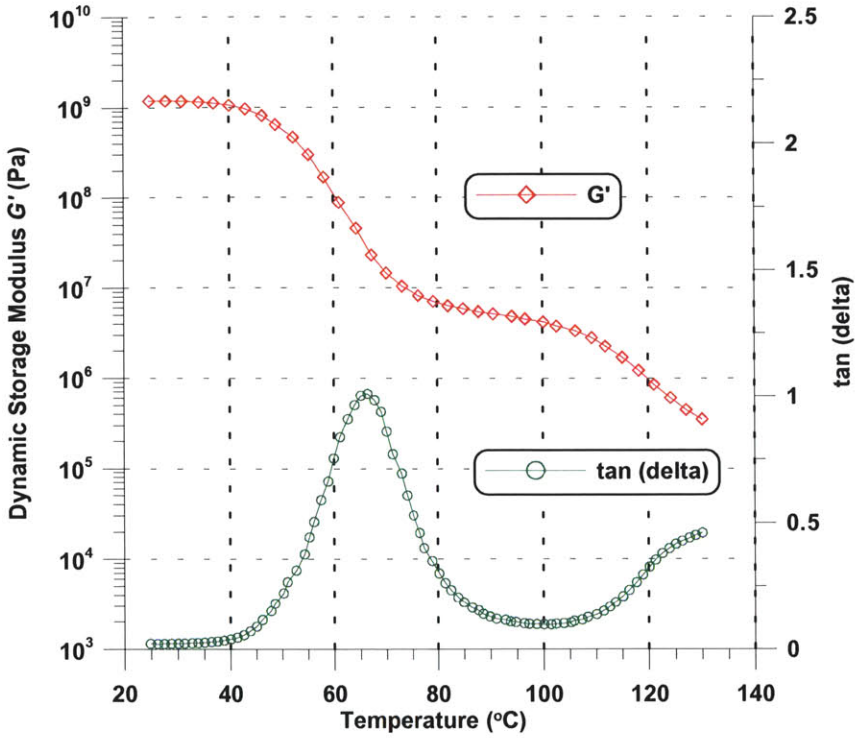

Figure B. 12: G' and tan (delta) of 10% volume content C2050 SMP, 15.4μ particle diameter.

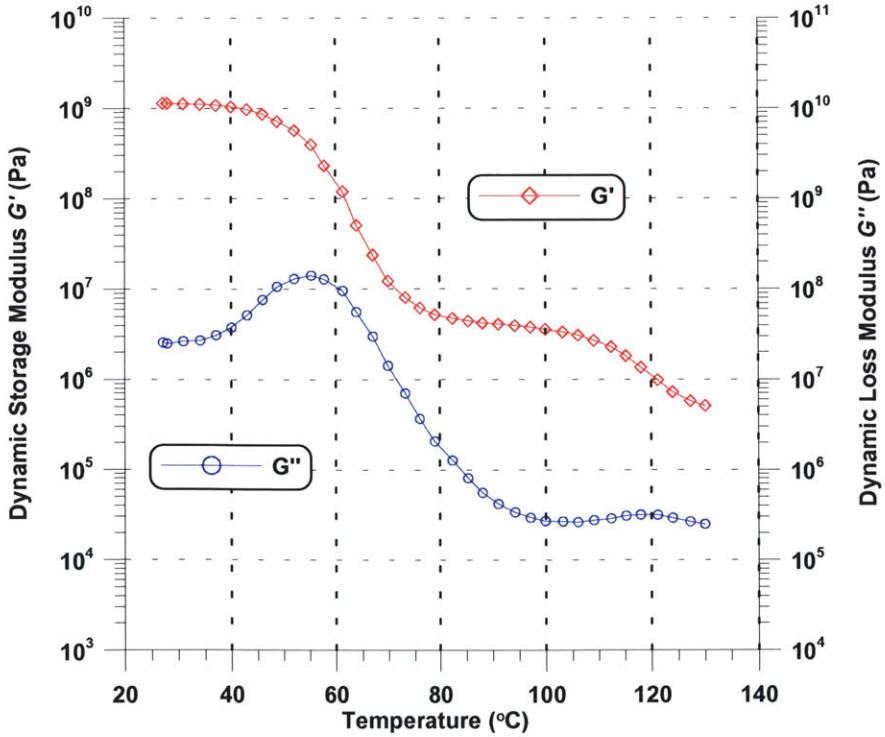

Figure B. 13: G' and G'' of 10% volume content C2050 SMP, 43.6μ particle diameter.

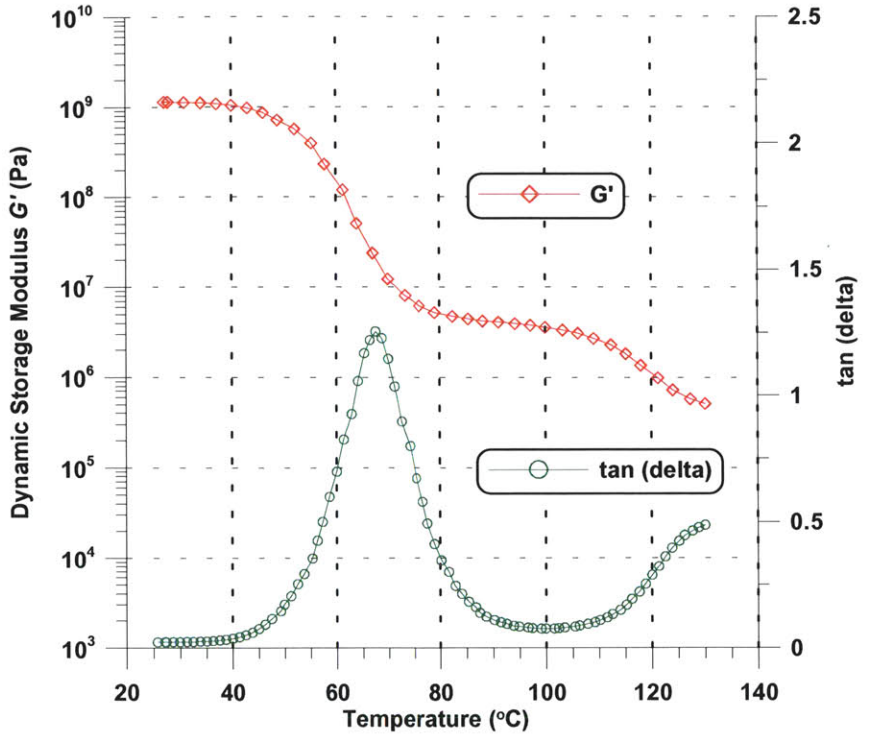

Figure B. 14: G' and tan (delta) of 10% volume content C2050 SMP, 43.6μ particle diameter.

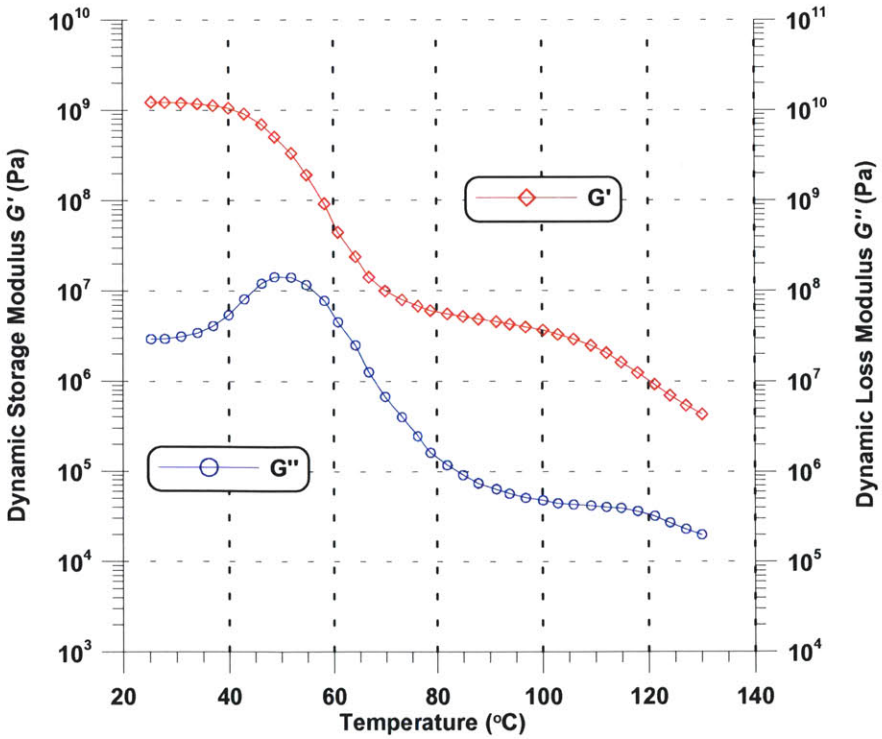

Figure B. 15: G' and G'' of 10% volume content cmd5005 SMP, 43.6μ particle diameter.

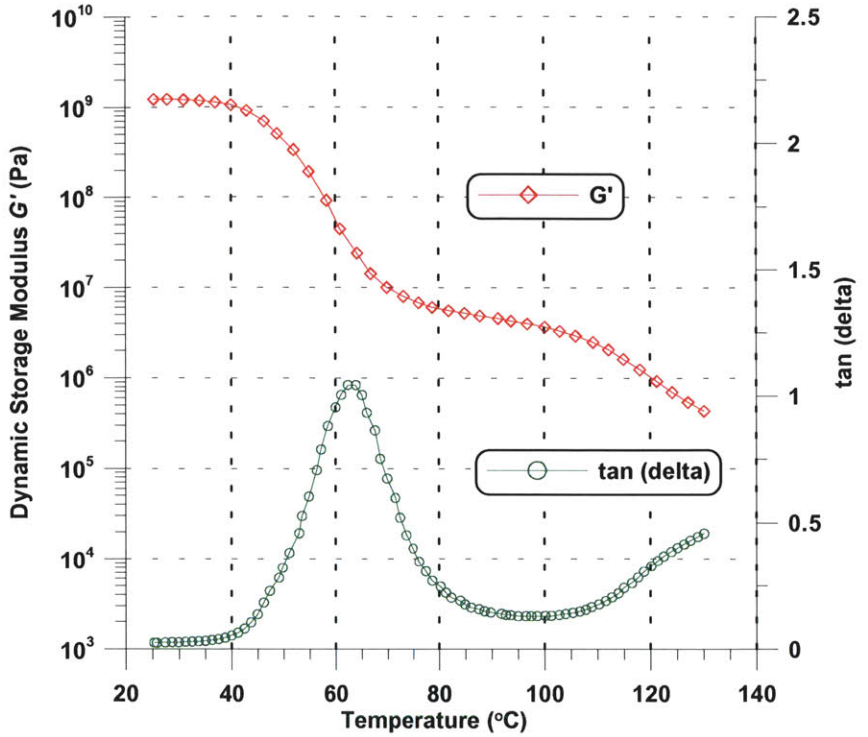

Figure B. 16: G' and tan (delta) of 10% volume content cmd5005 SMP, 43.6μ particle diameter.

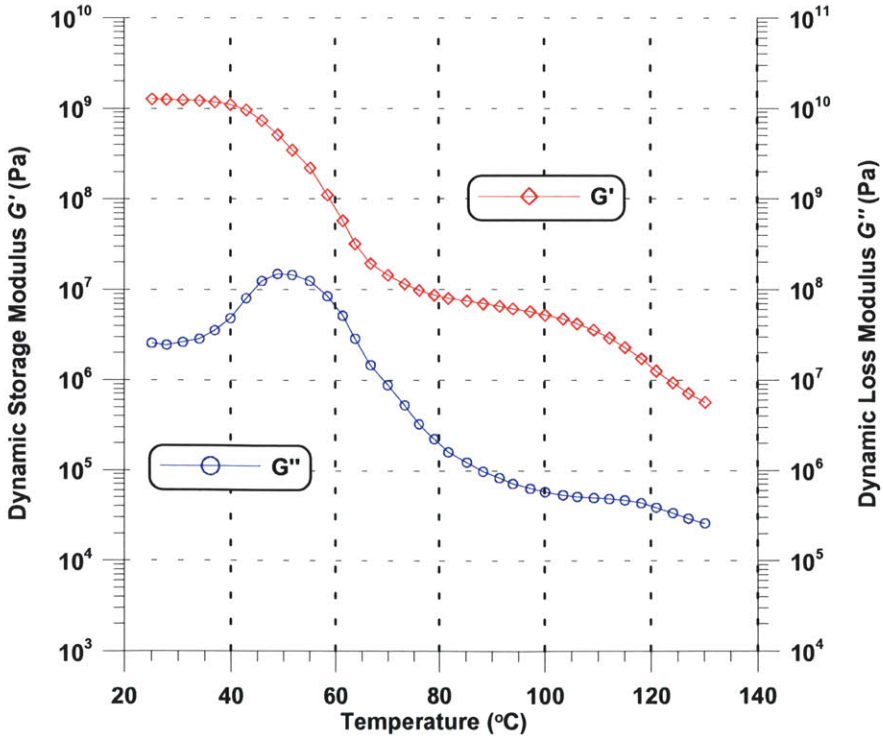

Figure B. 17: G' and G'' of 10% volume content N40 SMP, 43.6μ particle diameter.

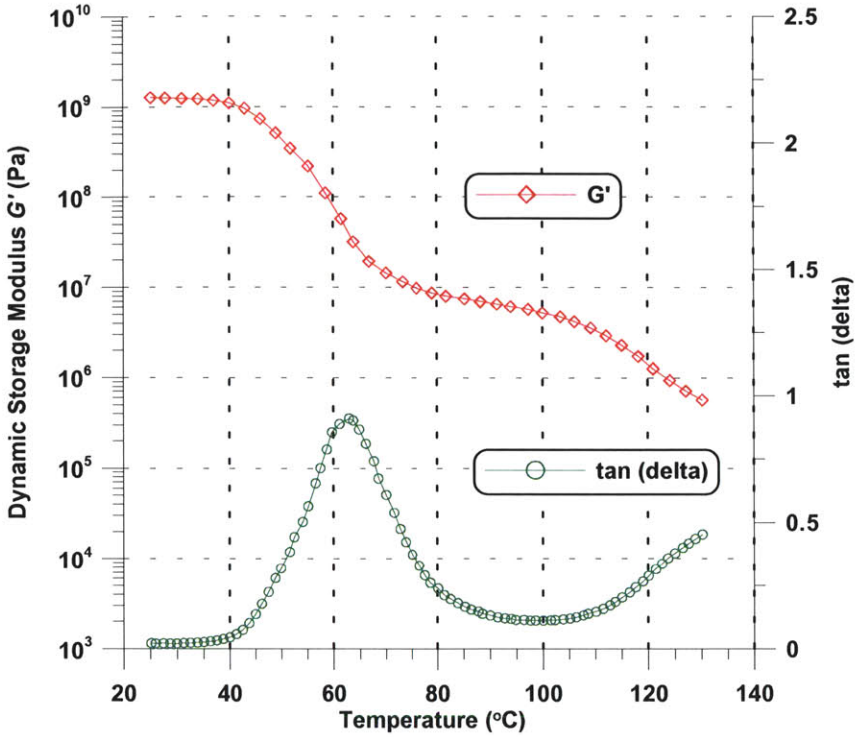

Figure B. 18: G' and tan (delta) of 10% volume content N40 SMP, 43.6μ particle diameter.

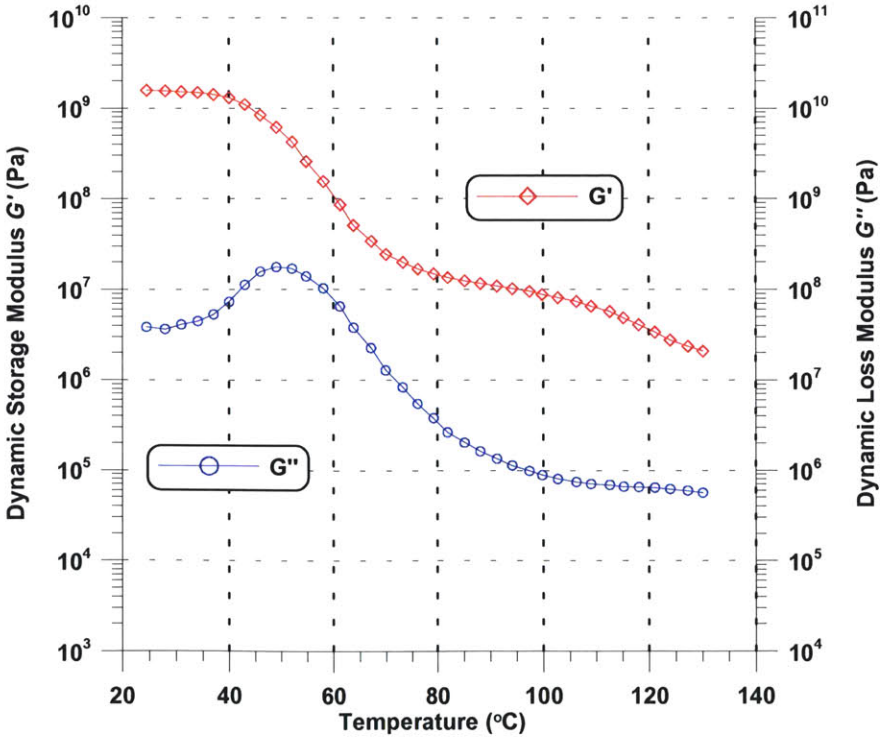

Figure B. 19: G' and G'' of 20% volume content C2050 SMP, 6.71μ particle diameter.

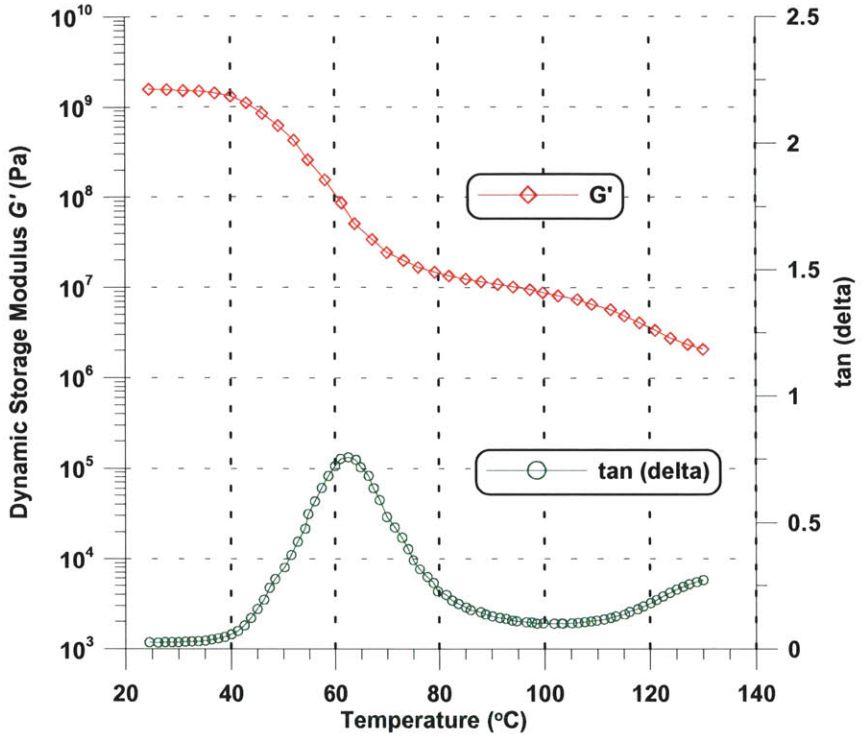

Figure B. 20: G' and tan (delta) of 20% volume content C2050 SMP, 6.71μ particle diameter.

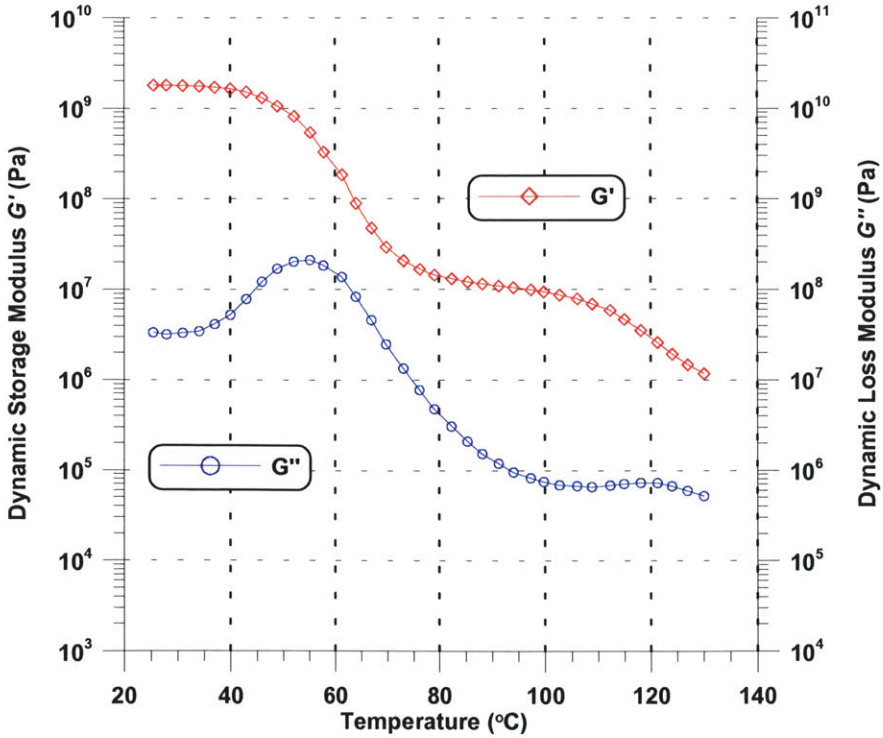

Figure B.21: G' and G'' of 20% volume content C2050 SMP, 43.6μ particle diameter.

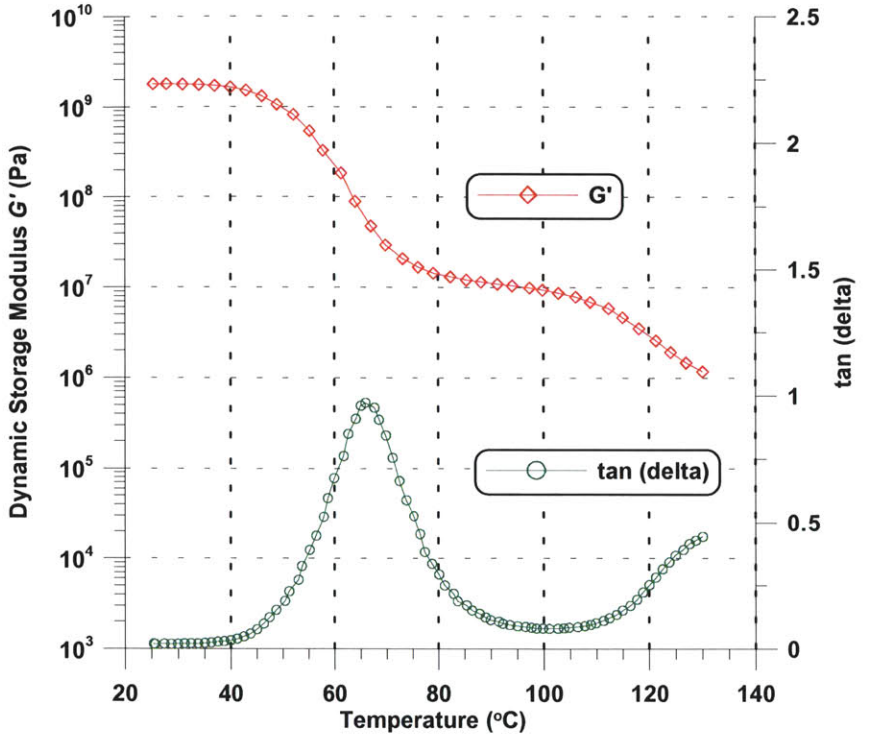

Figure B.22: G' and tan (delta) of 20% volume content C2050 SMP, 43.6μ particle diameter.

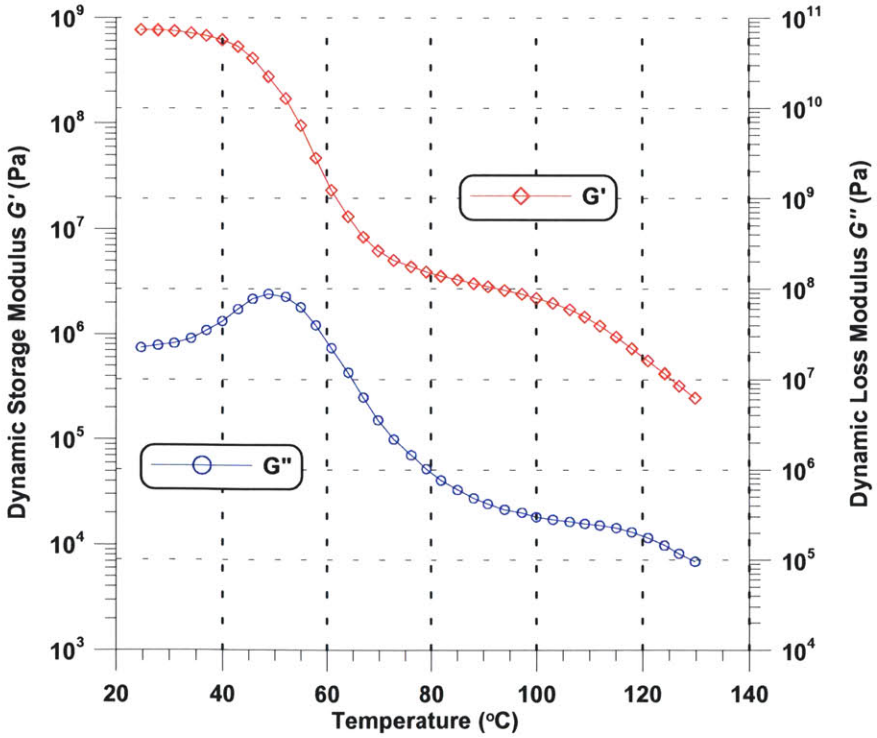

Figure B.23: G' and G'' of MP5510 SMP cured at 25c 2 hours and 80c 4 hours.

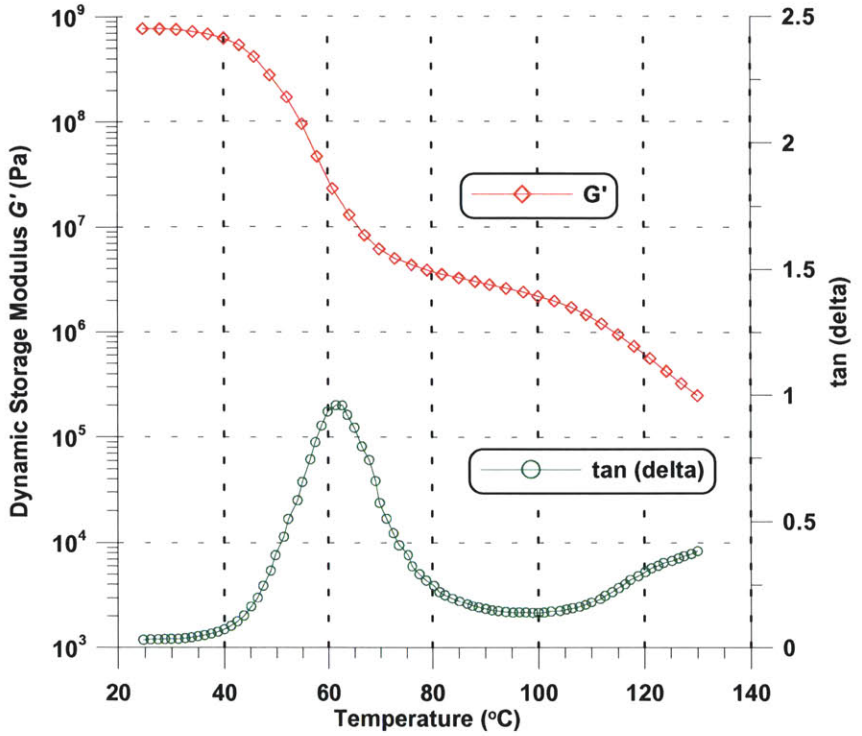

Figure B.24: G' and tan (delta) of MP5510 SMP cured at 25c 2 hours and 80c 4 hours.

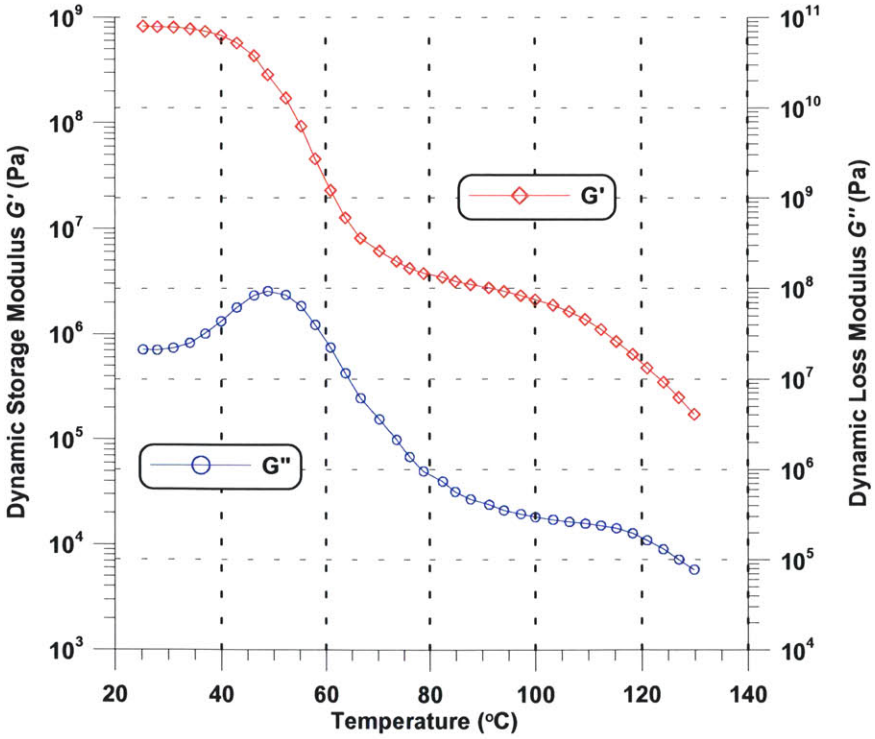

Figure B. 25: G' and G'' of MP5510 SMP cured at 25c 1 hour and 80c 5 hours.

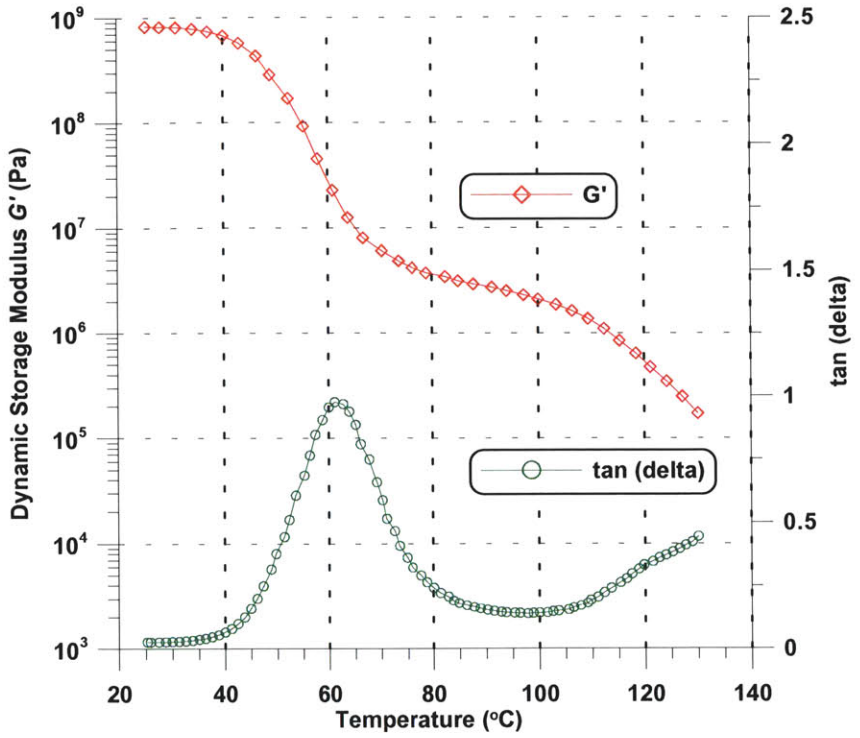

Figure B. 26: G' and tan (delta) of MP5510 SMP cured at 25c 1 hour and 80c 5 hours.

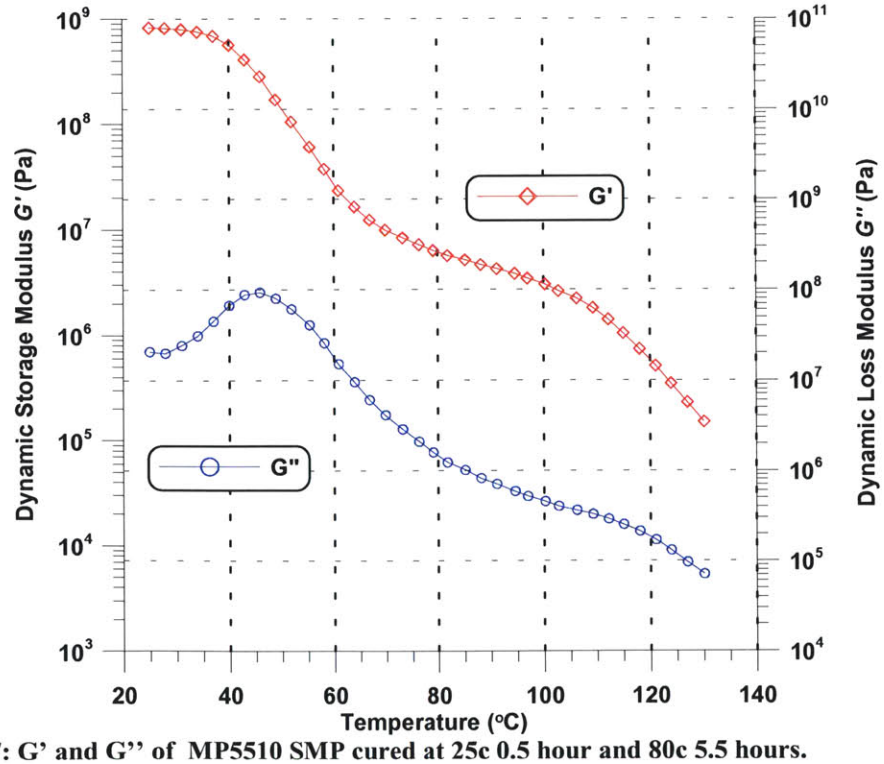

Figure B.27: G' and G'' of MP5510 SMP cured at 25c 0.5 hour and 80c 5.5 hours.

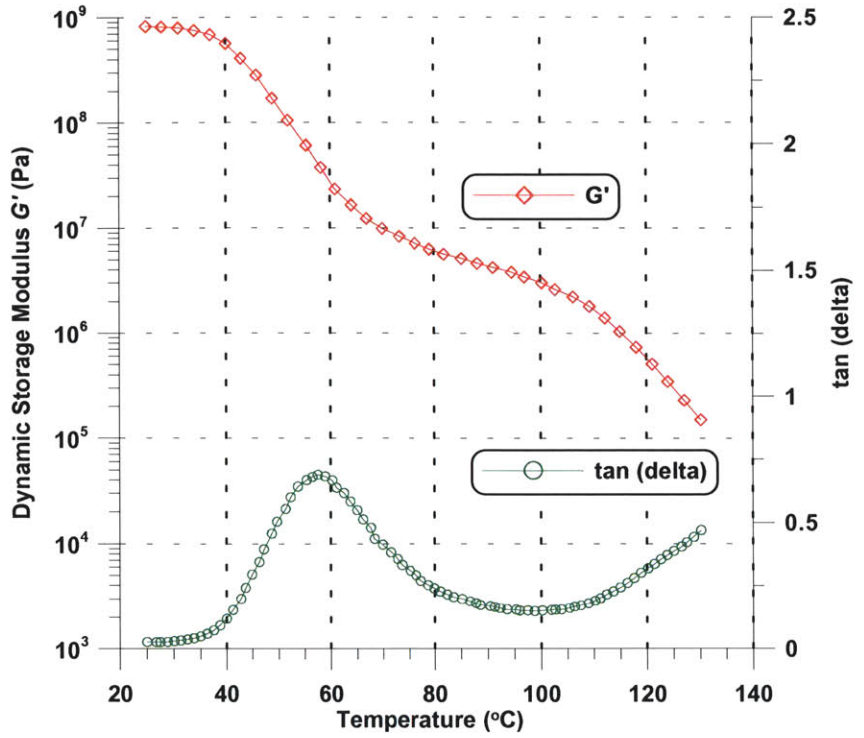

Figure B.28: G' and tan (delta) of MP5510 SMP cured at 25c 0.5 hour and 80c 5.5 hours.

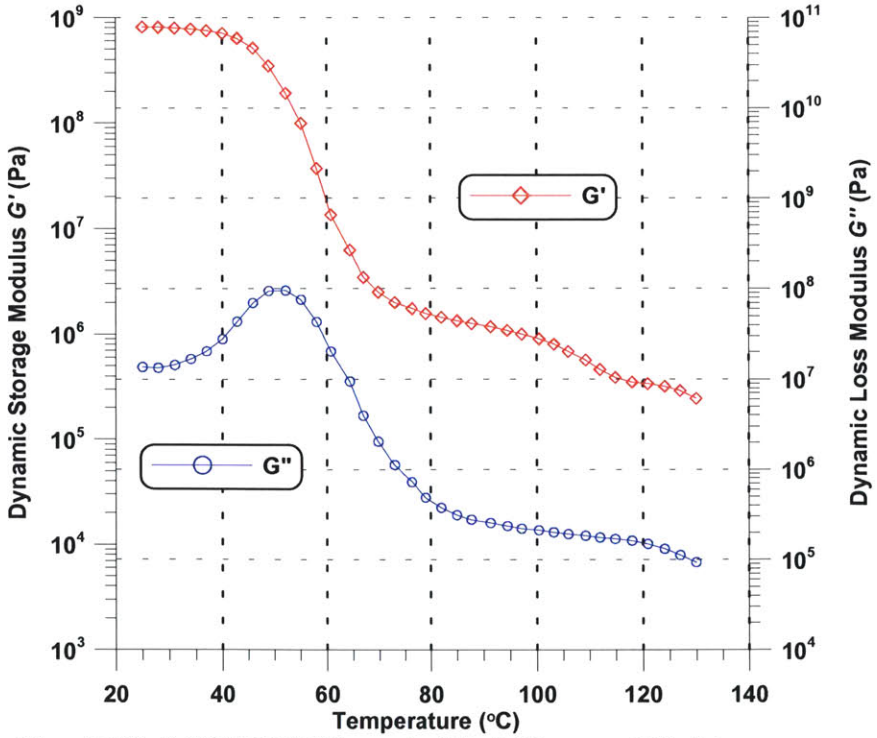

Figure B. 29: G' and G'' of MP5510 SMP cured at 25c 0.0 hour and 80c 6 hours.

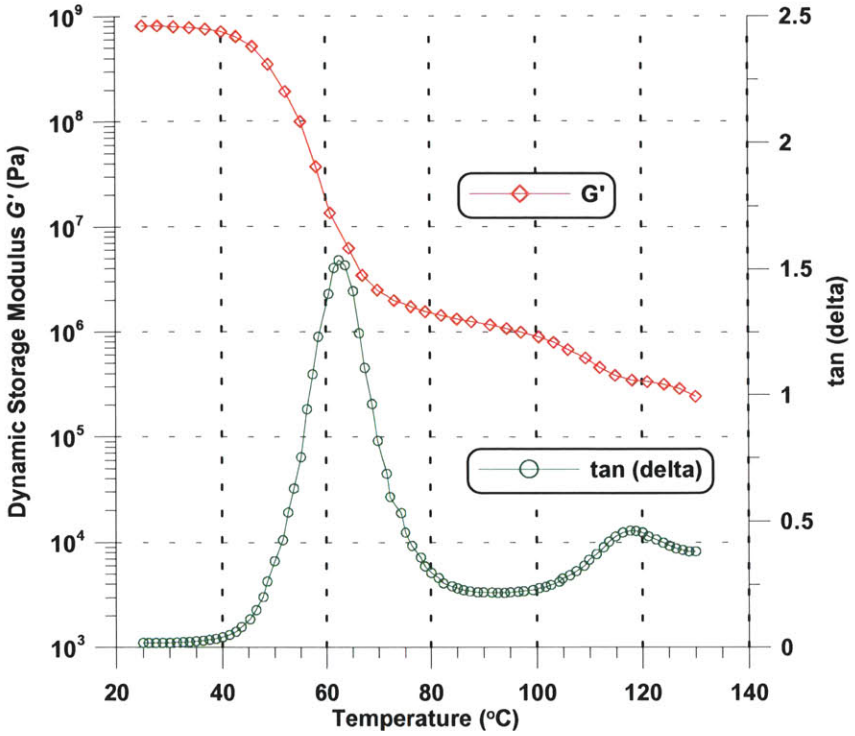

Figure B.30: G' and tan (delta) of MP5510 SMP cured at 25c 0.0 hour and 80c 6 hours.

Appendix C: DSC Curves

DSC test curves for various magnetic particle volume content, particle size and material. Test procedure can be seen in chapter 5. DSC samples are from the same sample batch as the samples used in the DMTA tests.

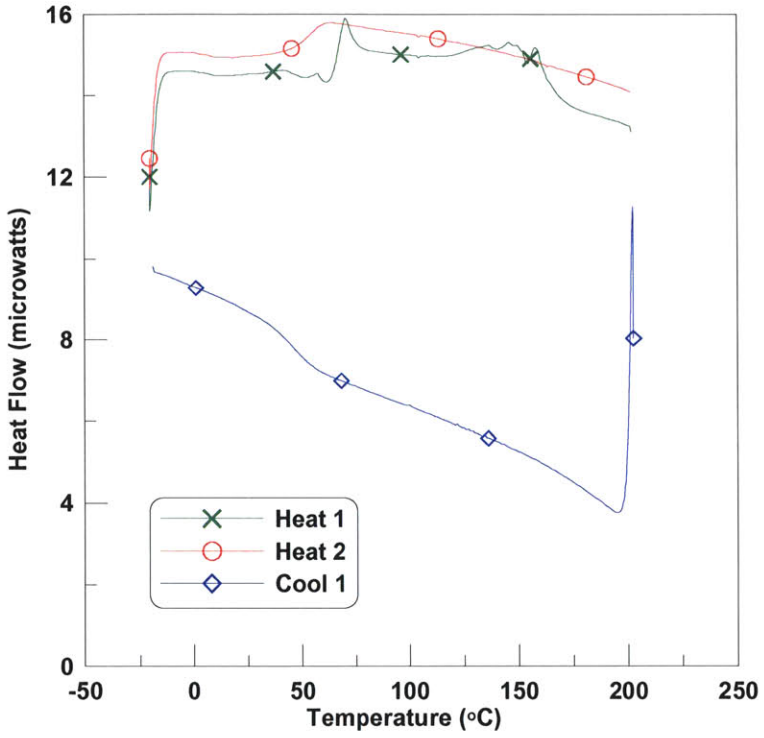

Figure C. 1: 1% volume content C2050 SMP, 6.71μ particle diameter.

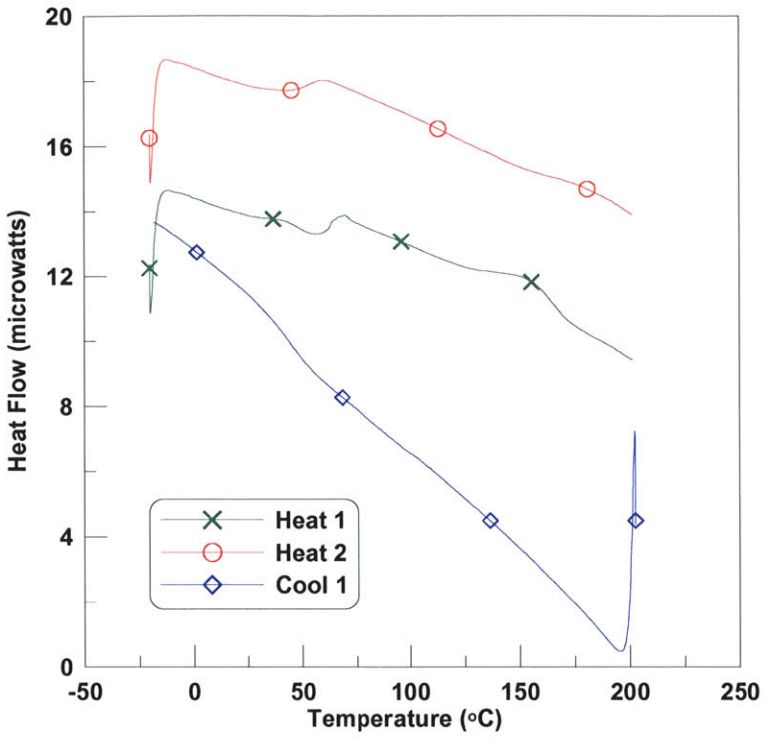

Figure C. 2: 1% volume content C2050 SMP, 43.6μ particle.

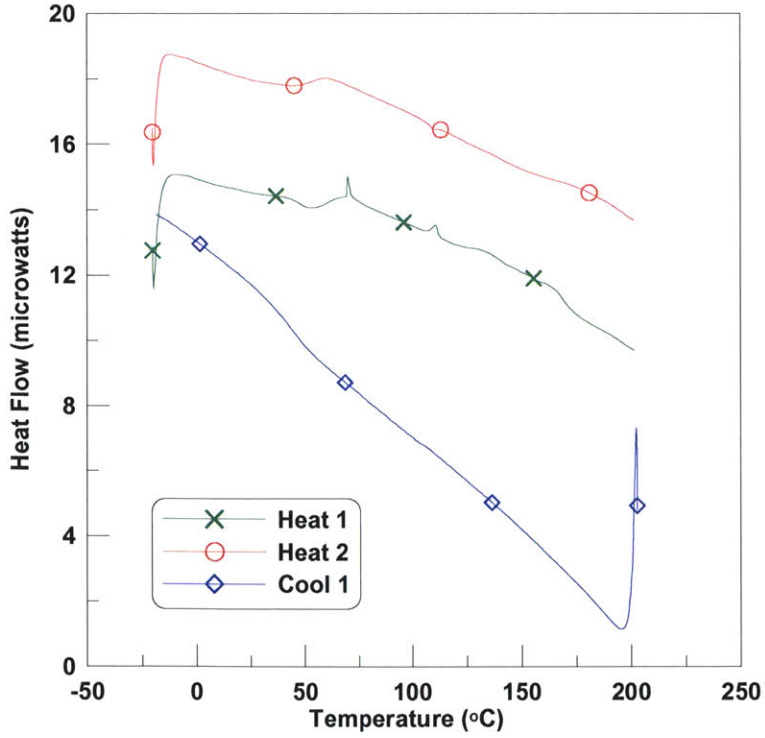

Figure C. 3: 5% volume content C2050 SMP, 6.71μ particle diameter.

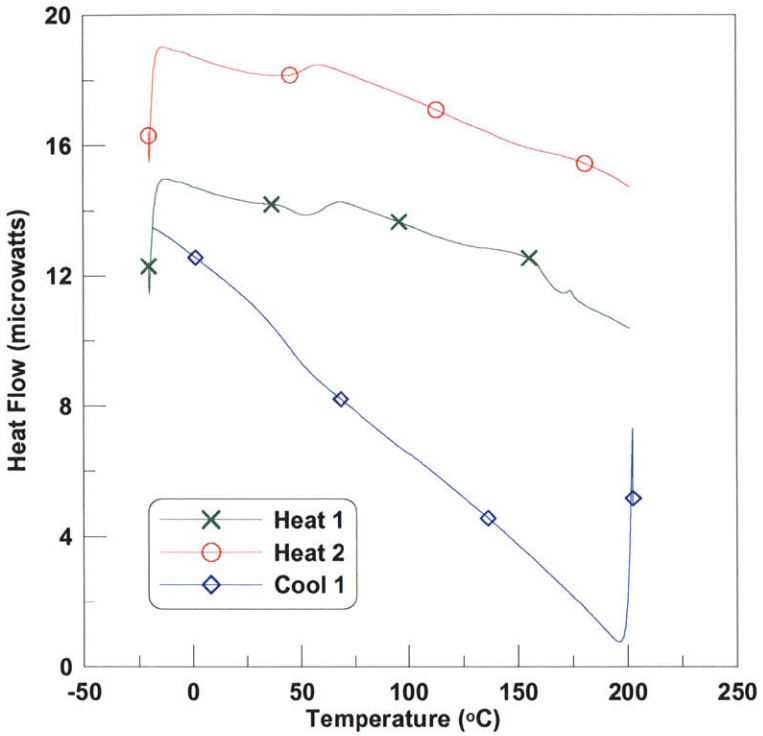

Figure C. 4: 5% volume content C2050 SMP, 43.6μ particle diameter.

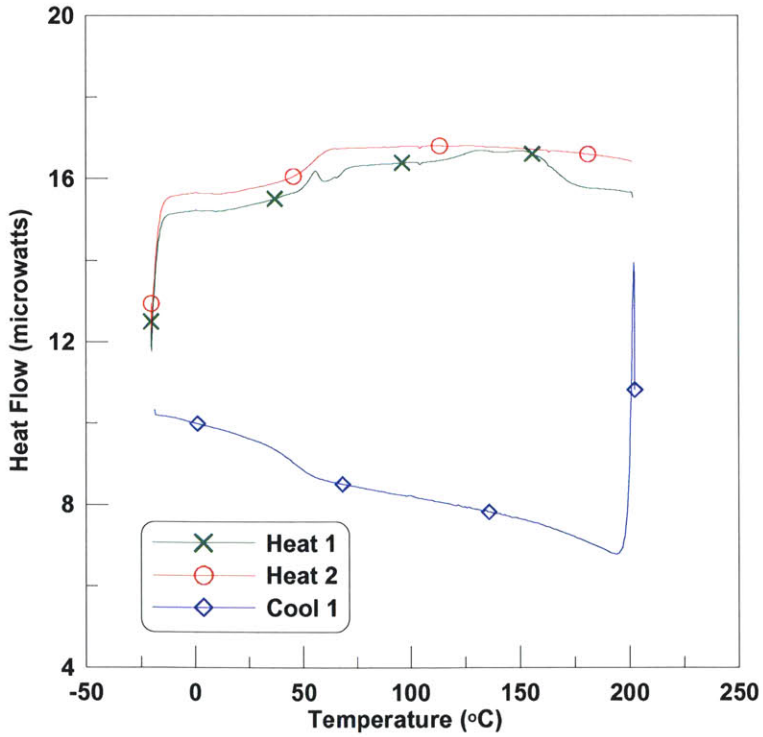

Figure C. 5: 10% volume content C2050 SMP, 6.71μ particle.

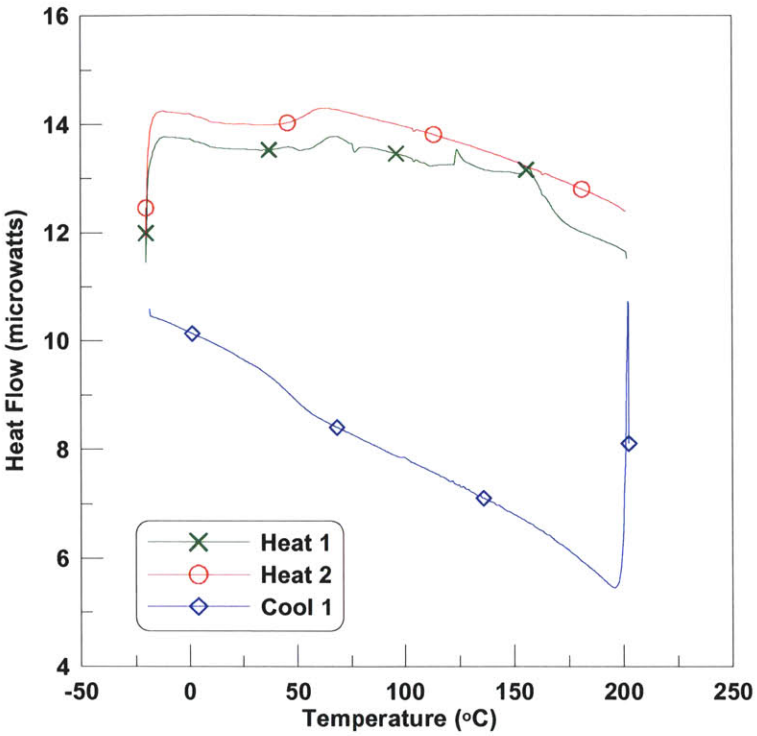

Figure C. 6: 10% volume content C2050 SMP, 15.4μ particle.

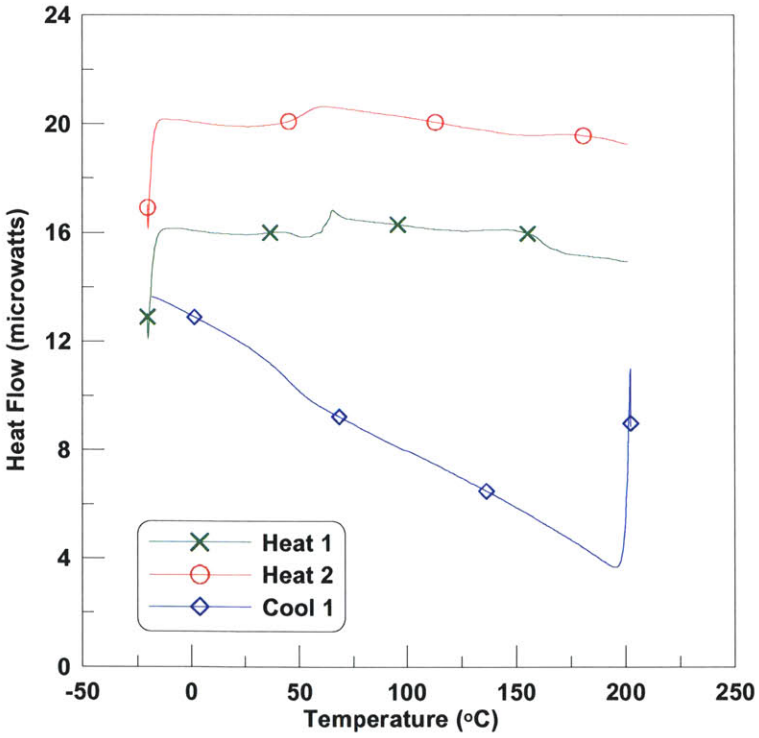

Figure C. 7: 10% volume content C2050 SMP, 43.6μ particle.

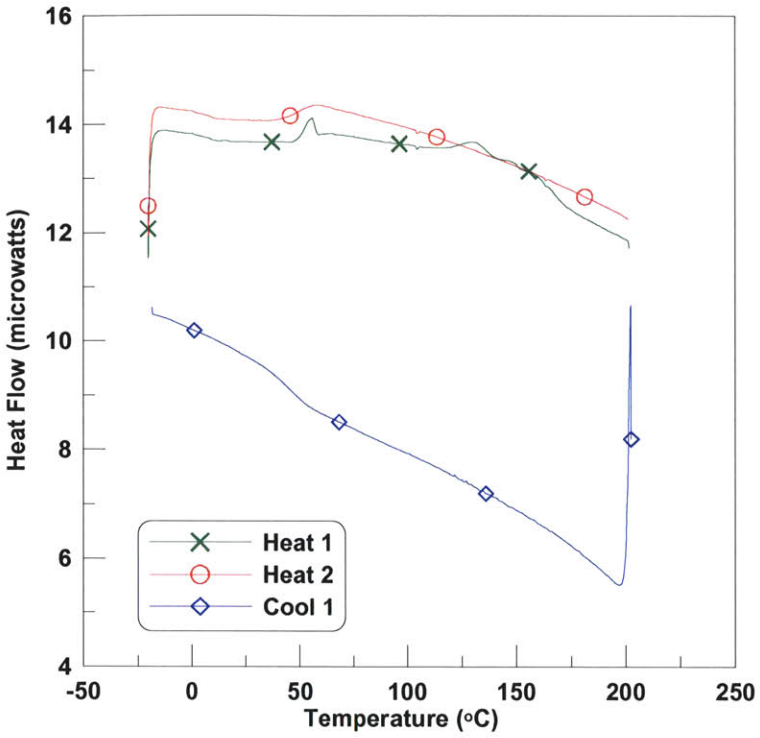

Figure C. 8: 10% volume content cmd5005 SMP, 43.6μ particle.

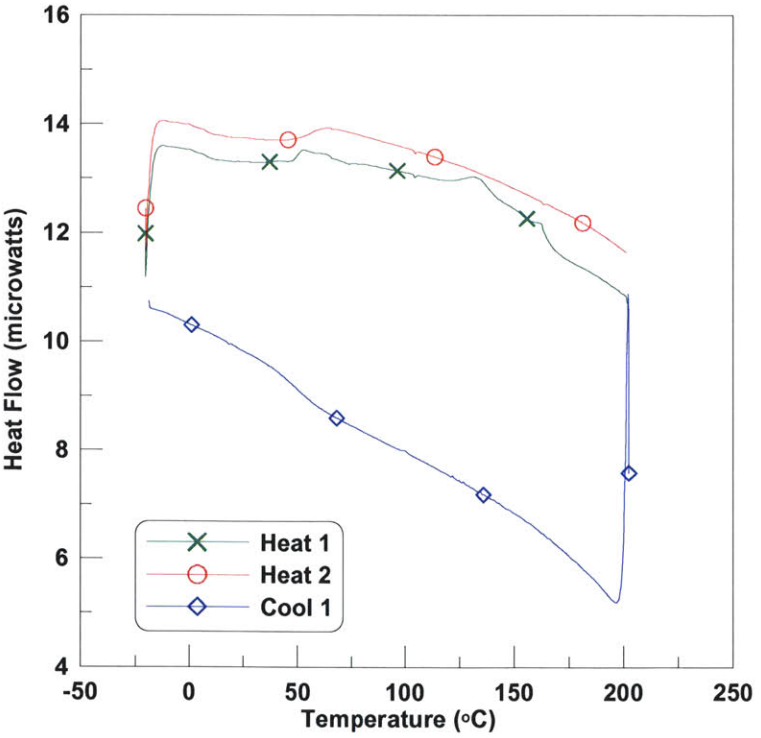

Figure C. 9: 10% volume content N40 SMP, 43.6μ particle.

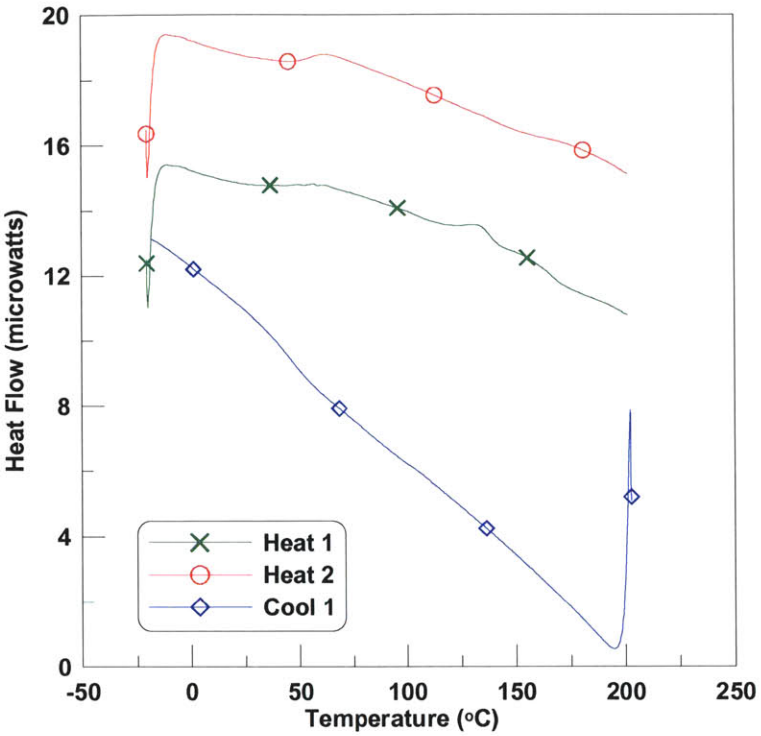

Figure C. 10: 20% volume content C2050 SMP, 6.71μ particle.

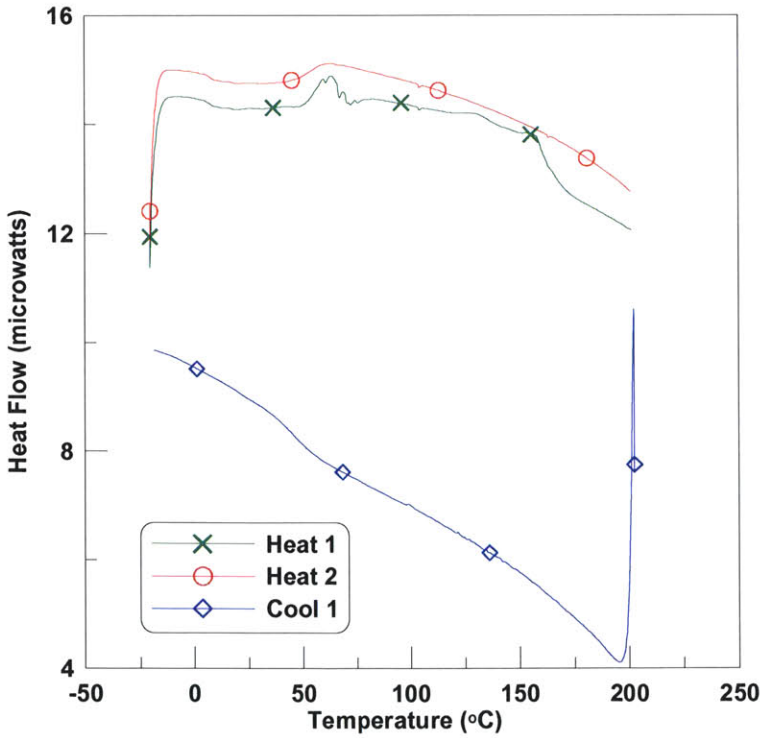

Figure C. 11: 20% volume content C2050 SMP, 43.6μ particle.

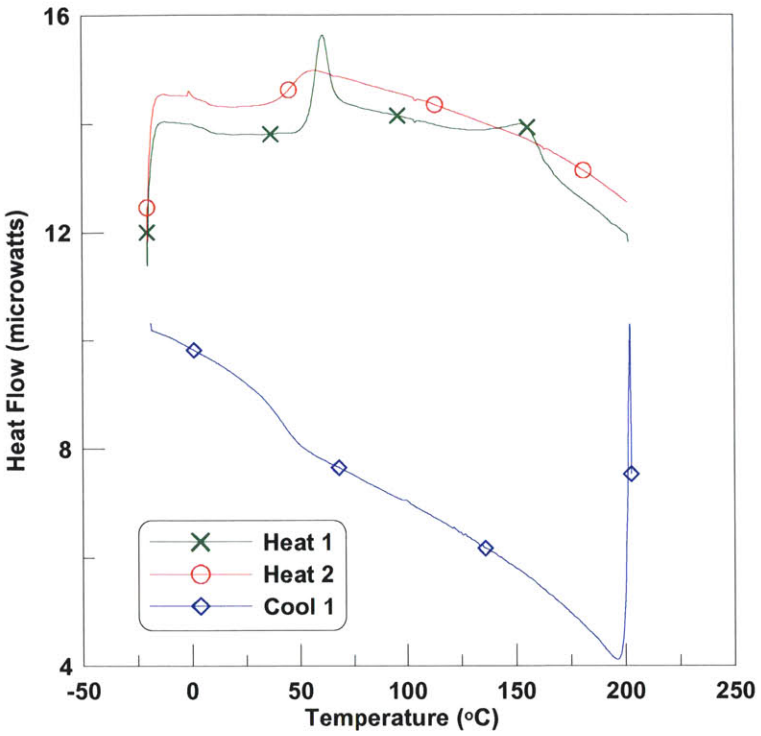

Figure C. 12: MP5510 SMP cured at 25c 0.0 hour and 80c 6 hours.

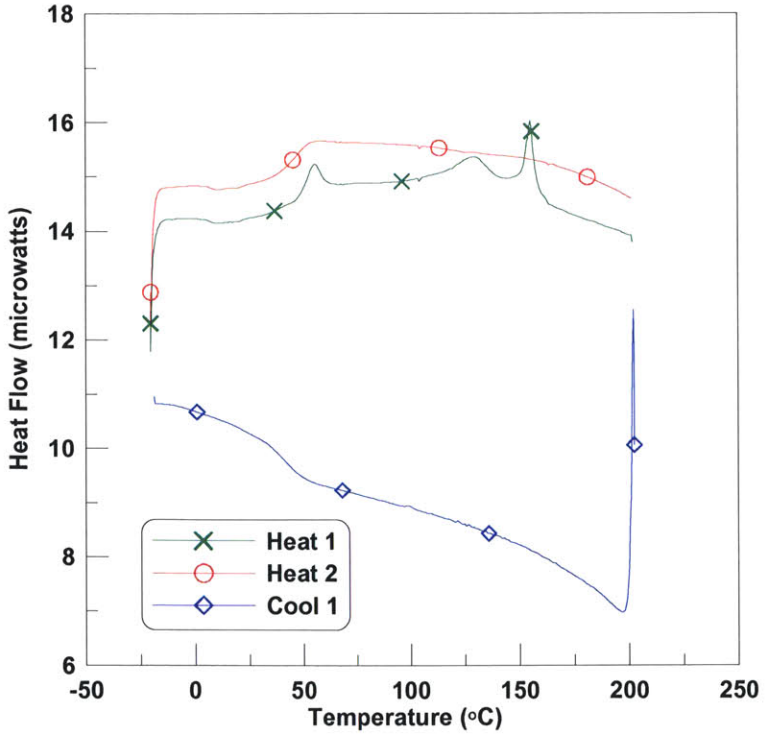

Figure C. 13: MP5510 SMP cured at 25c 0.5 hour and 80c 5.5 hours.

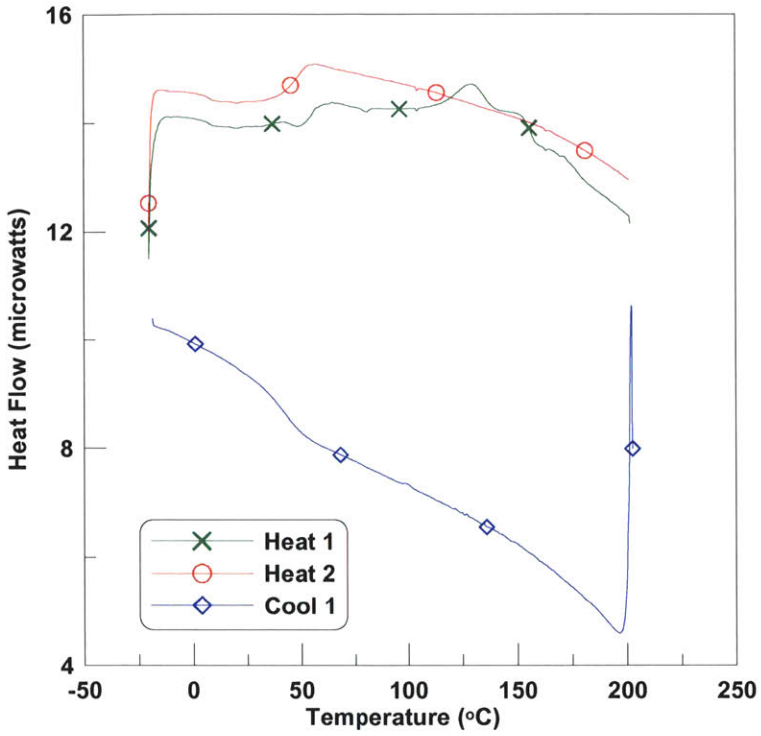

Figure C. 14: MP5510 SMP cured at 25c 1.0 hour and 80c 5.0 hours.

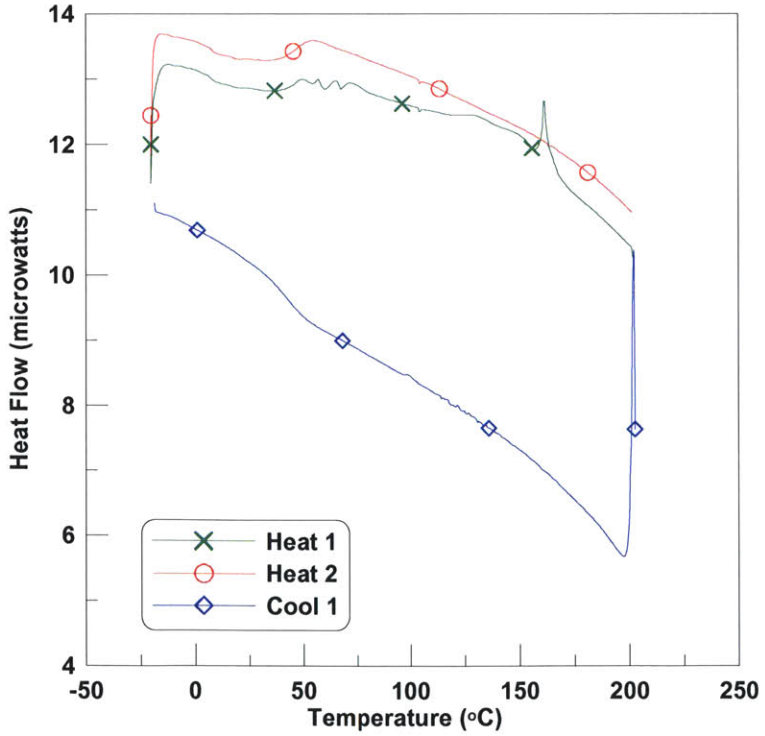

Figure C. 15: MP5510 SMP cured at 25c 2.0 hour and 80c 4.0 hours.

Appendix D: Strain Recovery Curves

Below are the strain recovery test curves. Young's modulus, E, is calculated from data points between 0.001 and 0.004 strain The red line represents the line which is fitted to these points and so subsequently the slope of this line is equal to E.

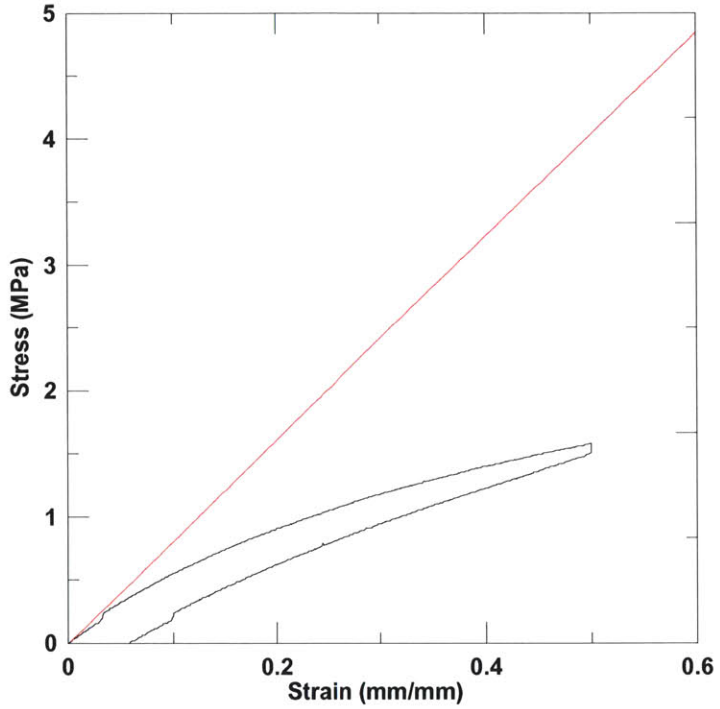

Figure D. 1: Strain recovery 1% volume content, 43.6μ particle diameter, C2050 magnetic material

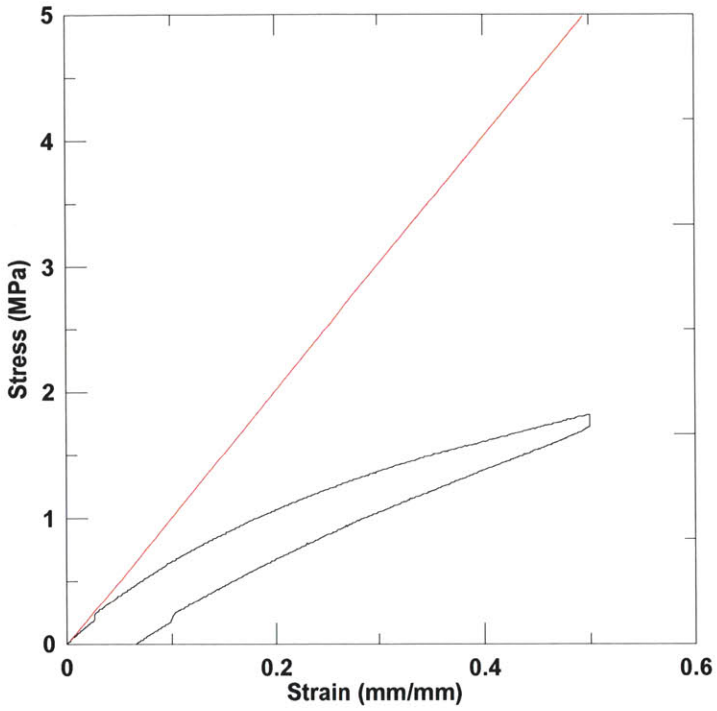

Figure D. 2: Strain recovery 5% volume content, 43.6μ particle diameter, C2050 magnetic material.

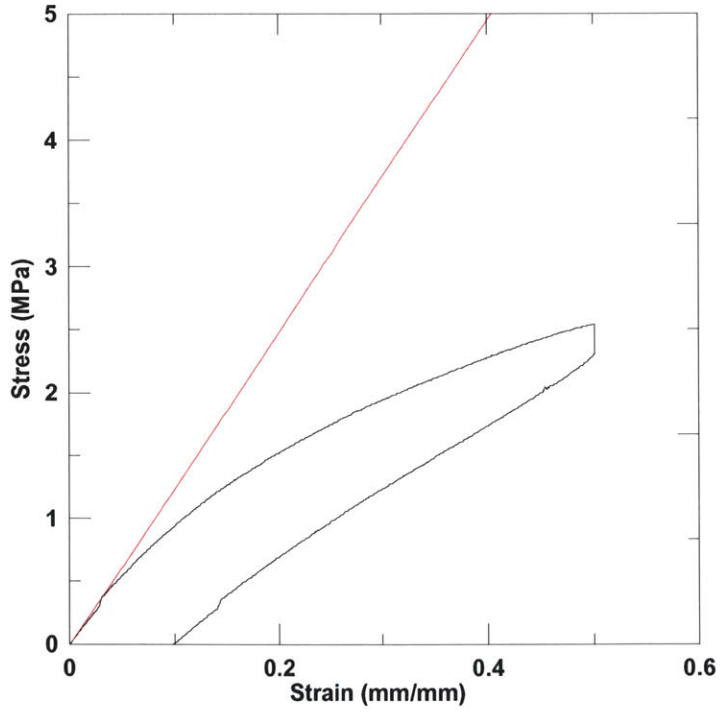

Figure D. 3: Strain recovery 10% volume content, 43.6μ particle diameter, C2050 magnetic material.

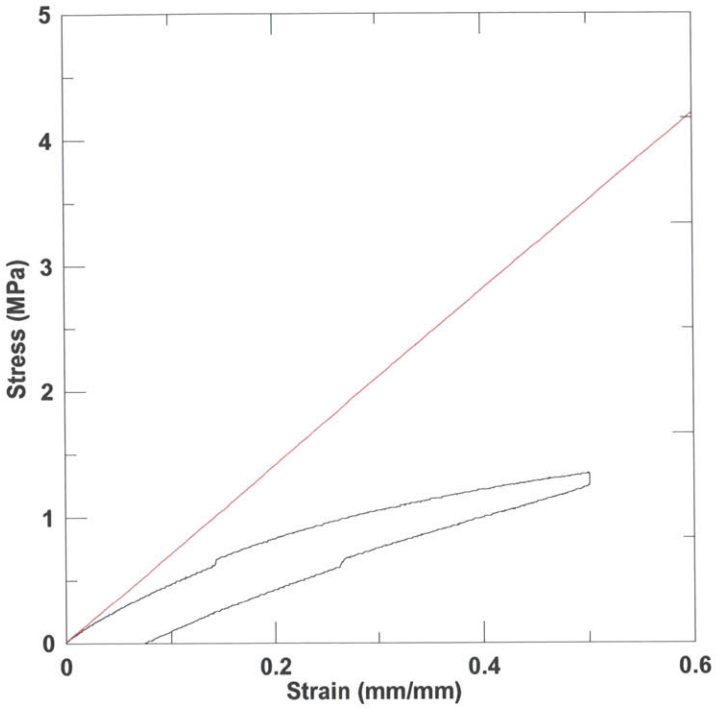

Figure D. 4: Strain recovery 0% particle volume content, SMP 2 hour 25 °C cure.

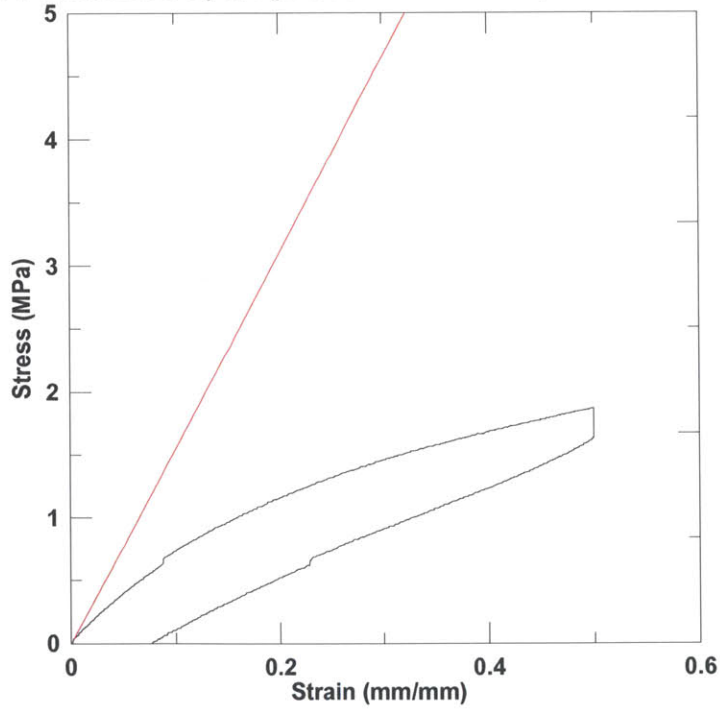

Figure D. 5: Strain recovery 0% particle volume content, SMP 0 hour 25 °C cure.